AN INVESTIGATION OF REMOTELY SENSED URBAN HEAT ISLAND CLIMATOLOGY

By

Leiqiu Hu

Submitted to the Department of Geography and the
Graduate Faculty of the University of Kansas
in partial fulfillment of the requirements for the degree of
Doctor of Philosophy

Committee members

Dr. Nathaniel A. Brunsell, Chairperson

Dr. Johannes J. Feddema

Dr. David B. Mechem

Dr. David A. Rahn

Dr. C. Bryan Young

Date defended: June 27, 2014

The Dissertation Committee for Leiqiu Hu certifies
that this is the approved version of the following dissertation :

AN INVESTIGATION OF REMOTELY SENSED URBAN HEAT ISLAND CLIMATOLOGY

Dr. Nathaniel A. Brunsell, Chairperson

Date approved: June 27, 2014

Abstract

Satellite remotely sensed temperatures are widely used for urban heat island (UHI) studies. However, the abilities of satellite surface and atmospheric data to assess the climatology of UHI face many unknowns and challenges. This research addresses the problems and potentials for satellite remotely sensed UHI climatology by examining three different issues. The first issue is related to the temporal aggregation of land surface temperature (LST) and the potential biases that are induced on the surface UHI (SUHI) intensity. Composite LST data usually are preferred to avoid the missing values due to clouds for long-term UHI monitoring. The impact of temporal aggregation shows that SUHI intensities are more notably enhanced in the daytime than nighttime with an increasing trend for larger composite periods. The cause of the biases is highly related to the amount and distribution of clouds. The second issue is related to model validation and the appropriate use of LST for comparison to modeled radiometric temperatures in the urban environment. Sensor view angle, cloud distribution, and cloud contaminated pixels can confound comparisons between satellite LST and modeled surface radiometric temperature. Three practical sampling methods to minimize the confounding factors are proposed and evaluated for validating different aspects of model performance. The third issue investigated is to assess to what extent remotely sensed atmospheric profiles collected over the urban environment can be used to examine the UHI. The remotely sensed air and dew-point temperatures are compared with the ground observations, showing an ability to capture the temporal and spatial dynamics of atmospheric UHI at a fine scale. Finally, a new metric for quantifying the urban heat island is proposed. The urban heat island curve (UHIC),

is developed to represent UHI intensity by integrating the urban surface heterogeneity in a curve. UHIC illustrates the relationship between the air temperature and the urban fractions, and emphasizes the temperature gradients, consequently decreasing the impact of the data biases. This research illustrates the potential for satellite data to monitor and increase our understanding of UHI climatology.

Acknowledgements

I would like to thank a great many people who made this dissertation possible.

My deepest gratitude is to my advisor, Dr. Nathaniel A. Brunsell, for the guidance, support, and encouragement to make the ideas become a completed study. I would like to thank my committee members: Dr. Johannes J. Feddema, Dr. David B. Mechem, Dr. David A. Rahn (Department of Geography, KU), and Dr. Bryan Young (Department of Civil, Environmental and Architectural Engineering, KU) for their friendly guidances and insightful suggestions.

I am thankful for the collaboration of Dr. Andrew J. Monaghan, Dr. Michael Barlage, Dr. Olga V. Wilhelmi and Dr. Keith W. Oleson from National Center for Atmospheric Research, who provide abundant inspirations and insightful suggestions.

I extend my gratitude to the KU biometeorology lab members for giving me great supports and help.

Last but not least, I give heartfelt thanks to my family and friends that surround me in China and U.S. Especially to my mother, Huaxiu Lei, for her selfless love and dedication to support me pursuing this final degree.

This research was possible thanks to funding from National Aeronautics and Space Administration program (NNX10AK79G): System for Integrated Modeling of Metropolitan Extreme Heat Risk (SIMMER).

Contents

List of Figures

List of Tables

Chapter 1

Introduction

1.1 The Problems

Urban areas account for 79% of the U.S. population (Population Reference Bureau, 2011), and this percentage will likely increase in the future. The high density population in the urban environment exerts complex impacts on urban surroundings. One impact is the urban heat island (UHI) (Gallo et al., 1993; Sen Roy and Yuan, 2009), showing a higher temperature in the urban environment compared to its rural surroundings. This phenomenon not only affects human health related to high temperature (Patz et al., 2005) and air pollution (Mage et al., 1996; Taha, 1997), but it also starts a vicious cycle consuming energy to cool buildings and resulting in generating more anthropogenic heat. Long-term monitoring of the UHI helps us to understand UHI features and the urban climatology behind it.

UHI studies are well documented across time and space by using various measuring techniques and temperatures as summarized by Voogt and Oke (2003). Two distinct classes of the UHI are often defined: the atmospheric UHI is assessed through in-situ and vehicle mounted sensors measuring air temperatures in the urban canopy layer (UCL) (Oke, 1976) and through the ground-based, airborne and tower amounted senors for the urban boundary layer (UBL) (Barlow et al., 2011; Grimmond, 2006; Voogt and Oke, 2003; Roth, 2000); the second class is the surface UHI

(SUHI) and is based on the use of thermal remotely sensed data (Voogt and Oke, 2003). However, for atmospheric UHI at the UCL and UBL, the representativeness is questionable due to heterogeneous urban surface properties (Stewart, 2011) and comparatively insufficient data sources for a large scale study (Grimmond, 2006).

The SUHI research community is thriving after the land surface temperature (LST) available from thermal remote sensing (Voogt and Oke, 2003; Gallo et al., 1995). Satellite remotely sensed data overcome some problems of in-situ measurements, generally with various sources, global coverage, long-term archive, and steady repeat frequency. Taking these features into consideration, satellite-based UHI studies have great potential to improve our understanding of the spatial–temporal variability of the physical processes over the urban areas, which influence the long-term urban climate.

However, simply applying LST introduces errors to quantify UHI intensity due to the nature of remote sensing techniques, especially for long-term or large-scale investigations. One of the primary issues is clouds. Infrared remote sensing is not able to detect the surface under clouds, so all SUHIs are discussed under clear sky conditions. Temporally composited LSTs are usually the solution for the missing data due to clouds (Schwarz et al., 2011; Gallo and Owen, 1999). The impact of the inhomogeneous cloud distribution over the urban area on the biased sampling through the compositing process is usually neglected.

In addition to clouds, other factors also influence the representativeness of surface temperature, such as sensor view angle. The satellite LST is a directional radiative temperature, representing the information from a certain view angle (Voogt and Oke, 2003). This unique feature becomes important when we try to use remotely sensed temperature as truth for model validation. Directly validating the model performance using satellite observations causes a big uncertainty due to several essential incomparable aspects, such as cloud distributions and the thermal anisotropic urban surface.

The in-situ measurements of air temperature and remote sensing of LST have their incompatible advantages, which result in distinct methodologies to address two concepts of UHI: atmo-

spheric and surface UHI. The gridded observational air temperature may bridge the gaps between weaknesses of these types of observations, and may be able to improve the understanding of UHI impacts on human health more clearly with a comprehensive spatial distribution. Moreover, the common problem for current UHI studies is the unclear urban/rural divisions, resulting in a variety of UHI magnitudes that may be not comparable across space and time.

1.2 The Research Questions and Research Objects

The purpose of this dissertation research is to address the common problems related to the use of thermal remote sensing for long-term monitoring and to develop some practical solutions for these problems, and to further explore the potentials of remote sensing techniques to break the barriers of traditional measurements of air temperature and land surface temperature for atmospheric UHI studies.

Based on the problems address previously, this reserach is attempting to answer the following questions.

- *What is the impact of temporal aggregation of remote sensing data on UHI studies and what are the main causes of it?*
- *How can we use MODIS land surface temperature to validate long-term urban model simulations?*
- *Can the air and dew-point temperatures retrieved from MODIS capture the atmospheric UHI features, spatially and temporally?*
- *How can we quantify UHI magnitude using remote sense data?*

1.3 Organization of the Dissertation

Chapter 2,3, 4 are formatted as journal papers: an introduction addresses the problems, research questions, and objects; the methodology describes the data processing and analysis methods; results and discussions contain the details of each findings; and the summary of each chapter and some future research suggestions. At last, Chapter 5 is a brief summary about the conclusions drawn from this dissertation, the contributions to the UHI climatology literature, and some research directions that are important in the future.

Chapter 2

The impact of temporal aggregation of land surface temperature data for surface urban heat island (SUHI) monitoring

2.1 Introduction

More than 50% of the world population live in urban areas, and that proportion will likely grow in the future (World Health Organization Centre for Health Development, 2010). One impact of the urban population is the urban heat island (UHI) (Gallo et al., 1993; Sen Roy and Yuan, 2009). The urban environment with higher temperature not only affects the inhabitability caused by air pollution (Taha, 1997), and increases human health problems related to high temperature (Kalkstein and Greene, 1997; Patz et al., 2005), but also starts a vicious circle to encourage consuming energy to cool buildings, resulting in more anthropogenic heat. As a result, long term monitoring of UHI becomes necessary and it is essential to understand UHI features and the urban climatology behind it.

Remote sensing techniques introduce a new viewpoint to understand UHI, using land surface temperature (LST) to define the surface UHI (SUHI) (Voogt and Oke, 2003). Traditionally, air

temperature differences between urban and rural areas using pairs of in-situ climatology data define UHI, and were conducted by many studies (Henry et al., 1989; Gallo and Owen, 1999; Gaffin et al., 2008; Morris et al., 2001; Shao et al., 2011; Chow et al., 2011). However, the representativeness is questionable due to heterogeneous urban surface properties and comparatively insufficient data sources. After the advent of thermal remote sensing, LST data became available, and a variety of LST related SUHI studies used multiple sensors carried by satellites (Gallo et al., 1993; Streutker, 2003) and aircraft (Lo et al., 1997; BenDor and Saaroni, 1997; Quattrochi et al., 2000). Satellite remote sensing overcomes some problems of in-situ measurements generally with wider sources, broader coverage, and steadier periodicity. Taking these features into consideration, using remote sensing to study SUHI can improve conductive to understand the spatial–temporal variability of physical processes, which influence the long-term urban climate.

The satellite remote sensing approach, however, has its own limitations. One of the primary issues affecting data accuracy is that clouds can easily contaminate the data due to the indirect nature of remote sensing. Hence, the accuracy of LST products is highly contingent upon the cloud-screening algorithm (Wan, 2008). Even though LST can be accurately derived, it is hard to avoid missing data due to clouds. Researchers commonly adopt two possible solutions to decrease the impact of clouds: choosing cloud-free images or constructing temporally composited data (Holben, 1986; Los et al., 1994; Gallo and Owen, 1999). For example, several SUHI studies only examined the nighttime thermal images (Matson et al., 1978; Streutker, 2003; Tomlinson et al., 2012; Zhou et al., 2011; Tiangco et al., 2008), because the solar radiation increases the instability of boundary layer during the daytime, which is more likely to form clouds. Meanwhile, the cooling differences due to energy budgets between the urban and surrounding rural areas are maximized (Voogt and Oke, 2003). As a result, nights are usually under calm and clear conditions. Some research (Tan et al., 2006; Chen et al., 2006; Kato and Yamaguchi, 2005) was based on case studies in a short time period by selecting representative cloud-free LST images. However, this way is not suitable for continuous monitoring or for a large area investigation. On the other hand, temporal composite products can minimize the number of gaps created by clouds or any other undesirable

conditions in the long time series (Gallo and Owen, 1999; Pinty et al., 2002). Sometimes, it is preferred to use a coarser temporal resolution of remote sensing data over a long observational period, so that the SUHI analyses can be based on high clear-sky-coverage and consistent-repeat-period data.

SUHI studies, particularly for long-term or global analyses, commonly adopt temporally composited remote sensing. Composite data directly increase the clear sky coverage across urban and rural regions, which are beneficial to do spatial comparison for SUHI studies. For example, Gallo and Owen (1999) used monthly and seasonal Advanced Very High Resolution Radiometer (AVHRR) composites to analyze the SUHI effect, recommending monthly composites for summer and fall and biweekly composites for winter. Schwarz et al. (2011) used monthly composite LST generated from Moderate Resolution Imaging Spectroradiometer (MODIS) 8-day LST to explore indicators for quantifying SUHI of European cities. Unfortunately, these SUHI studies did not consider the possible errors caused by composite processes.

Normalized Difference Vegetation Index (NDVI) is one of a few biophysical variables that has been discussed for temporal compositing methods and associated biases. Compositing NDVI from AVHRR by the Maximum NDVI (MaN) compositing method results in a positive bias (Moody and Strahler, 1994). Moreover, the magnitude of biases depends on the composite methods. The composite maximum NDVI of AVHRR suggests significantly higher and generally less variable values when using MaN method rather than using Maximum Temperature (MaT) (Roy, 1997). Also, Tan et al. (2006) pointed out that MODIS 8-day composites of NDVI are overestimated by MaN and minimum blue method due to gridding artifacts. However, the processing methods and properties of LST are dissimilar with NDVI. The results may be not applicable to LST.

LST properties are a result of surface–atmosphere interactions and energy budget considerations, closely related to surface conditions (such as emissivity, land cover and structure, and moisture), subsurface properties (such as conductivity and specific heat density), and atmospheric properties (such as solar radiation, wind speed, and clouds) (Norman et al., 1995; Roy, 1997). Meanwhile, the characteristics of AVHRR and MODIS sensors are different in many ways, such

as spectral range and instantaneous field of view. As a result, the bias magnitudes may vary from different sensors. The product of composite MODIS LST released from NASA utilizes another aggregation method, simply by averaging the daily MOD11A1 product (Wan, 2007). The main bias is expected to be introduced by clouds, because the distinct urban climate system exerts influences on cloud occurrence frequency (Taha, 1997; Romanov, 1999), leading to the urban/rural data availability difference. However, what is the impact of temporal aggregation on MODIS LST is still unknown. In this paper, we examine this issue by focusing on Houston, Texas and its rural surroundings estimating the magnitudes of the influence of temporal aggregation on MODIS LST products for long term SUHI studies.

2.2 Study area

Houston, Texas is chosen as the study area in the domain ranging from 31.0° N, 97.0° W (northwest) to 28.5° N, 94.0° W (southeast) (Fig. 2.1). Houston is a coastal city on the Gulf of Mexico with a population of 2.1 million within about a 1600 km^2 urban area (United State Census Bureau, 2010). The climate is classified as humid subtropical, which is characterized by hot, humid summers and generally mild to cool winters. The land cover types in the study area according to MODIS land cover data from 2001 to 2009, except sea and land water (21.6%), primary include cropland/natural vegetation mosaic (28.3% ± 6.8%), woody savannas (13.5% ± 4.6%), croplands (11.7% ± 2.5%), grasslands (9.1% ± 2.6%), mixed forest (7.2% ± 2.8%) and urban and built-up (3.9% ± 0.03%). Fig. 2.1 illustrates the land cover in 2009 with the super neighborhood boundary (SNBR, from COHGIS 2010 (`http://cohgis.houstontx.gov/cohgis2010/index.html`)). The SNBR portrays the main Houston urban area without extra roads and small pieces of land outside main urban region, so we use it as the boundary of the Houston urban area instead of the administrative boundary in the later analyses.

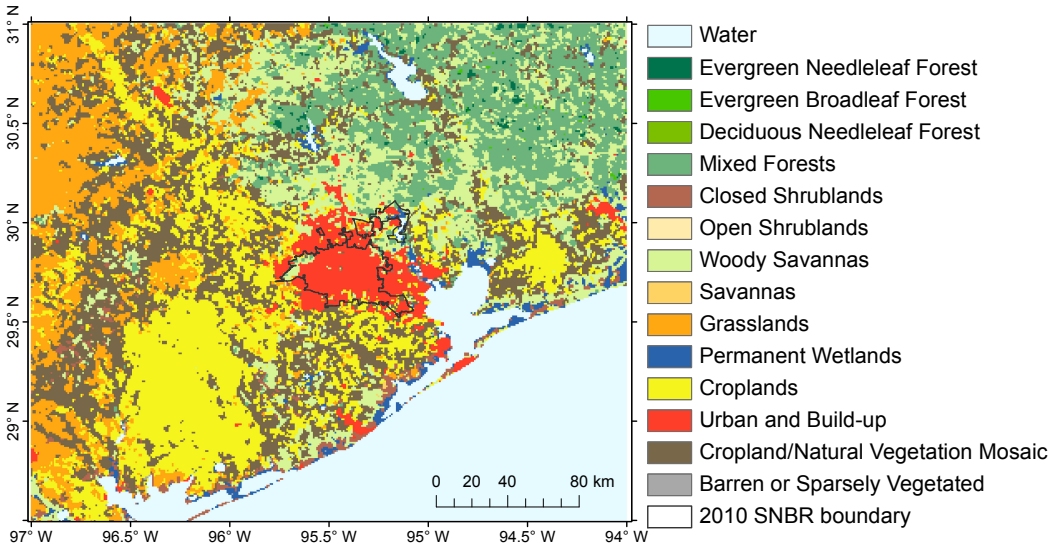

Figure 2.1: MODIS land cover map (International Geosphere Biosphere Programme (IGBP) classification) in 2009 with the super neighbourhoods boundary (SNBR) which is assigned as the Houston urban area in this study.

2.3 Data and Methods

2.3.1 Data and Data Processing

We used the daily (MOD11A1/MYD11A1) and 8-day composite (MOD11A2/MYD11A2) MODIS LST products from Mar. 5th, 2000 (MOD11A1; Jul. 8th, 2002 for MYD11A1) to Dec. 31st, 2010 at 1 km spatial resolution. MODIS is a 36-band instrument aboard the Terra (EOS AM) and Aqua (EOS PM) satellites, which covers the earth surface 4 times each day at the daytime (around 10:30 and 13:30 local time) and nighttime (around 22:30 and 1:30 local time). The MOD11A1/MYD11A1 products are produced daily using the generalized split-window LST algorithm (Wan and Dozier, 1996). The emissivities in bands 31 and 32 in the products are estimated by the classification-based emissivity method according to the land cover types (Wan and Dozier, 1996).

All sea pixels were excluded after reprojection and extracted from the subset of the study area. Considering both the location and the climate in Houston, we also masked the unreasonable LST values before analyses. According to the low air temperature record from NOAA Online

Weather Data (www.nws.noaa.gov/climate/xmacis.php?wfo=hgx) and considering the relationship between surface and air temperature (Jin and Dickinson, 2010; Sun and Mahrt, 1995), we set the low threshold of 280 K for May to September, and 258 K for other months. There are two images available for each daytime and nighttime. In order to simplify the comparison, we used the average of daytime or the average of nighttime values, although each pair was obtained approximately 3 h apart. This process is done after the separately aggregating Terra and Aqua images. In addition, only the first 360 days were accounted for statistics, so that 8-day composite LST dataset can match the daily dataset better in a one year period.

The MODIS land cover type product (MCD12Q1, 500 m, yearly) was introduced to explore the impact of temporal aggregation in a spatial perspective. We chose International Geosphere Biosphere Programme (IGBP) classification out of five schemes in MCD12Q1, which includes 17 classes with natural vegetation, developed and mosaicked land, and non-vegetated land classes. After being projected to the same coordinate system as the LST data, the land-cover maps were resampled to 1 km using the majority resampling method. Unfortunately, there are only 9 annual land cover maps available from 2001 to 2009 online, while LST datasets have a wider time series span (2000–2010), so the 2000 and 2010 LST data were assessed using the nearest year 2001 and 2009, respectively.

2.3.2 Analysis Methods

UHI is defined by the temperature differences between urban and non-urban areas. However, the differentiation between "urban" and "rural" remains diverse (Schwarz et al., 2011). In this study, we defined the urban temperature using mean urban LST in SNBR boundary of Houston. Then, the temperature differences (also called SUHI maps) were calculated from

$$\Delta T(i,j) = \bar{T}_{urban} - T(i,j) \tag{2.1}$$

where $\bar{T}_{urban}$ is the mean of LST in SNBR boundary with the land cover type of urban and

built-up, and T(i,j) is a pixel in the LST image at the position of (i,j). Generally, the non-urban areas reflect positive values in SUHI maps, which indicate the LST difference magnitudes between the Houston urban and the non-urban areas.

Daily and 8-day composite LST values of Houston and non-Houston areas were calculated and compared to show the seasonal, annual, and interannual dynamics of urban–rural climate. Then, the impact of temporal aggregation on SUHI was evaluated from two points of views: time and space. The analyses of the temporal aggregation were aimed to test whether the impact of aggregation varies with time of year, while the spatial analyses were attempting to ascertain what the impact of the aggregation has on the spatial variance. The major statistics were calculated using MODIS daily and 8-day composite data, because 8-day composites are a primary MODIS LST product, and the clear sky coverage at this scale is generally high enough for common spatial analyses.

To assess the influence of temporal aggregation, we estimated 2-, 4-, 8-, 16-, and 32-day composite scales of SUHI maps based on daily LST using a moving window algorithm. This resulted in a composite LST image from each fixed composite period (window size: from 2 to 32 days) and moves the window forward day by day, then estimated the SUHI from these composited LST images. The mean SUHI magnitudes in study area at each composite scale were calculated before estimating the mean SUHI from Terra and Aqua. Then the mean SUHI were compared with daily mean SUHI in the same period. Moreover, to evaluate the cost and gain, the clear sky coverage ratio (R_{csc}) was calculated based on each composite LST image:

$$R_{csc} = \frac{N_{cs}}{N_{total} - N_{sea}} \tag{2.2}$$

where N_{cs} is the total number of land surface pixels under clear sky conditions, N_{total} is the total number of pixels in an image, and N_{sea} is the number of masked sea pixels.

Regression analyses for day and night were performed on 8-day averages of daily SUHI versus the SUHI derived from the 8-day composite data, respectively. Such analyses were also undertaken for seasonal relationships. To evaluate the 8-day composite data performance, coefficient

of determination (R^2), root mean square error (RMSE), and slope and intercept of the regression were calculated. Moreover, the differential SUHI maps between 8-day composite images and the corresponding daily images were calculated and the seasonal statistics were calculated.

In order to explore the spatial variability caused by temporal aggregation, summer composite SUHI maps during 11 years were generated from daily and 8-day composite LST as well as their differential maps for day and night, respectively. Land cover is a critical forcing for development of the UHI (Jin and Shepherd, 2005), and the relationship between UHI and land cover has been reported widely in the literature (Voogt and Oke, 2003). We statistically analyzed the mean SUHI magnitudes of each main land cover type at summer-season and annual periods to assess the responses of different land cover types to the temporal aggregation.

To quantify the potential influence of cloud contamination on the aggregation product, the linear aggregations were tested between R_{csc} and aggregation biases at the 2-, 4-, 8-, 16- and 32-day composite scales. The aggregation biases are generated from the differences between the mean composite SUHI in the study area and the daily mean SUHI in the composite period. Moreover, the spatially heterogeneous distribution of clouds was also assessed seasonally by calculation of the available pixel ratio (APR) maps (Spring MAM, Summer JJA, Autumn SON, and Winter DJF). APR is defined as follows:

$$APR(i,j) = \frac{\sum_{z=1}^{N} n(i,j,z)}{N} \tag{2.3}$$

where n is 1 when the value of the pixel at (i,j) is meaningful (non-NaN), otherwise n equals 0; N is the total number of images in each season. APR maps are directly derived from the daily dataset, because this originally reflects the cloud contamination frequency. A higher APR value means less cloud contamination during this season at this pixel.

2.4 Results

2.4.1 Temporal Aggregation Influence on LST in the Urban and Rural Areas

We began by focusing on the temporal LST patterns of Houston and the surrounding areas. The mean daily average LSTs of 11 years are $301.1 \pm 6.5K$ (daily), 302.7 $\pm$ 6.8 K (8-day) in the Houston urban area, and 297.8 $\pm$ 6.5 K (daily), 299.2 ± 6.3 K (8-day) in the non-Houston area during the daytime. For the nighttime, the mean LSTs are lower than those during the daytime, which are 289.8 $\pm$ 7.2 K (daily), 289.7 $\pm$ 7.0 K (8-day) in the Houston urban, and 287.9 $\pm$ 7.1 K (daily) and 287.8 $\pm$ 6.9 K (8-day) in the non-Houston area. The 8-day composite LST shows higher temperatures in the daytime and lower temperatures at night, which increases the diurnal LST by 1.7 K (the Houston urban) and 1.5 K (the non-Houston area), respectively.

The mean daily, seasonal, annual and interannual LST patterns assessed by daily LST in the Houston urban and the non-Houston urban area are shown in Fig. 2.2. There is a marked seasonal trend of the mean LST. Compared with the mean LST in 45 8-day periods between the two datasets, the annual trend doesn't agree well in quantitative features (Paired t-test,$p < 0.01$) in the daytime with mean differences (8-day minus daily) about 1.9 K (Fig. 2.2a) and 1.5 K (Fig. 2.2b). However, these differences are not statistically significant during nighttime (Fig. 2.2c and Fig. 2.2d). Moreover, the composited data are generally less varied due to the aggregation reducing the LST range. The standard deviation (STD) shows a different diurnal and seasonal pattern for the urban and non-urban areas. There is a relative higher STD in summer during the daytime in the Houston urban area, and in contrast, the STD is notably lower in summer during nighttime in both Houston and non-Houston areas.

The interannual comparison was also conducted from 2000 to 2010 (Fig. 2.2). The statistics show that the mean 8-day LST is always higher than that of the daily dataset during the daytime, while the nighttime mean LST is opposite. The t-test indicates that the annual differences between the two datasets are not significant.

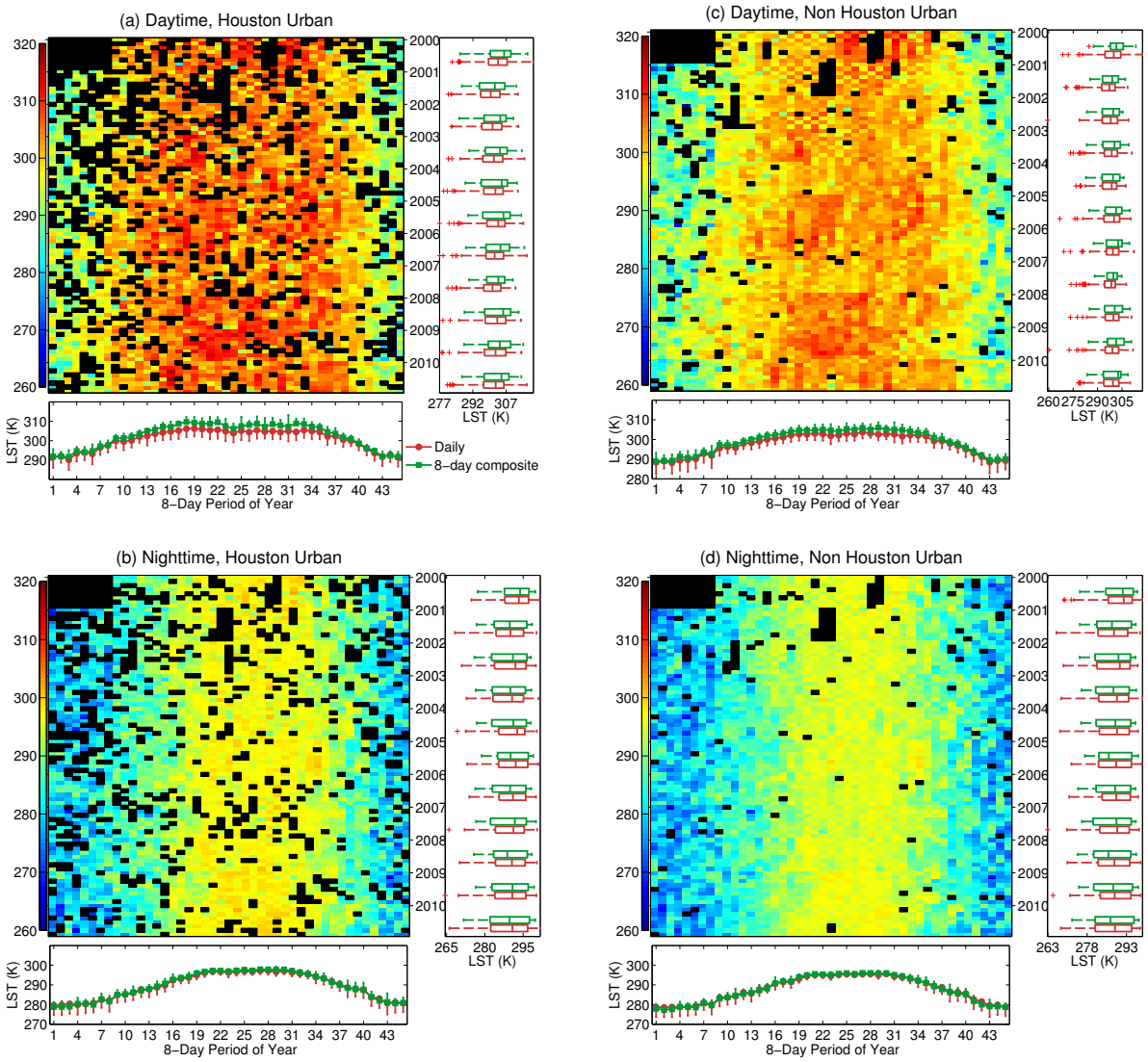

Figure 2.2: The daily average LSTs of Houston urban and non-Houston urban areas during 11 years. The daily average LSTs are arranged as 8-day period by 45 8-day periods in a year by 11 years. The missing values are in black. The bottom plot shows the mean and standard deviation (STD) in every 8-day period using daily (red, downward error bar) and 8-day composite data (green, upward error bar). The right box-plots illustrate the distributions of daily (red) and 8-day composite data (green) LST in each year.

2.4.2 Temporal Aggregation Influence on Temporal Dynamics of SUHI

2.4.2.1 Multi-scale Composite SUHI Comparisons

In order to examine the impact of the time scale of temporal aggregation on SUHI as well as on the clear sky coverage, the 2-, 4-, 8-, 16-, and 32-day temporal composites were calculated by the moving window algorithm. The 11-year mean of statistics were plotted in Fig. 2.3, showing the annual trend of daily and multi-scale composite SUHI magnitudes. The interannual variation of the SUHI (not shown figure) in summer day is relatively larger than other seasons with the standard deviation of 2.4 K at the daily scale and 2.2 K at the 8-day scale, resulting in slightly higher variation of biases. However, the variations of the biases at 6 temporal scales are less than 1.6 K in the summer day. Conversely, the summer nights exhibit smaller variations of SUHI and the aggregation biases during the 11 years than other seasons, which are also much smaller than daytime. The seasonal pattern of SUHI in each scale is clear, indicating higher SUHI values in spring and autumn. With the increasing composite scale, the SUHI values are more notably enhanced in the daytime than nighttime. We compared the composite SUHI with the daily scale and found that the summer shows the largest variation (Fig. 2.3(b)) with about 3.5 K at 32-day composite scale for the day, while the temporal scaling exerts less influence in winter. The impact is also less at night than during day, showing relatively similar values at night in Fig. 2.3(d).

The advantages of utilizing composite data include the high efficiency for long term monitoring, as well as the great improvement of clear sky coverage which is essential for spatial analyses. The 11-year-averaged annual clear sky coverages at six scales are shown in Fig. 2.4. Since the compositing process decreases the cloud coverage by adding more information, the clear sky coverage increases as an increase of composite time period, which is greatly affected in a short composite period, compared with 0.44 for daily LST, 0.61, 0.80 and 0.93 at 2-, 4- and 8-day levels during the daytime, respectively. Based on daily data, the clear sky coverage differs substantially in summer for day (0.36) and night (0.54) due to diurnal energy balance patterns in urban environments. Generally, when the composite scales are greater than the 8-day period, the SUHI maps in a year long

period can reach a high quality of clear sky coverage for both day and night, and with a seasonal analysis, a shorter compositing period can result in the similarly high quality.

One of the primary issues associated with temporal scaling of SUHI from remote sensing is that cloud contamination determines the availability of SUHI maps and the magnitudes of SUHI related to the mean urban LST. We will discuss this issue in further details in Section 2.4.4.

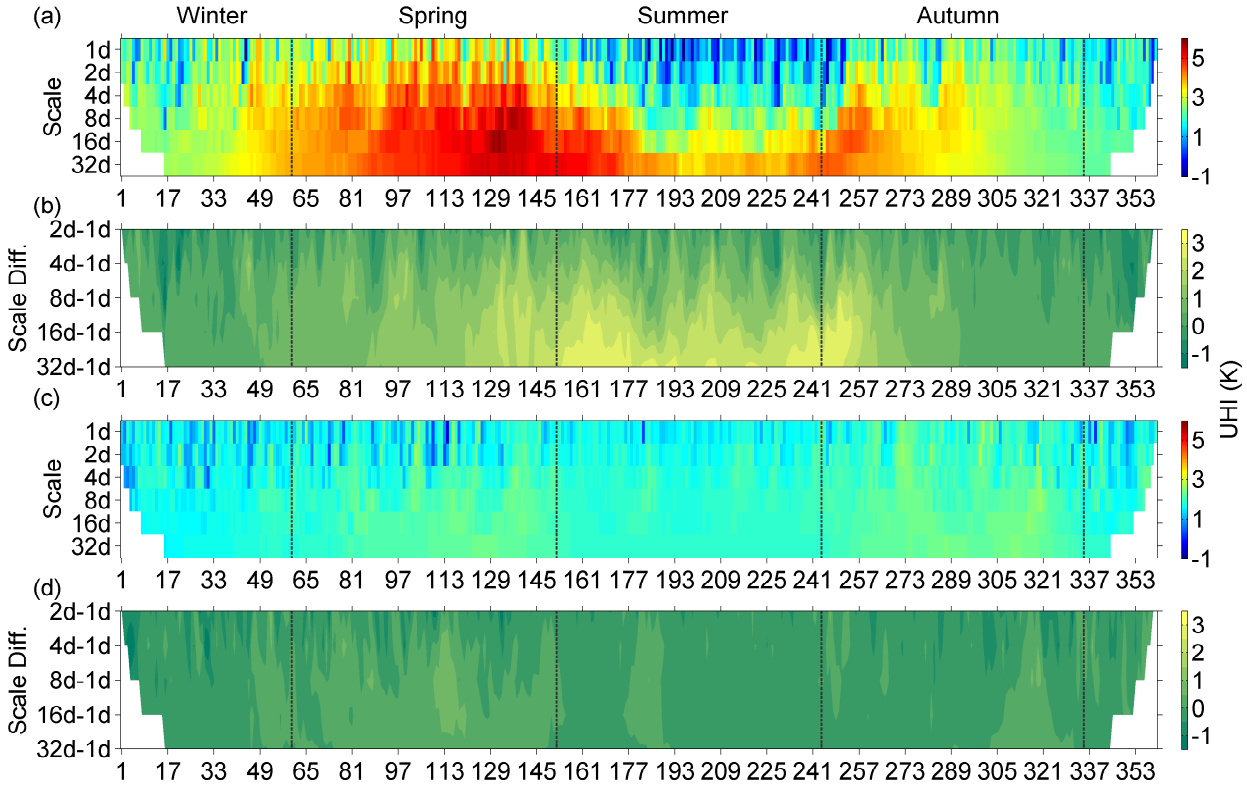

Figure 2.3: The 11-year mean SUHI of study area at daily and 2-, 4-, 8-, 16- and 32-day temporal composites for day (a) and night (c) with their SUHI differences for day (b) and night (d). The SUHI differences are calculated from the difference between composite SUHI and the mean SUHI using the daily SUHI during the corresponding period. The four vertical lines separate a year into four seasons.

2.4.2.2 Linear Regression Analysis Between Daily and 8-day Composite SUHI

The trend in the improvement of the clear sky coverage resulting in an increased error of SUHI is clear. Next, we scrutinized daily and 8-day composite LST product available online to quantify the errors. A scatter plot of the mean daily SUHI during 8-day period versus the 8-day composite

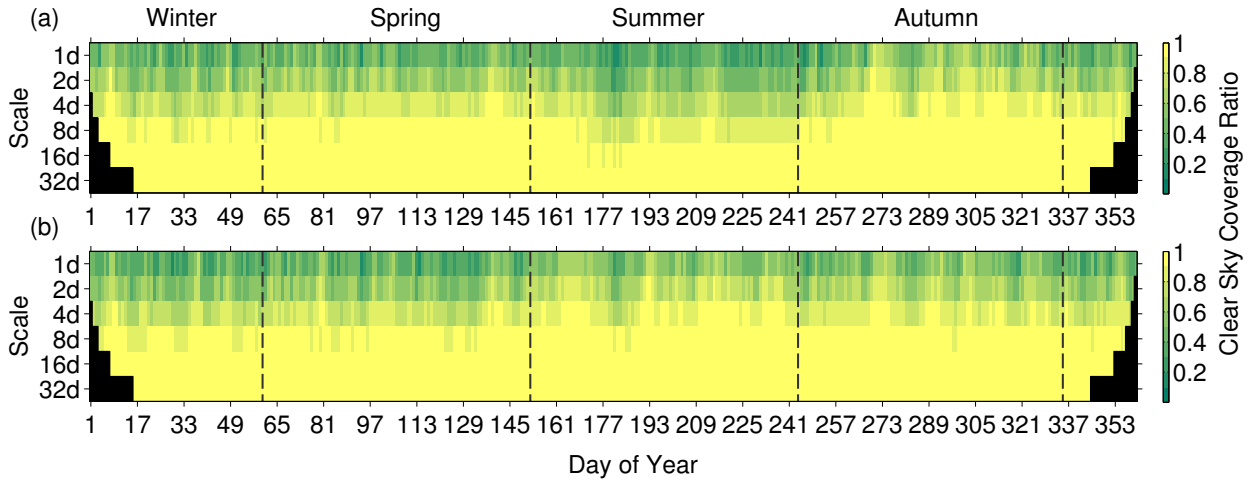

Figure 2.4: The 11-year mean clear sky coverage ratio (R_{csc}) for each composite scale image at day (a) and night (b).

SUHI from early 2000 to 2010 for day and night, respectively (Fig. 2.5), examines the influence of temporal aggregation on SUHI. At first glance, the aggregation process directly results in a higher SUHI magnitude than that using daily SUHI, especially in the daytime. Similar regression analyses were also implemented at a seasonal scale, and the results are shown in Table 2.1. The 8-day composite SUHI differed seasonally from the daily SUHI. The stronger R^2 in summer during the daytime explains the variation of 8-day composite SUHI caused by the variation of daily data. Spring has the largest absolute bias, as high as 2.5 K in the daytime. For the nighttime, the spring shows the highest R^2 and a slope of near 1. Generally, the SUHI estimated from the two datasets indicates a smaller difference during the nighttime.

Table 2.1: The statistical results from the regression between daily and 8-day composite SUHI from 2000 to 2010

Season	Daytime				Nighttime			
	Slope	Intercept	R^2	RMSE	Slope	Intercept	R^2	RMSE
Spring	0.57[†]	2.49	0.35	0.80	0.91	0.32	0.68	0.32
Summer	1.14	1.56	0.75	0.67	0.73	0.64	0.51	0.13
Autumn	0.95	0.95	0.51	0.61	0.83	0.49	0.51	0.18
Winter	0.88	0.55	0.51	0.51	0.83	0.24	0.28	0.29
Annual	0.86	1.35	0.56	0.94	0.86	0.35	0.51	0.25

[†] The t-test results are not significant (p-value$>$ 0.05) at 95% confidence level.

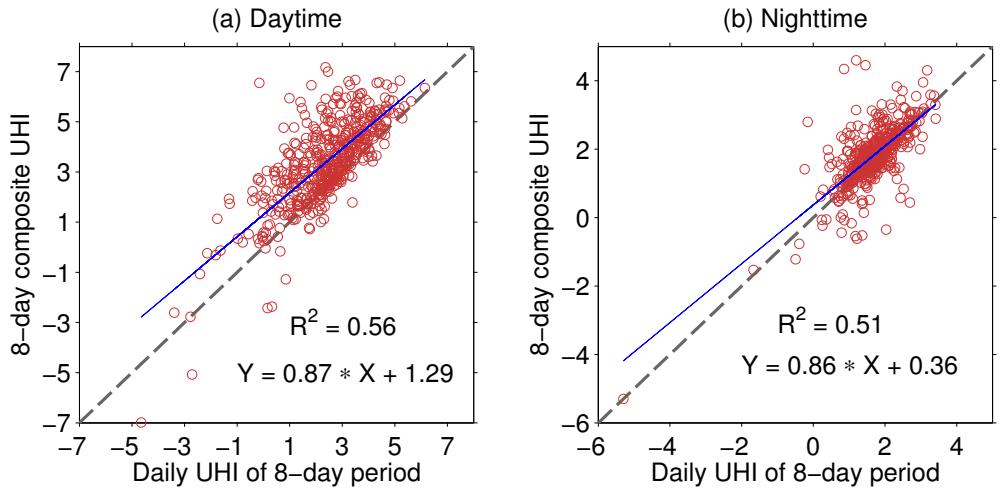

Figure 2.5: Scatter plot showing the average of daily SUHI images in 8-day period against its corresponding 8-day composite SUHI value across the study area.

2.4.2.3 Statistics of SUHI Dynamics from Daily and 8-day Composite Data

The annual SUHI trends using daily and 8-day composite datasets were calculated and plotted in Fig. 2.6. Agreeing with the regression result, the 8-day aggregation of LST generally enhances the SUHI during the daytime, and the effects become greater in the warm seasons rather than the cold seasons. The influence on the nighttime SUHI is comparatively less notable. The aggregation increases 1.4 K of pseudo median in the daytime and 0.4 K for the nighttime in Wilcoxon Signed-Rank test, which are significantly different ($p < 0.01$). Additional statistics of the seasonal mean SUHI with its STD are listed in Table 2.2. We observed a strong seasonal pattern of SUHI in the daytime, illustrating about $1 \sim 2K$ K higher mean SUHI in spring and autumn than summer. The nighttime mean SUHI is quite stable, which differs less than 0.5 K among seasons. The seasonal mean SUHI differences between 8-day composite and daily datasets varied with a remarkable diurnal pattern. Generally, the aggregation causes few differences at night, especially in winter; the effects are greater with seasonal variations in the daytime. The largest mean gap is as high as 1.8 K during 11 years, and occurs in the summer.

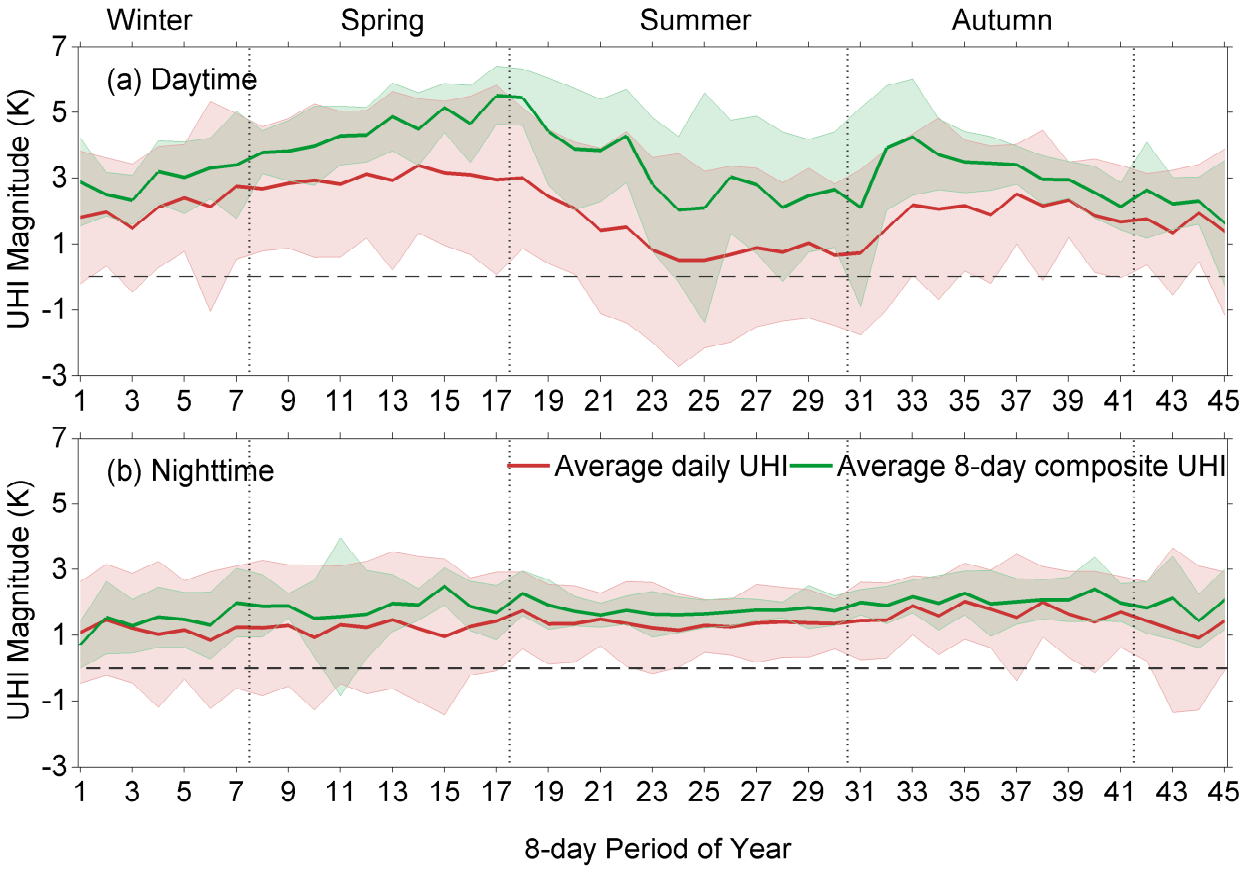

Figure 2.6: The mean 8-day period SUHIs from daily and 8-day composite dataset during 11 years for day and night. Green line represents the mean 8-day composite SUHI and the light green area shows the range between the mean value $\pm$ 1 STD. The red line depicts the daily mean SUHI magnitude arranged in 8-day periods and the light red area shows the daily mean value with $\pm$ 1 STD. The vertical lines separate a year into four seasons. The corresponding statistics refer to Table 2.2.

Table 2.2: The seasonal statistical results of 8-day period mean SUHI and the STD

Seasons	8-day period of year	Day (K)		Night (K)		Day (K)	Night (K)
		Daily	8-day	Daily	8-day	8-day - Daily†	8-day - Daily†
Spring	8-18	3.0±2.3	4.6±1.1	1.3±1.8	1.9±1.1	2.2	0.5
Summer	19-30	1.0±2.6	2.8±2.2	1.3±1.1	1.7±0.5	2.8	0.4
Autumn	31-41	2.0±2.1	3.2±1.2	1.7±1.3	2.1±0.7	1.6	0.2
Winter	1-7,42-45	1.9±2.1	2.8±1.2	1.2±1.9	1.6±1.0	0.8	0.3

† This is the statistics from the differential maps generated from the 8-day composite SUHI minus the corresponding daily SUHI.

2.4.3 Temporal Aggregation Influence on the Spatial Pattern of SUHI

The primary purpose of comparing the spatial differences is to characterize how much spatial variation is introduced as a result of temporal aggregation. As shown above, the largest SUHI differences during the day occur in summer, so we chose this season to assess the spatial variability. The summer mean SUHI maps during 11 years, as well as their differences for both day and night are shown in Fig. 2.7. Some negative values in the Houston urban area are due to the definition of SUHI in Eq. 2.1, where they have higher LST than the mean Houston urban LST. The SUHI shows a higher magnitude in the daytime composite dataset, and especially in the northeastern corner of the domain. Linking SUHI with the land cover map shown in Fig. 2.1 turns out to be a similar pattern. Nighttime SUHI maps and their differential map, which are more homogeneous, indicate that there is no remarkable spatial variation caused by the temporal composite process at night, which just consolidates the results in Section 2.4.2.

The major land cover types cluster regionally with relative homogeneity, the northeastern corner of which is primarily covered by mixed forest and woody savannas. To further assess the possible reason causing the spatial difference during the day time as well as the magnitude of the response, we introduced the land cover maps (MCD12Q1) to build a relationship between SUHI and the main land cover types (Fig. 2.8) for both summer and annual scales.

Since the SUHI accounts for smaller urbanized areas outside of Houston, the urban SUHI has a value slightly higher than zero due to comparing with the mean Houston LST, which agrees with the findings that the smaller cities are with a lower SUHI intensity (Oke, 1973). SUHI magnitudes of mixed forest and woody savannas are apparently higher than grassland, cropland and

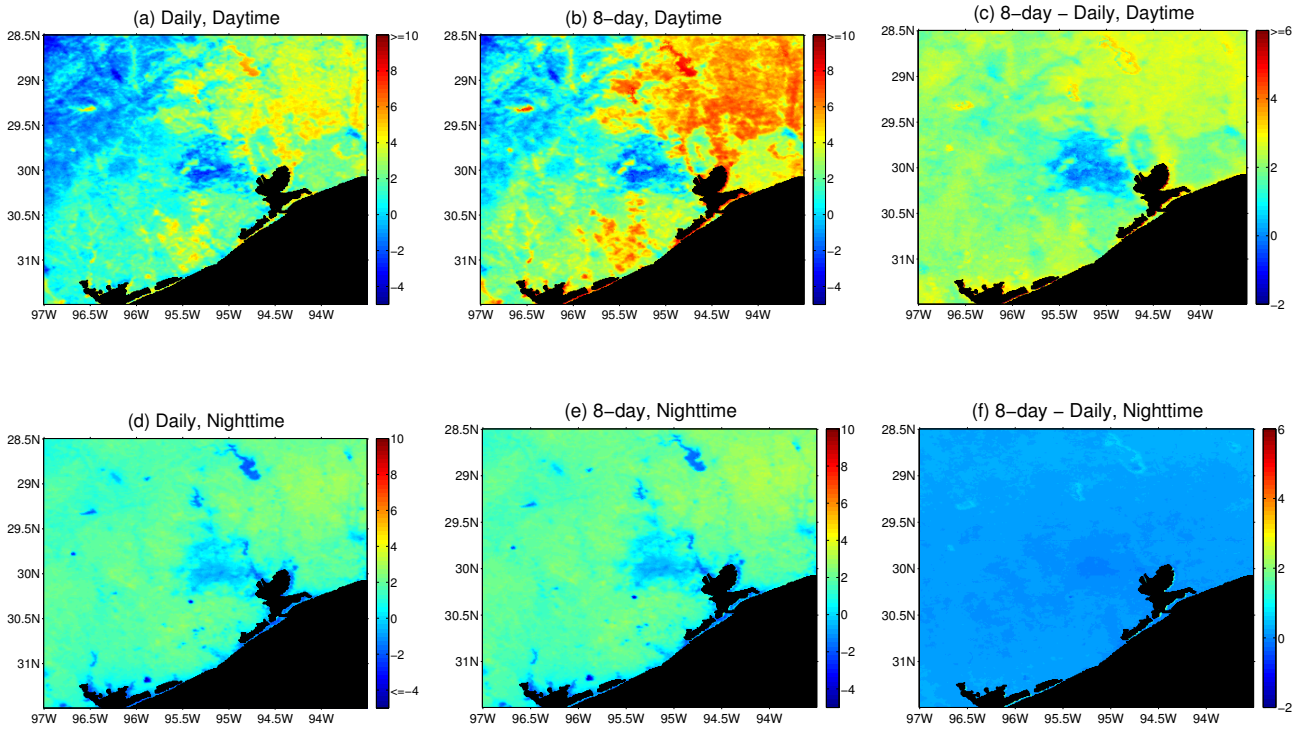

Figure 2.7: Mean summer SUHI for day and night using daily and 8-day composite datasets, and their SUHI difference maps.

cropland/natural vegetation mosaic in the daytime, which can be explained by the lower albedo and the higher evapotranspiration ability of trees enhancing the available net radiation and losing more energy through latent heat flux. In the summer day, the LST of grass is even higher than the urban LST, which shows a negative mean SUHI in Fig. 2.8(c).

The distinct diurnal pattern results from the change of energy budgets between day and night, and this difference also can be found between daily and 8-day composite data. With the exception of grass, the distributions of 8-day composite SUHI are generally more concentrated than daily, due to decreasing the variation by averaging daily values. The statistical test results show that the differences of the two datasets in each land cover types are significant (Welch's t test, $p < 0.01$), with a mean difference of about 1.3 K (annual) and 1.7 K (summer) for the day, and about 0.4 K (annual) and 0.3 K (summer) at the night. Further details are shown in Table 2.3. These results imply that the higher SUHI regions are more likely to have a larger gap between two composite scales in the daytime.

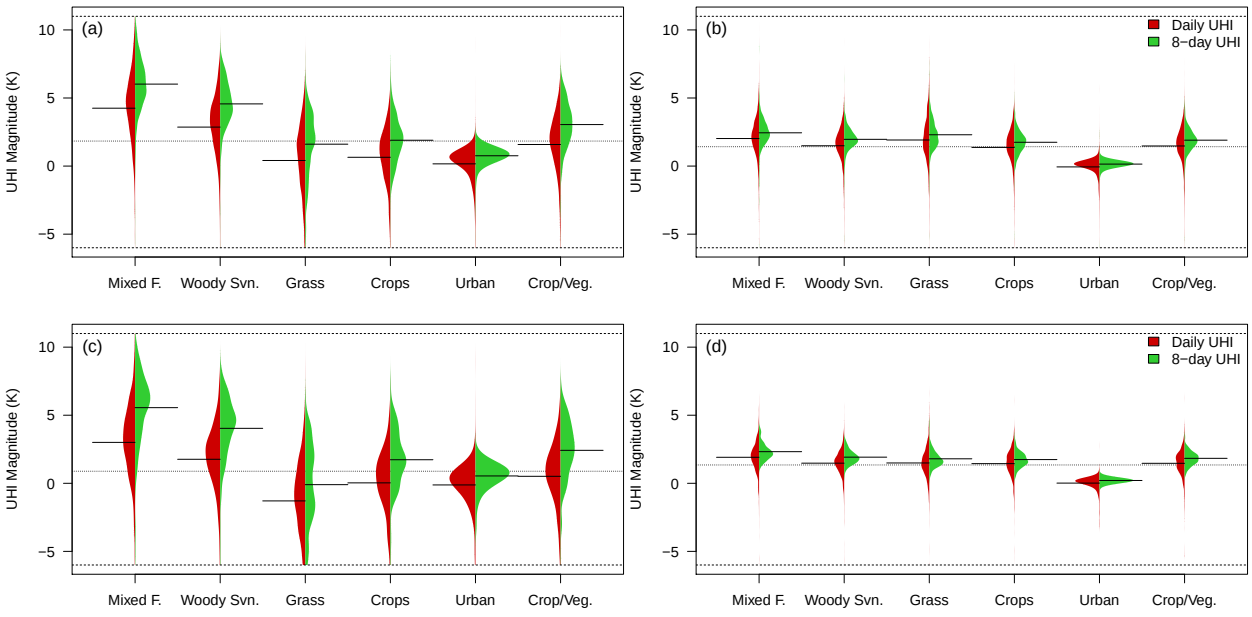

Figure 2.8: SUHI of daily and 8-day composite data with major land cover types in the study area. (a) and (b) are the daytime and nighttime SUHI for annual scale. (c) and (d) are daytime and nighttime SUHI only for the summer period.

Table 2.3: The mean SUHI based on land cover maps using daily and 8-day data

Land Cover Types	Day (K)				Night (K)				Day (K)		Night (K)	
	Daily(a|s)†		8-day(a|s)		Daily(a|s)		8-day(a|s)		Diff.‡(a|s)		Diff.(a|s)	
Mixed forest	4.3	3.0	6.0	5.6	2.0	1.9	2.4	2.3	1.9	2.9	0.3	0.4
Woody savannas	2.9	1.8	4.6	4.0	1.5	1.5	2.0	1.9	2.0	2.8	0.4	0.4
Grassland	0.4	-1.3	1.6	-0.1	1.9	1.5	2.3	1.8	1.7	2.5	0.3	0.4
Cropland	0.6	0.03	1.9	1.7	1.4	1.4	1.8	1.7	1.8	2.6	0.4	0.4
Urban/Build-up	0.2	-0.1	0.8	0.5	-0.1	0.01	0.1	0.2	1.6	2.4	0.2	0.3
Crop/Veg. mosaic	1.6	0.5	3.0	2.4	1.6	1.5	1.9	1.8	1.9	2.8	0.4	0.4

† a|s represents the mean SUHI of annual (a) and summer period (s), respectively.
‡ Diff. is the mean difference between 8-day composite SUHI and daily SUHI.

2.4.4 Influence of Clouds

The SUHI is composed of the differences between urban and rural LST, and missing either LST cannot generate a SUHI map. Fig. 2.2 illustrates the influence of clouds showing missing LST with black pixels, suggesting that this influence becomes larger in urban than rural and in the daytime than nighttime. Statistically, about 76% (day) and 81% (night) of total daily LST images were valid (cloud free) for Houston urban area LST to generate SUHI maps. 8-day composite product shares a higher proportion (above 98%), due to increasing the LST availability through a series of images. Similar results can be found in Fig. 2.4.

The benefit of temporal compositing is significant; however, it may result in a biased of SUHI quantification using an aggregated dataset. Fig. 2.9 shows the linear relationship between the R_{csc} and the aggregation biases at the 8-day composite scale. Due to the large variation of aggregation effect in summer, the 2-, 4-, 8-, 16-, and 32-day composite aggregation biases in summer were analyzed for day and night, respectively (Table 2.4). As the length of the composite period increases, the R_{csc} grows quickly resulting in a more concentrated distribution without a significant linear relationship. Hence, Fig. 2.9 only shows the regression lines with statistically significant level ($p < 0.05$). The slope of regression lines is positive, showing an increase in bias with a growing R_{csc} in the daytime. Also, the composite scale matters, which matches the results from Fig. 2.3, showing a larger slope with a longer composite period. In contrast, the increase in cloud ratio results in a decrease in error, which is close to zero at the high R_{csc} end. Moreover, the composite scale does not greatly affect the biases from the aggregation process. It is postulated that the large

cloud coverage decreases LSTs, and although the cloud and cloud-contaminated pixels have been removed (Wan, 2008), a residual cloud impact possibly exists on the adjacent pixels. For example, clouds cause the changes of energy and water balances, which affect the surrounding non-cloud pixels. The increase of R_{csc} by aggregation actually does not physically compensate for the cloud effects, especially for the daytime due to the relatively low clear sky coverage (Fig. 2.4). The diurnal distinction of the bias-R_{csc} relationships may be caused by the distributions of clouds exerting spatially variable impacts, leading to the variation of SUHI.

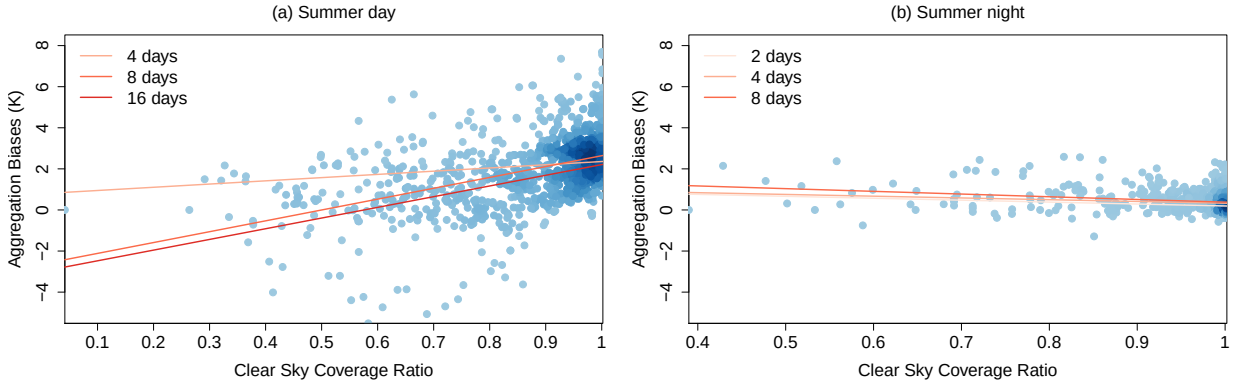

Figure 2.9: The scatter plot between 8-day composite clear sky coverage ratio (R_{csc}) and the aggregation biases at 8-day composite scale (blue points) for 11-year summers. The darker color indicates higher density at that point. Aggregation biases is calculated from the differences of composite SUHI and the daily mean SUHI in the corresponding period, refer to Fig. 2.3b,d. The regression lines are plotted only using statistically significant data.

Table 2.4: The statistics of linear regression analyses between clear sky coverage ratio (R_{csc}) and aggregation biases in 11-year summers

Composite Scale	Day		Night	
	Slope	Intercept	Slope	Intercept
2-Day†	-0.35	2.11*	-0.94*	1.14*
4-Day$^{\divideontimes}$	1.57*	0.79*	-0.85*	1.18*
8-Day$^{\divideontimes}$	5.28*	-2.64*	-1.31*	1.69*
16-Day‡	5.20*	-3.0*	-0.7	1.11*
32-Day	3.38	-1.43	0.57	-0.18

† Significant relationship of linear regression model for the night($p < 0.05$)
‡ Significant relationship of linear regression model for the day($p < 0.05$)
$^{\divideontimes}$ Significant relationship of linear regression model for both day and night($p < 0.05$)
* Significance of the slope or intercept ($p < 0.05$)

The enhanced SUHI is highly related to the characteristics of urban climate. The unstable boundary layer in the afternoon accelerates the generation of clouds above the urban area, which increases the cloud-contamination possibility at the time of the satellite overpass. The cloud contamination results in an absence of urban LST pixels, and thus it is difficult to calculate daily SUHI maps. While the composite values comparatively enhance the LST of areas around the city. Fig. 2.10 shows the daytime mean APR maps in the four seasons. A noticeable heterogeneity occurs in summer APR map (with STD of about 0.10), showing a lower ratio in Houston urban area and a higher one in northeastern corner. This trend matches the differential SUHI map in summer shown in Fig. 2.7. On the contrary, the more homogeneous winter APR map, with STD of about 0.04, explains well the smaller influence of temporal aggregation in winter (Table 2.2). Similarly, there is not a remarkable spatial bias of APR maps at night in each season (not shown), with the STD less than 0.05, although the mean APR value in summer is about 0.14 higher than that in winter.

A linear relationship was examined between APR and the SUHI difference map between 8-day and daily composite images in the summer during 11 years (Fig. 2.11). It turns out to be a strong positive correlation with R^2 of about 0.76, implying higher APR values with higher SUHI differences due to temporal aggregation. Also, a bias of land cover is exhibited in the APR maps, suggesting a relatively low APR with larger variance (such as urban and built-up areas, 0.15 ± 0.08 of APR with bias STD of 0.65 K) and high APR with a smaller variance (such as forest, 0.46 ± 0.04 of APR with bias STD of 0.19 K).

2.5 Discussion

The results suggest that the temporal aggregation of MODIS LST products leads to a more intensive SUHI effect with diurnal and seasonal patterns. We showed that the SUHI have a 1.29 K bias in the daytime and 0.36 K at night using 8-day composite dataset as compared to the daily dataset during 11 years across the study area. The seasonal variation suggests that it produces the highest potential difference at summer day due to 8-day scale aggregation, which is about 2.8 K.

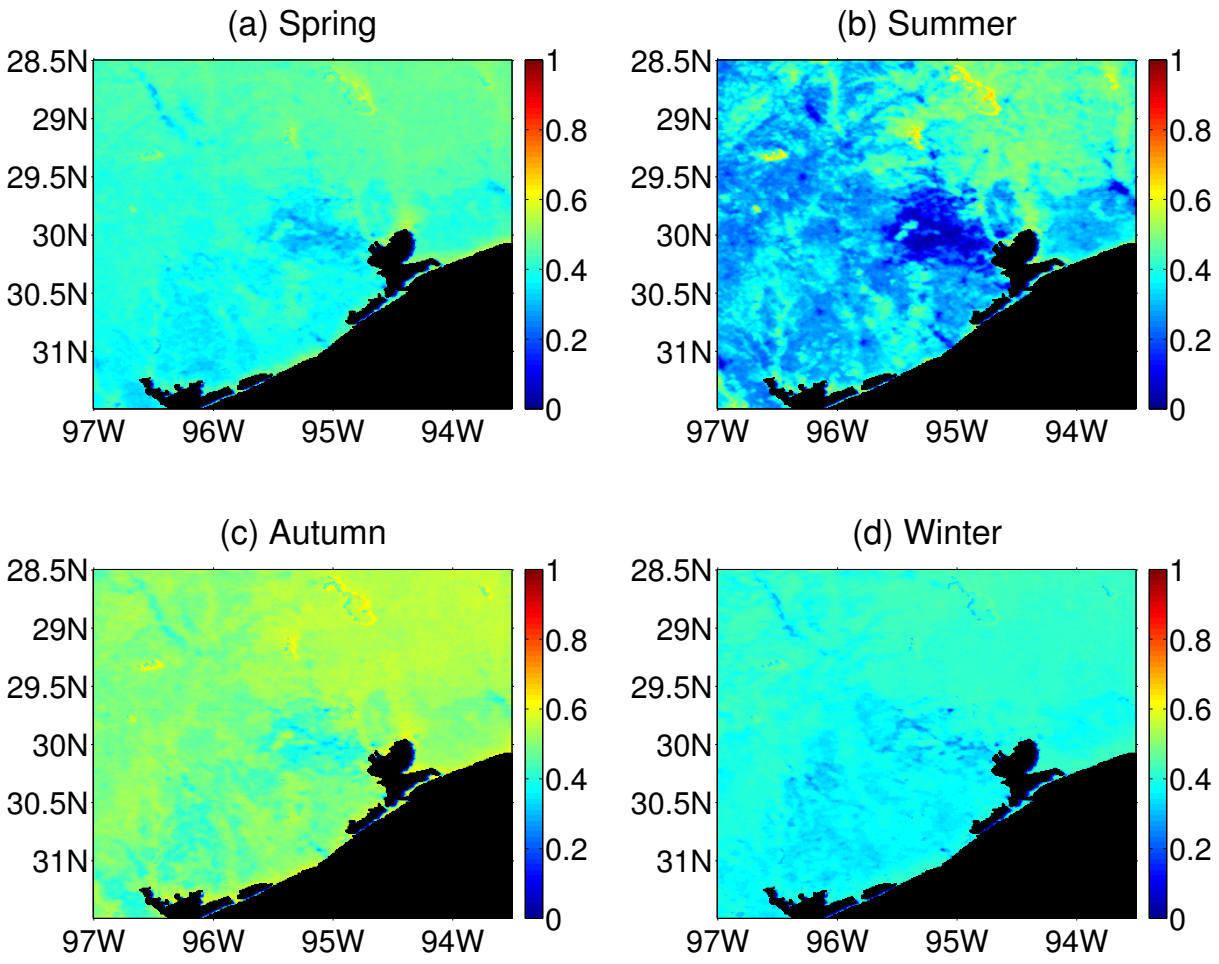

Figure 2.10: The available pixel ratio (APR) maps of four seasons for the day, which are generated according to Eq. 2.3.

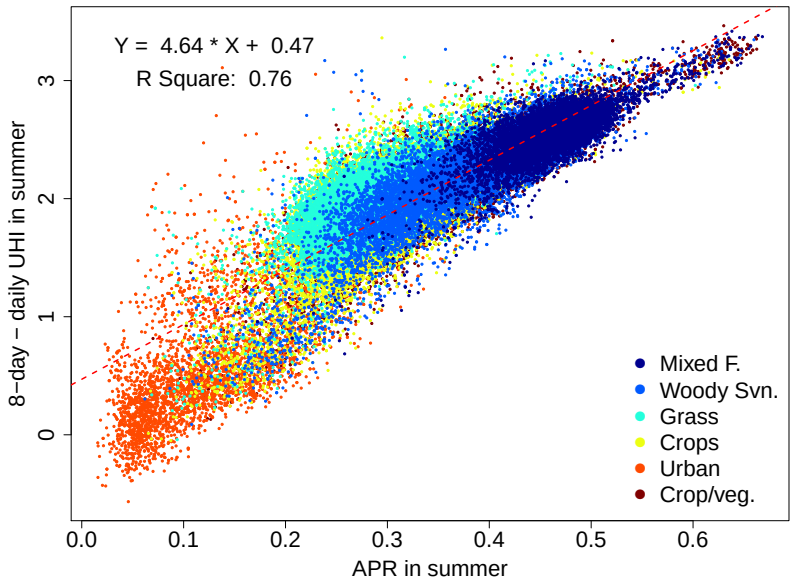

Figure 2.11: Regression analysis between the summer APR (Fig. 2.10b) and the differential SUHI map in summer (Fig. 2.7c) of six main land cover types.

In addition, the composite also has some impacts on the spatial distribution of the SUHI during the daytime, which is likely related to the land cover types.

The nighttime SUHI magnitude calculated from daily MODIS LST products is about 2.0 K during 11 years. Streutker (2003) pointed out that there was about 2 $\sim$ 3 K SUHI magnitude in Houston by nighttime AVHRR data between 1985 and 1987, and between 1999 and 2001. The mean LST surrounding Houston, which was about 290 K, was higher than the result we estimated. These differences may be attributable to the accuracy of AVHRR ($\pm$1.5K) (Prata, 1994) being lower, compared with MODIS ($\pm$1K) (Wan and Dozier, 1996). The heterogeneous surface, unavailable atmospheric conditions for correction, and sensor view angle more or less limit the quality of LST achieved from satellites (Jin and Dickinson, 2010). The differences are also caused by the designation of urban, rural, and the whole region of study area we defined. As there are many indicators used to define the SUHI in the literature, Schwarz et al. (2011) found that different indicators have weak correlations, and emphasized the importance of choosing methods to quantify SUHI effects. Hence, it is unclear how the choice of indicator will impact the aggregation results.

The diurnal SUHI shows that the midday SUHI magnitude of Houston is generally larger than

that in midnight. The seasonal patterns indicated that the highest SUHI magnitude occurs in the spring, and the lowest magnitude happens at summer in the midday. Nighttime SUHI variation of four seasons is not notable. Compared with global analyses from Zhang et al. (2010) and European cities from Schwarz et al. (2011), the Houston summer SUHI is generally about 1 K lower, and about 3 K lower than the settlements larger than 500 km^2 globally, however, it is not necessary indicating that Houston is not hot during summer. The absolute LST in the study areas is as high as 305.0 K in summer. It is probably because of the humid coastal climate, dominated biomes (Imhoff et al., 2010; Zhang et al., 2010), and the city structure which is sprawling (Streutker, 2003). However, it is hard to exclude the possible influence by this distinct seasonal pattern of SUHI in Houston, which may lead to decreasing universality of our results to other areas. Consequently, additional studies of other cities need to be done in the future.

A significant negative relationship between land surface temperature and NDVI is found in many studies (Dousset and Gourmelon, 2003; Gallo et al., 1993), which is associated with a decrease in surface resistance to evapotranspiration, a large portion of energy for latent heat flux, as well as a reduced Bowen ratio (Mildrexler et al., 2011; Mu et al., 2007). In this study, we used land cover maps instead of vegetation index for a more specified spatial pattern analysis. However, if linking the SUHI magnitude with NDVI, the trends will be similar, indicating that forest has the largest cooling effect (Mildrexler et al., 2011), particular in daytime (Lo et al., 1997). The SUHI analysis based on land cover types may exhibit some errors due to the coarse temporal resolution of land cover data, which may not perfectly match the actually situation during the year.

The bias of cloud contamination is a possible reason for increasing the SUHI magnitude using composited data. According to the research conducted by Romanov (1999) on the urban influence of the cloud cover, the results show that there is a considerable increase of cloud fraction in spring and summer while winter's urban effect is slight in the daytime, which matches our findings: 1) the seasonal trends (Fig. 2.10), and 2) the differences of SUHI caused by aggregation increase in spring and summer, and decrease in winter (Table 2.2). As the results shown in Section 2.4.4, cloud formation is closely associated with land–atmosphere interactions. Urban areas are likely

to be affected by clouds, due to their surface properties. The boundary layer heights over urban areas are generally higher than that over rural areas due to a warmer surface, as a consequence, the low-level convergence over the urban surface contributes to the formation or location of clouds (Angevine et al., 2003). Also, the urban climate increases the source of cloud condensation nuclei (Jin et al., 2005; Diem and Brown, 2003). Crops have a lower stomatal resistance,which increases evaporation and decreases cloud-base, eventually generating more clouds than forest (Betts et al., 2007).

The LST detected in this study shows some extremely low values in summer, which may be caused by clouds. We set thresholds for the daily dataset, but the influence will be integrated in the composite LST product online and decrease the LST value of that pixel over the 8-day period, which should be considered in applications. Also, cloudy urban environment effectively restrict the development of pronounced SUHI (Morris et al., 2001). However, remote sensing only works well under clear sky conditions. As a result, biases from the technique itself may increase the SUHI magnitude for long time monitoring.

We illustrated the mean effects of Terra and Aqua. However, variation between Terra and Aqua exists (Schwarz et al., 2011), not only the LST but also the clear sky coverage distribution and ratio. The overpass times of Terra and Aqua are before and after the highest temperatures in a day. The statistics shows that the afternoon LST is about 2.6 K higher than the late morning, and before midnight LST is about 1.0 K higher than 2:30 am LST. The mean Terra and Aqua LST cannot represent the highest and lowest temperatures of the day and night, which may not correspond to the largest SUHI. However, the R_{csc} values of Terra and Aqua are statistically equal (t-test, $p < 0.05$). Due to the fact that the aggregation processing and analysis were conducted for Terra and Aqua separately, these results indicate the mean effect of temporal aggregation.

2.6 Conclusions

In order to investigate a long term urban heat island dynamics with maximum decreased influences of clouds, this paper discussed the impact of using the 2-, 4-, 8-, 16- and 32-day composite LST instead of daily LST in Houston area to study SUHI. Especially, due to the availability and high clear sky coverage of 8-day composite LST, MODIS daily LST and 8-day composite LST products have been statistically compared for SUHI in both spatial and temporal respects.

Three main conclusions can be made from the results of this study. First, the temporal aggregation impact has seasonality and is also a function of composite scale. The seasonal pattern shows that the summer daytime SUHI has the largest magnitude and variation, while the nighttime SUHI magnitudes are much smaller and less variable. The composite scale is particularly important during the summer daytime. The higher the aggregation scale is, the higher SUHI biases are generated. However, the impact from the two factors for nighttime is comparably small. Consequently, we recommend using shorter composite period in summer daytime. Second, the temporal aggregation varies spatially, which is related to the land cover types. The mean bias caused by land cover types were calculated to be about $1.6 \sim 2.0K$ during the daytime, and less than 0.4 K at night. Third, the potential cause of the errors from temporal aggregation is heterogeneously distributed clouds. The analysis shows that the land–atmosphere interactions, which result in higher frequency of clouds over the urban areas, are the primary reason.

However, additional research is required to draw a more common conclusion. As discussed above, it is preferable to know that the impact on temporal aggregation is independent from SUHI indicators. Also, it is worthwhile to test the aggregation impact on the cities in various climate regions. For example, although the impact is outstanding for summer daytime, cities in the dry regions may be less influenced by clouds. The seasonality and bias magnitude may vary. Also, the size and structure of city are also factors that impact SUHI, which may have more or less UHI effects due to the aggregation bias. In addition, other sensors have variable observation time, spatial and temporal resolution, which need be tested too.

An important message emerging from this study is that the aggressions of 8-day period of daily

MODIS LST products will increase the spatial coverage of information; however, it will lose some accuracy, the extent of which differs diurnally and seasonally, particularly for the summer daytime. For long term or global SUHI studies, it is beneficial to use 8-day composite LST if we can balance the gains and losses.

Chapter 3

How can we use MODIS land surface temperature to validate long-term urban model simulations?

3.1 Introduction

Approximately half of the world's population now lives in the metropolitan areas, and urban expansion is expected to continue (World Health Organization Centre for Health Development, 2010). The combined impacts of global climate change, urban heat islands (UHI), urbanization, and demographic trends place more urban residents at risk to heat-related stressors. More accurate information on urban meteorology, high-resolution weather forecasting, and climate change projections for cities are therefore required (National Research Council, 2012).

Atmospheric models are helpful for understanding the current climate system and projecting future climate changes. Regional and local scale atmospheric model simulations are especially valuable for decision making at the municipal level, however they necessitate accurate representations of specific urban features (e.g. morphology), fine-scale climatic background information, and ideally are coupled to urban canopy models (UCMs). UCMs have advanced rapidly during recent

decades (Grimmond et al., 2010) and have been coupled to a variety of atmospheric models (Chen et al., 2011; Oleson et al., 2008; Kusaka and Kimura, 2004) for use in numerous applications. For example, Chen et al. (2011) integrated the Weather Research and Forecasting model (WRF) (Skamarock and Klemp, 2008) coupled with the UCM of Kusaka et al. (2001) at 1 km spatial resolution to assess the impacts of urbanization on Houston's sea breeze circulation and found that the city enhances stagnant air at nighttime, which can exacerbate pollution. Despite the utility of high-resolution urban climate modeling, the heterogeneous surface structures in the urban environment, with multiple sources of energy and water, increase the complexity of models, and consequently can increase the uncertainty of model accuracy.

Climate simulations over urban regions are usually validated with in-situ measurements (Grimmond and Oke, 2002; Masson, 2006). Large collaborative programs that integrate different types of measurements at multiple temporal and spatial scales are becoming popular in urban climate studies (Mestayer et al., 2005; Grimmond, 2006). Nevertheless, the expense, location, and duration of in-situ measurement programs limit their widespread application for long-term model simulations and validation. Moreover, the heterogeneity of the urban environment cannot be fully represented by the limited footprint of in-situ measurements, which complicates attempts to analyze the spatial agreement of observations with model output.

Accurate estimation of radiative temperature is required for any coupled climate modeling system, because it is an integral component of the surface energy budget, water stress evaluation, and soil moisture-climate feedback (Bodas-Salcedo et al., 2008; Ghent et al., 2010). Land surface temperature (LST) products from satellite remote sensing platforms are widely available and are potential sources for model validation, having comprehensive spatial coverage, comparable scale with models, and constant periodicity. There are many ways to apply satellite LST data to evaluate and improve atmospheric model simulations at multiple temporal and spatial scales (Jin et al., 1997; Sohrabinia et al., 2012; Miao et al., 2009; Leroyer et al., 2011). For example, Jin et al. (1997) compared skin temperatures simulated with NCAR Community Climate Model (CCM2) coupled with a biosphere-atmosphere transfer scheme with satellite-derived radiative temperature

to evaluate model performance globally. LST can also be incorporated into data assimilation, helping to constrain uncertainty in model simulations. For instance, Ghent et al. (2010) found that the LST bias of the Joint UK Land Environment Simulator (JULES) was reduced by two-thirds by applying observed LST by means of data assimilation. The limits of satellite remotely sensed LST for improving model performance in the long term are unknown, especially in complex urban environments.

There are several aspects to consider before comparing LST with urban climate model simulations. First, the distribution of clouds across the urban area is heterogeneous and varies seasonally (Hu and Brunsell, 2013). The cloud-screening algorithms for satellite images usually are not perfect for detecting all cloudy pixels, so cloud-contaminated pixels exist in some ``cloud-free'' products. The data that are unavailable due to clouds would otherwise contain important information for model validation, and the impact of clouds is often larger during daytime than nighttime (Hu and Brunsell, 2013). Second, the satellite LST is a directional radiative temperature, representing the information from a certain view angle (Voogt and Oke, 2003). The anisotropy of LST largely exists due to differences in surface properties, the urban geometric structure, and the relative geometry between the sun and sensor. Additionally, the view angle relates to the atmospheric path length corresponding to absorption and reemission of radiation, leading to larger anisotropic effects for large view angles in the remotely sensed LST. Although view angle effects from the atmosphere are considered in LST retrieval algorithms (e.g., Wan and Dozier (1996)), the surface structure induced anisotropy of LST still exists (Voogt and Oke, 1998; Rasmussen et al., 2010; Vinnikov et al., 2012; Lagouarde et al., 2004). Third, different sensors have different temporal and spatial resolutions, as well as data acquisition times. Adequately addressing these issues can allow for satellite LST data to be comparable with model simulations of surface radiative temperature. However, little research on this topic has been done previously.

This paper addresses the question of how to use satellite remote sensing LST to validate surface radiative temperature in an urban canopy model. We propose three practical methods, attempting to decrease the uncertainty of the satellite LST product and to meet a variety of different demands

of validations depending on the application. The methods are tested using daily LST from the Moderate Resolution Imaging Spectroradiometer (MODIS) for the decade spanning 2003 to 2012, compared with simulations of surface radiative temperature from the High-Resolution Land Data Assimilation System (HRLDAS) (Chen et al., 2007) over Greater Houston, Texas, USA. The details of MODIS and the HRLDAS simulations are described in Section 3.2, and the three sampling methods are discussed in Section 3.3. The temperature distributions and spatial analysis of the MODIS data and simulations for each method are presented in Section 3.4, as well as the justification of the assumptions made in the sampling methods. The advantages and disadvantages of the three sampling methods and their scope of applications are discussed in Section 3.5, and conclusions are drawn in Section 3.6.

3.2 HRLDAS and MODIS Data

3.2.1 Study Area

We choose Houston, Texas as the study area, defining the domain from 29.25 N and 96 W (southwest) to 30.5 N and 94.75 W (northeast). Fig. 3.1 shows the HRLDAS model domain and land use categories based on the U.S. Geological Survey (USGS) National Land Cover Database (Homer et al., 2004; Fry et al., 2011). Three urban types are classified in the domain, including light-intensity urban (LU), heavy-intensity urban (HU), and commercial urban (CU, including industrial area), covering approximately 20.6%, 5.0%, and 1.9% of total land area, respectively. Other majority land cover types include cropland and grassland mosaic (27.9%), wooded wetland (23%), and dryland cropland and pasture (8.9%).

3.2.2 HRLDAS simulations

Here we briefly describe the methodology for simulating radiative temperature, T_{rad}, with HRLDAS. For additional details, the reader is referred to a full description of the modeling approach in

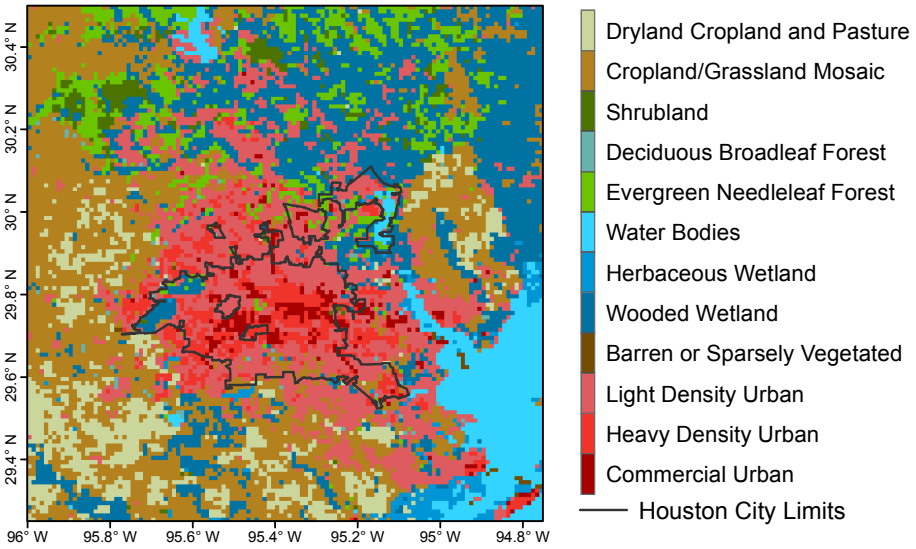

Figure 3.1: The land use map used in the HRLDAS model simulation.

Monaghan et al. (2014). HRLDAS is an offline (i.e., uncoupled to an atmospheric model) version of the Noah Land Surface Model (Noah LSM) (Chen and Dudhia, 2001; Chen et al., 2007). The Noah LSM simulates the fluxes of energy and water from the land surface as a function of the underlying land surface and soil properties, while also maintaining stores of water and energy in four soil layers to a depth of 2 m. In order to better represent the physical processes involved in the exchange of heat, momentum, and water vapor in the urban environment, the UCM of Kusaka et al. (2001) is employed within the Noah LSM. The UCM provides a more realistic description of the urban lower boundary conditions and morphology and therefore more accurate simulations for urban regions. As mentioned above, the urban land use categories (low-intensity, heavy-intensity and commercial) for Houston were characterized in the UCM with the 30 meter resolution 2001 USGS NLCD (Homer et al., 2004). The urban-versus-vegetated (i.e., non-urban) percentage within each grid cell was specified by the National Urban Database and Access Portal Tool (NUDAPT) (Ching et al., 2009; Burian and Ching, 2009), a 2-dimensional dataset of influential urban properties. The use of NUDAPT leads to a more heterogeneous UHI characterization in the HRLDAS simulations.

Half-hourly, 1-km resolution HRLDAS simulations were performed over metropolitan Houston for 2003-2012, preceded by a 1-year (2002) ``spin up´´ period to allow the soil temperature and

moisture states to equilibrate (Chen et al., 2007). The upper boundary conditions for HRLDAS were derived from $1/8^{th}$ degree hourly meteorological data from the North American Land Data Assimilation Phase 2 (NLDAS-2) (Cosgrove et al., 2003; Xia et al., 2012) forcing dataset. It was assumed that watering and irrigation was applied to all vegetated surfaces, a process represented in HRLDAS by setting in the upper soil layer a lower threshold of 30% water by volume.

In order to ensure that the temperature fields being compared were as similar as possible, we generated a diagnostic radiative temperature (T_{rad}) variable in HRLDAS such that it is similar to the MODIS LST product. At each time step, the energy balances for the roof, wall, and road components for each grid cell containing urban areas were simulated by the UCM subroutine within the Noah LSM. The simulated outward longwave radiation values for the roof, wall and road were then combined into a bulk urban longwave radiation value for each grid cell, based on the weighted average of the roof and canyon (wall + road) longwave components. A bulk urban emissivity value was calculated in the same manner for each grid cell. Concurrently the longwave radiation was calculated in the LSM for the vegetated portion of each grid cell. Then, the bulk urban and vegetated longwave radiation and emissivity values were averaged by weighting the fraction of urban-versus-vegetated area in each grid cell. Finally, these resulting ``integrated´´ longwave radiation and emissivity values for each grid cell were used to calculate T_{rad} using the Stefan-Boltzmann law. The T_{rad} is most representative of nadir for all cases if we do not include wall proportion.

3.2.3 MODIS Data

The MODIS sensors onboard the Terra and Aqua satellites provide global-coverage of LST four times per day. The satellite sun-synchronous orbits of MODIS are designed to cross the equator at 10:30 and 22:30 for Terra, and at 13:30 and 1:30 for Aqua (local solar time). The high frequency of global coverage is at the expense of a large range of view angles spanning from -65° to +65° from nadir. The retrieved spatial resolution for LST is as high as 1 km, which coincides with the scale of the HRLDAS output. The 1 km resolution LST data is produced using the split-

window method described by Wan and Dozier (1996), and filtered with the MODIS Cloud Mask products (MOD35 L2). The LST MOD11A1 (Terra) and MYD11A1 (Aqua) Version 5 (Wan, 2008) products from 2003-2012 summers (June-July-August, JJA) across the Houston area were collected and processed for this study.

3.3 Sampling Strategies

To ensure that the samples from MODIS and HRLDAS are comparable, we attempt to minimize the biases caused by factors other than the model. Three major aspects must be considered and properly addressed before the MODIS-based model evaluation: satellite overpass time, sensor view angle, and cloud distributions and cloud contaminated pixels. Among them, the cloud distributions are the primary issue affecting sampling strategies, and we describe the different sampling methods to account for this issue in this section.

3.3.1 Satellite Overpass Time

The overpass times provided by MODIS LST product are in local solar time, which is defined as the MODIS observation time in coordinated universal time (UTC) plus longitude in degrees divided by 15 (Williamson et al., 2013). MODIS overpass times are converted from local solar time to local standard time or UTC to enable comparison with model simulations. Each overpass time for the Houston area is slightly different, but is usually within 2 h. For example, the daytime overpass data is distributed between 10:00 to 12:10 for Terra and between 12:30 to 14:30 for Aqua over the 10-year summer record. The median local standard times of satellite overpasses for the datasets are about 11:16 (Terra-day), 13:34 (Aqua-day), 22:34 (Terra-night), and 02:16 (Aqua-night). We selected the HRLDAS outputs at 11:30, 13:30, 22:30, and 2:30 as the four daily times, therefore we could conduct the comparison at the nearest half hours to the median MODIS overpass times.

3.3.2 View Angle

Thermal angular anisotropy is a widely observed phenomenon and has been reported in soil, grass, savanna (Pinheiro et al., 2006), forest canopy (Smith et al., 1997), and urban area by modeling (Soux et al., 2004), surface observations (Zhan et al., 2012), and airborne thermal sensors (Voogt and Oke, 1998) with temperature biases of several degrees or even larger. The accuracy of LST related to view angle depends largely on the correction of atmospheric effects, which is a function of wavelength, local meteorological conditions, time of day, season, and location. Although the MODIS LST products are corrected for atmospheric effects related to view angles, the anisotropy bias effect can still be detected due to the generalized parameters used for the atmosphere correction algorithm, as well as the heterogeneous surface structures of various surface components.

Generally, there are two primary solutions to minimize the impact of different view angles between the observations and model output: correct the MODIS LST view angles to nadir, or adjust the HRLDAS T_{rad} to the same view angle of MODIS. The use of the split window atmospheric correction does not adequately remove the effect of view angle from the MODIS data. We can potentially incorporate additional local observations to conduct a more accurate atmosphere correction. However, most correction processes are complex and require knowledge of the atmospheric conditions (e.g. an atmospheric sounding) near the time of satellite overpass. This ancillary information is sometimes unavailable for a specific location and a certain period of time (Vinnikov et al., 2012). On the other hand, Lagouarde et al. (2004, 2012) demonstrated with airborne measurements that angular impacts on land surface temperature exist over urban areas. Corrections for this effect require knowledge of the angular anisotropy of urban surfaces, which is even more complex than that of atmospheric attenuation. The magnitude of biases induced by view angle effects related to the urban surface structures is unclear at the 1 km scale.

There is also the option to adjust the view angle for simulated T_{rad} based on the morphology of simulated urban canyon structure due to the availability of each urban component temperature (T_{roof}, T_{wall}, T_{road}) and corresponding emissivity for each grid cell within the model. However, the difficulty of simulating directional vegetation temperatures prohibits the estimation of the biases in

mixed urban-rural and rural-only pixels, especially for a heavily vegetated city, like Houston (there are no pure urban pixels). Therefore, we applied the view-angle correction to the temperature of only the urban fraction in each grid cell, and tested the results only for the daytime. The mean adjusted daytime T_{rad} is about 1 K lower than the unadjusted T_{rad} (which is equivalent to the temperature at the nadir); however, the distributions of adjusted T_{rad} at different view angles are similar.

Fig. 3.2 illustrates the impact of view angle on MODIS LST. View angle thresholds of 15°, 35°, and 55° were applied, and LST distributions with larger and smaller view angles than the threshold were analyzed. Generally, the LSTs with smaller view angles tend to be warmer. The distributions differ with land cover type and time of day for LSTs with larger and smaller view angles. For example, the daytime mean LST differences between pixels with smaller and larger view angles about 2.4 K, 2.8 K and 3.4 K for the view angle thresholds of 15°, 35°, and 55° over the commercial urban area. The nighttime mean LST differences for the three view angle thresholds are 1.3 K, 1.3 K, and 1.7 K for Terra and about 0.5 K smaller for Aqua. Moreover, we tested the view angle effect on water bodies. It showed the existence of anisotropy, indicating a large impact from the atmospheric interaction rather than the surface morphology. Consequently, correcting the view angle of either MODIS LST or adjusting HRLDAS T_{rad} does not seem practical. In order to minimize the biases caused by the view angle, we have chosen to only compare HRLDAS T_{rad} at nadir with MODIS LST that has a small view angle.

However, we should be aware that there are some potential biases comparing the temperature at nadir and off-nadir. As we mentioned before, the atmospheric attenuation is the major view-angle-dependent bias for MODIS LST. The LST at off-nadir angles generally will have a lower bias compared with temperature at nadir due to the longer atmospheric path. From the urban surface morphology perspective, the LST at off-nadir may further decrease during the daytime due to viewing less road proportion and more wall proportion in the urban canyon where usually $T_{road} > T_{wall} > T_{roof}$. There is a higher T_{wall} than T_{road} and T_{roof} at night, so LST bias can be offset at a certain level (please find further details about the urban component temperature in Monaghan et al.

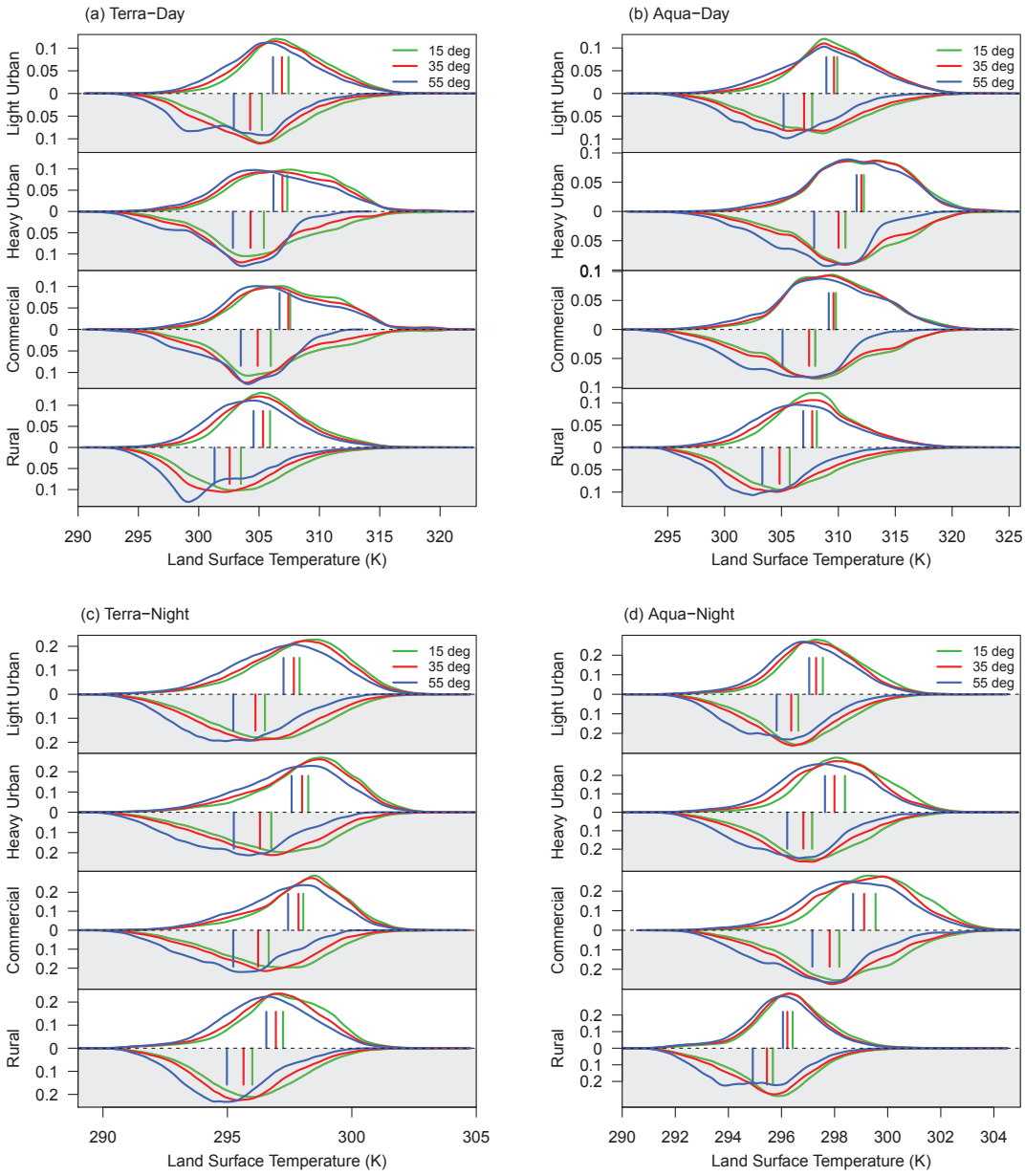

Figure 3.2: The LST probability density distributions for view angle thresholds of 15° (green), 35° (orange), 55° (blue), respectively. The upper half of the distribution plots are the pixels with view angles smaller than the given threshold, and the lower shaded half indicates the LST distributions with larger view angles. The short segment line indicates the mean temperature of each distribution.

(2014). By excluding LST with large view angles, the bias of the sampled LST at off-nadir angles can be effectively controlled.

In order to maintain a sufficient sample size, we cannot set the view angle threshold too small. Fig. 3.3 shows the ratio of sampled pixels to the total available pixels (excluding outliers). The ratio of sampled-versus-total pixels for a given threshold exhibits a nearly linear relationship, indicating a relatively uniform distribution of view angles. At a view angle threshold of 35°, more than 40% of pixels are selected for analysis. The total number of available pixels is dependent on the overpass time due to the variable cloud coverage throughout the diurnal cycle. The Terra daytime data usually has the fewest clear-sky pixels over the urban area during summer. With consideration of sample size and view angle impacts on LST, we decide to use 35° as the view angle threshold in this study.

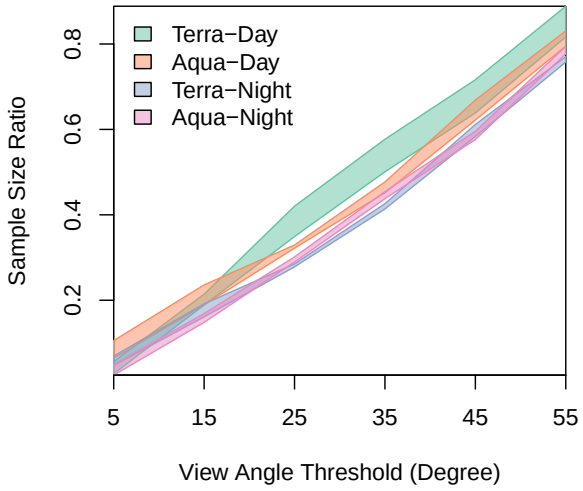

Figure 3.3: The ratio of sampled pixels with a view angle smaller than the threshold to the total number of available pixels for the four times of day corresponding to MODIS over pass times (with four different colors). The shaded region indicates the range of ratios for the three urban land use types and the rural classification.

3.3.3 Cloud Distributions and Cloud Contaminated Pixels

Cloud contaminated pixels – i.e., pixels with cloud influences that are not removed during quality control – are also an issue found in the LST product (Williamson et al., 2013). In general, the cloud edges and thin clouds are the major sources of contamination (Platnick et al., 2003). Thick aerosol content from pollutants over the urban area also contributes to pixel contamination, which may partially explain why fewer daytime pixels meet the clear-sky criteria over urban areas compared to adjacent rural areas. It is unclear how advection of pollution plumes affects outlying suburban and rural areas. When the pixels contaminated by clouds or high aerosol content during the daytime remain in the analysis, the MODIS temperature is biased low relative to the ¨true´´ temperature. Most cloud contaminated pixels have been removed in the Version 5 LST product (Wan, 2008). However, some extremely low temperatures were found in the LST product during summer daytime, presumably due to cloud contamination.

Cloud contaminated pixels (those that remained in the Version 5 LST product) were removed first from MODIS LST, by retaining only the data within 1.5 times the interquartile range (Q3-Q1) at each pixel point and time of day. Using a time series to identify the outliers is better, because the detection through spatial analysis may bias the temperature variations caused by land cover type, and may also fail to detect all the contaminated pixels due to the existence of many contaminated pixels in one scene. Table 3.1 shows the statistics related to the outliers. After masking the outliers, the lower end temperature during 10 years increases from 248.3 K and 238.6 K to 290.8 K and 291.5K for Terra and Aqua daytime images respectively, and from 276.2 K and 273.8 K to 289.3 K and 289.9 K threshold for Terra and Aqua night, respectively. The maximum temperature deceases by about 5 K for daytime, and 11 K for Terra night, 2 K for Aqua night after filtering the outliers. This process may potentially exclude extreme heat days. However, it is only a small portion (about 1.2% of the total original pixels). Moreover, the extreme days were excluded from MODIS, as well as the corresponding data in HRLDAS, so it would not impact the sampling methods or the comparison for the long term.

Clouds frequently form on summer afternoons in Houston (Burian and Shepherd, 2005), coin-

Table 3.1: The statistics of the outliers for four times of day corresponding to MODIS overpass times, including the mean and standard deviation (STD) of hot and cold outliers, and the ratio of outliers to the total number of original data.

	Terra Day		Aqua Day		Terra Night		Aqua Night	
	Hot	Cold	Hot	Cold	Hot	Cold	Hot	Cold
Mean (K)	316.2	293.7	318.3	294.5	302.6	289.9	299.8	290.2
STD (K)	3.0	3.6	3.7	5.6	2.6	1.5	0.7	1.8
Ratio	1.16%	0.75%	1.22%	0.92%	0.04%	1.46%	0.12%	3.58%

ciding with MODIS daytime overpasses. Fig. 3.4 shows the distribution of the ratio of clear days to the total days (there are 920 total days) during 10-year JJA. The cloud distribution is most heterogeneous during the summer daytime compared with other seasons, or with nighttime (Hu and Brunsell, 2013). The deep convection due to the thermal properties of urban surface, urban-rural advection, thick aerosols, etc. all contribute to the large cloudiness differences between urban and rural areas.

After masking the outliers and pixels with larger view angles, the LST data from 2003 to 2012 from four times a day were used as the primary samples from MODIS. Clouds are not explicitly resolved in the HRLDAS forcing data. Instead, clouds are manifested through fluctuations in the surface downwelling longwave and shortwave radiative forcing fields, which makes it difficult to define exactly when cloudy conditions are present in the simulations over a given grid point. We therefore tested the three methodologies described below as a means of minimizing differences between MODIS and HRLDAS due to clouds.

3.3.4 Sampling methods for MODIS-HRLDAS Comparisons

In the first sampling method – satellite cloud mask (SCM) method, we assume that the cloud distributions in MODIS and HRLDAS are the same. Therefore, we can apply the masks built from MODIS for the clouds, outliers, and view angles to HRLDAS. As a result, the total sampled pixels for 2003-2012 is 16.8%, 11.6%, 24.2% and 20.7% of the total pixels in the domain (except the inland water and sea) for the Terra day, Aqua day, Terra night, and Aqua night passes, respectively.

The second method, max/min temperature (MMT) method, is to independently select the

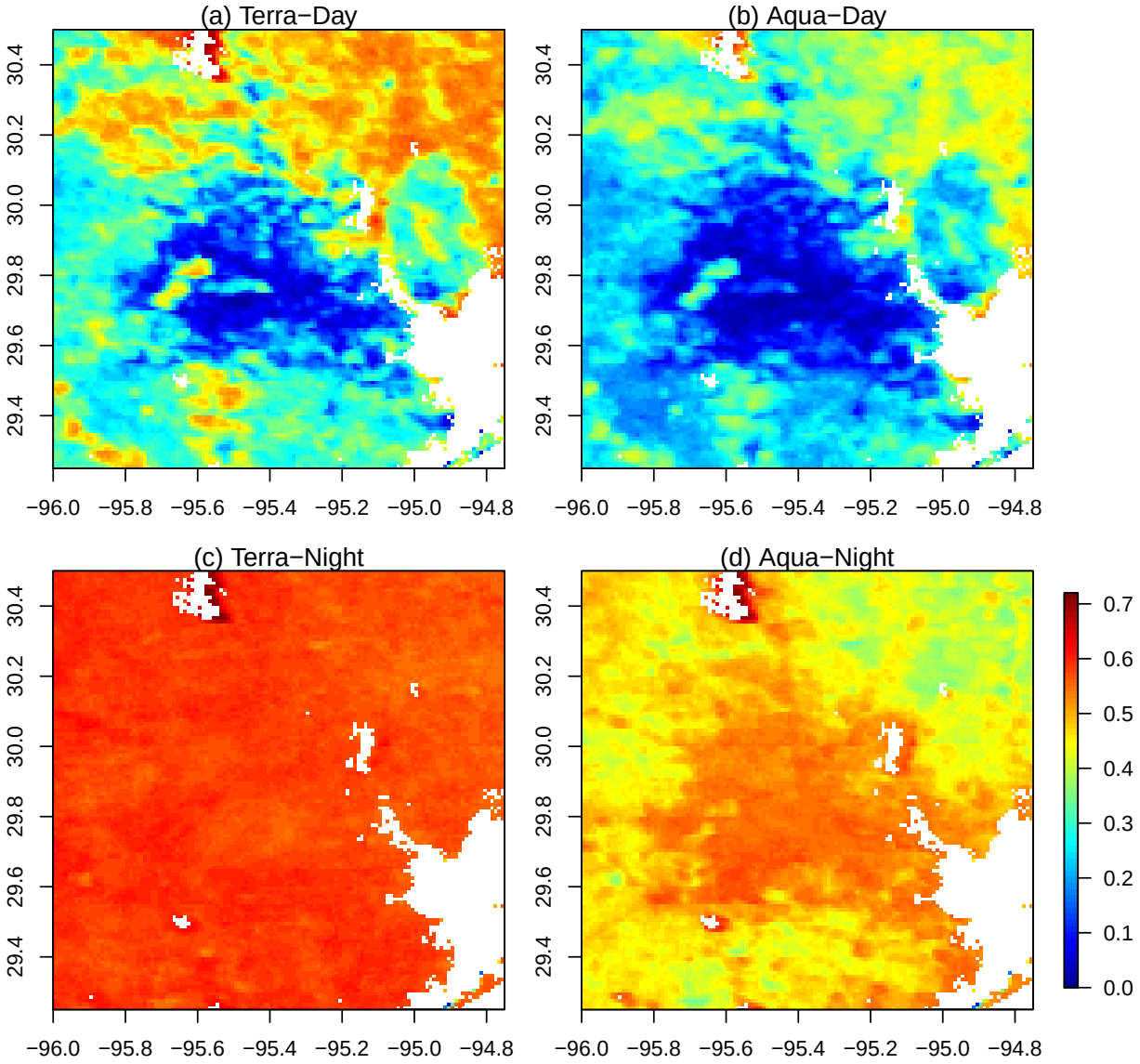

Figure 3.4: The ratio of selected pixels to total days available for four times of day during 2003-2012 JJA. In-land water and sea pixels are masked, which are the white region in the figure.

warmest days and coolest nights in the model output and MODIS observations. This method relies on the fact that clear-sky LSTs are generally higher (lower) than cloudy or cloud-contaminated pixels during the daytime (nighttime) because of the tendency of clouds to dampen daytime high and nighttime low temperatures (Dai et al., 1999). First, we applied the common masks from MODIS (outliers and view angles) to both MODIS and HRLDAS data. It is difficult to determine whether clouds are concurrently impacting both MODIS and HRLDAS fields at every grid point, and therefore we sampled the warmest days and coolest nights separately for each dataset, in order to minimize the possibility of clouds impacting either dataset. Assuming that neither MODIS nor the HRLDAS simulations perfectly characterize clouds in space and time, this approach necessitates that the comparisons will not be temporally consistent.

There are many missing data in the MODIS fields, especially during daytime when convective clouds are common (see Fig. 3.4). One of our objectives is to map spatial patterns of the heat island, which ideally requires a consistent number of days available for each grid point. Despite the large amount of missing data, we found that for most grid points, there are at least 50 days with available (``clear-sky´´) data for a given daytime pass during 2003-2012 summers. We therefore sampled the warmest 50 days and the coolest 50 nights from the HRLDAS and MODIS data for each overpass time, respectively, representing about 5.4% of each set of data. The percentage of available data was slightly lower than 5.4% for daytime due to some grid cells having less than 50 cloud-free days. There are 2993, 733, and 278 grid cells with LU, HU, and CU, respectively, and therefore despite using only a small fraction of the overall total days for the comparison, there remains an adequate sample size for each land use category to draw statistically meaningful conclusions.

In the third method – high clear-sky fraction (HCF) method, we only choose the daytime and nighttime MODIS overpasses with a high percentage of clear-sky coverage in a scene after excluding the outliers and pixels with larger view angles. The same times are selected from the HRLDAS simulations. Approximately 25% of the total pixels in the domain is urban land cover type in this study. We suggest the clear-sky coverage ratio be set to 90% or more, so that we can guarantee at

least more than half of urban pixels are available (clear-sky) in the each sampled overpass. This method helps eliminate problems caused by cloud mismatches, and also maintains the temporal and spatial consistency between observations and simulations. However, based on our selection criteria there are limited number of days available, due to the prevalence of clouds. About 28 and 8 cloud-free days, and 132 and 97 cloud-free nights are sampled from Terra-day, Aqua-day, Terra-night and Aqua-night, respectively for MODIS during the study period.

3.4 Results

3.4.1 Distribution Analyses

The probability density distributions for the three proposed sampling methods were compared between MODIS observations and HRLDAS simulations at each time of day and each land cover type (Fig. 3.5). If the conditions are mostly clear-sky, the MODIS and HRLDAS samples selected by the SCM and HCF methods should be similar spatially and temporally, which is the most ideal case for comparison. For example, the LST distributions of the SCM and HCF methods are analogous during the nighttime in most land cover types. However, the high frequency of clouds during the daytime in Houston, especially over the urban area, dramatically decreases the sample size under the HCF method. The daytime distribution is narrower in the HCF method compared to the SCM method due to fewer sampled days. The distributions are less coincident in HU and CU, which is probably due to the smaller sample size compared with rural and LU. The MMT method is somewhat different in that it scrutinizes the ability of HRLDAS to simulate the two extreme ends of the temperature distribution, and therefore the distributions are less smooth with much smaller LST ranges.

T_{rad} in daytime HRLDAS simulations are overestimated in most cases (Fig. 3.5). An exception is the relatively good match between the HRLDAS and MODIS distributions for rural and CU areas in the HCF method for Aqua daytime overpasses, despite small sample sizes. In general, the nighttime comparisons are in better agreement. For example, the Terra nighttime comparison in the

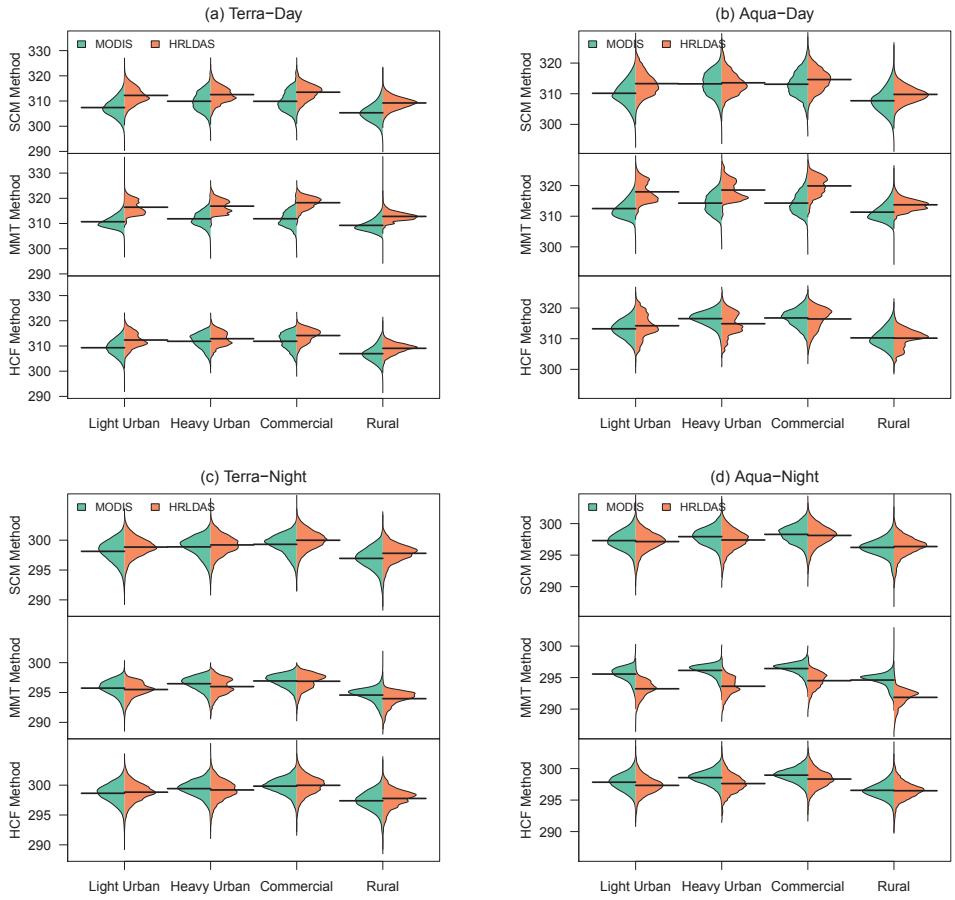

Figure 3.5: The probability density distribution of MODIS LST (K) and HRLDAS T_{rad} (K) for the different sampling methods. The black horizontal line indicates the mean temperature. The satellite cloud mask (SCM) method uses all pixels after quality control; the max/min temperature (MMT) method uses the 50 warmest days/coolest nights for each grid; and the high clear-sky fraction (HCF) method uses all days/nights with a spatial clear-sky coverage ratio over 90%.

MMT method indicates good agreement with differences less than 0.6 K. The largest differences result from using the MMT method which necessarily compares the coolest nights in both datasets; HRLDAS is about 1.9 K $\sim$ 2.7 K cooler for different land cover types. HRLDAS simulates a fast decrease in temperature from 10:30 pm (Terra night) to 2:30 am (Aqua night), which is not observed in the MODIS data, suggesting HRLDAS underestimates the urban heat island. HRLDAS is an offline model and therefore it is not coupled with the atmosphere, which can be a source of bias. For example, it is possible that a coupled model would mitigate large temperature gradients between the urban area and atmosphere. Also, the forcing data may have some urban signature but likely not at the scale we are using the model. Overall, the temperature patterns among different land cover types are generally comparable. Rural areas are cooler than urban areas, and the ``most rural´´ urban type, LU, is cooler than other urban types for all times and sampling methods in both datasets.

3.4.2 Spatial Analyses

All the sampled LST and T_{rad} through time were averaged at each pixel, and the resultant spatial distributions of the averaged LST and T_{rad} maps from the three sampling methods are shown in Fig. 3.6 (Terra only), indicating different spatial patterns due to the different sampling strategies. The spatial patterns among the sampling methods are more similar during nighttime than daytime. The HCF method matches well with the SCM method spatially, with correlations between HRLDAS and MODIS of 0.98 and 0.99 for daytime and nighttime, respectively. The MODIS LST distribution in the MMT method has correlations of 0.90 and 0.88 with SCM and HCF methods within the urban area, and slightly higher correlations in rural areas for most of the time during day and night. The nighttime urban boundary is better defined among methods; however, the UHI is still observed in the mean of warmest 50 pixels during the daytime. The difference maps between MODIS and HRLDAS show a similar pattern among methods for daytime and nighttime. The heterogeneous distribution of bias is related to the land cover type. For example, the wetland temperature was overestimated at the north-east corner of the domain by about 5 K according to

the SCM and MMT methods, and 3.9 K for the HCF method, while the urban areas were overestimated by about 3.6 K, 5.6 K and 2.5 K for three methods for Terra daytime data. The range of differences during the daytime is similar among the three methods, about 20 K, while the range during the nighttime is smaller, about 8 K. The overall domain-average temperature differences are about 4 K and 3 K for Terra and Aqua daytime for the MMT method, which is about 1 K $\sim$ 2 K larger than other two methods, suggesting HRLDAS has comparatively lower skill at simulating extremes. We will discuss potential reasons in the next section.

3.4.3 Justification of Sampling Method Assumptions

For the SCM method, we assumed the cloud distribution in HRLDAS is coincident with MODIS observations, so that we could apply the MODIS cloud mask to HRLDAS. Fig. 3.7 shows the probability density distributions for HRLDAS T_{rad} for clear-sky and cloudy pixels defined by the mask in the MODIS LST product in the SCM method. HRLDAS mean T_{rad} is about 0.4 K (about 1 K for LU and rural areas) warmer in the cloud-free pixels over the cloudy pixels during daytime, which is expected because clear-days are warmer than cloudy days. The nighttime differences are smaller, probably due to the lack of interaction of strong external energy sources (e.g. solar radiation) and also the accuracy of cloud maps. Generally speaking, cloud detection is more difficult during the nighttime (Platnick et al., 2003) due to less information in the optical regions of the spectrum. In summary, the assumption we made for the SCM method – that cloud distributions are similar between HRLDAS and MODIS – appears to be true for daytime and inconclusive for nighttime.

The assumption we made for the MMT method was that the warmest (daytime)/coolest (nighttime) pixels from MODIS and HRLDAS should be temporally consistent at a certain level. In other words, if the cloud masks of two data sources are comparable, and the model is able to simulate the temperature variability similar to the MODIS LST observations, the distributions of sampled pixels that are cloud-free should share many of the same hot days and cool nights in common. The ratio of the number of temporally consistent days to the total sampled days for each grid is shown

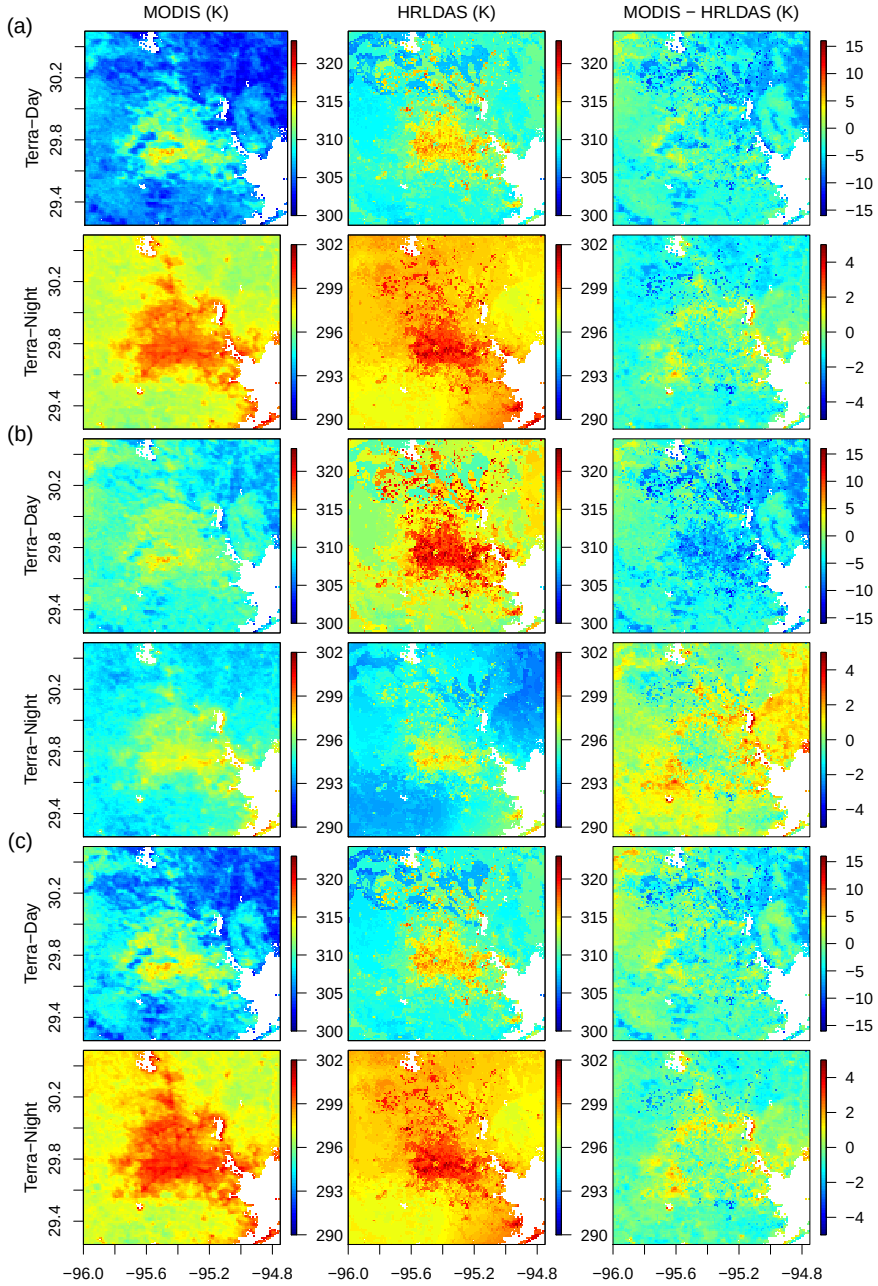

Figure 3.6: The temporally averaged LST determined from the three sampling methods and the difference map between MODIS and HRLDAS. (a), (b), and (c) demonstrate sampling methods: satellite cloud mask (SCM) method, max/min temperature (MMT) method and high clear-sky fraction (HCF) method, respectively.

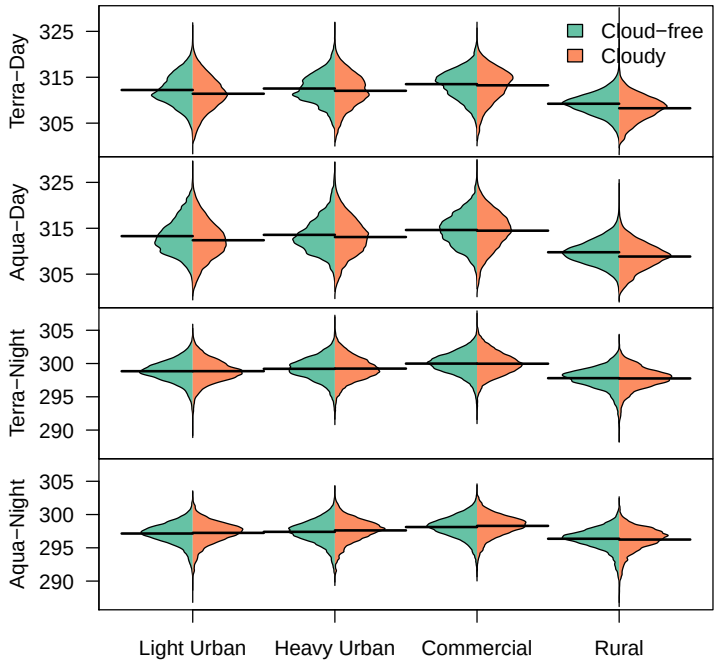

Figure 3.7: The comparison between the ``cloud-free'' and ``cloudy'' pixels of HRLDAS T_{rad} (K) by using the cloud mask from MODIS in the SCM method at four times of day and four land cover types.

in Fig. 3.8. The temporal agreement in the urban area is very low (a ratio of about 0.1 (Terra) and 0.09 (Aqua)) compared with northeast-corner rural areas (wetland and forest land cover types with ratios of about 0.23 (Terra) and 0.18 (Aqua)) during the daytime. The spatial distribution of the ratios is less variable during the night with an average of 0.20 and 0.17 in urban areas for Terra and Aqua, respectively. The spatial patterns in Fig. 3.8 are closely related to the spatial distribution of the available-to-total pixels after excluding the outliers and the pixels with large view angles (not shown here, it is similar to Fig. 3.4.), especially during the daytime with correlation coefficients of 0.8 (Terra), and 0.7 (Aqua). The correlation drops to 0.2 for Terra night when the cloud-free ratio is high and with less spatial variability. Consequently, the cloud distributions and frequency may directly impact this method, i.e., it is so cloudy during most days that insufficient samples are available over the urban areas. For example, there are less than 20 clear-sky days in some urban pixels during the 2003-2012 JJA periods. On the other hand, the poor temporal agreement may also be attributed to model defects, such as the mismatch of clouds due to the forcing data, or sim-

plified assumptions (we evaluate model performance in the companion paper by Monaghan et al. (2014). In summary, the MMT method may be better suited for regions where daytime cloudiness is not as persistent so that a larger distribution of pixels can be drawn from.

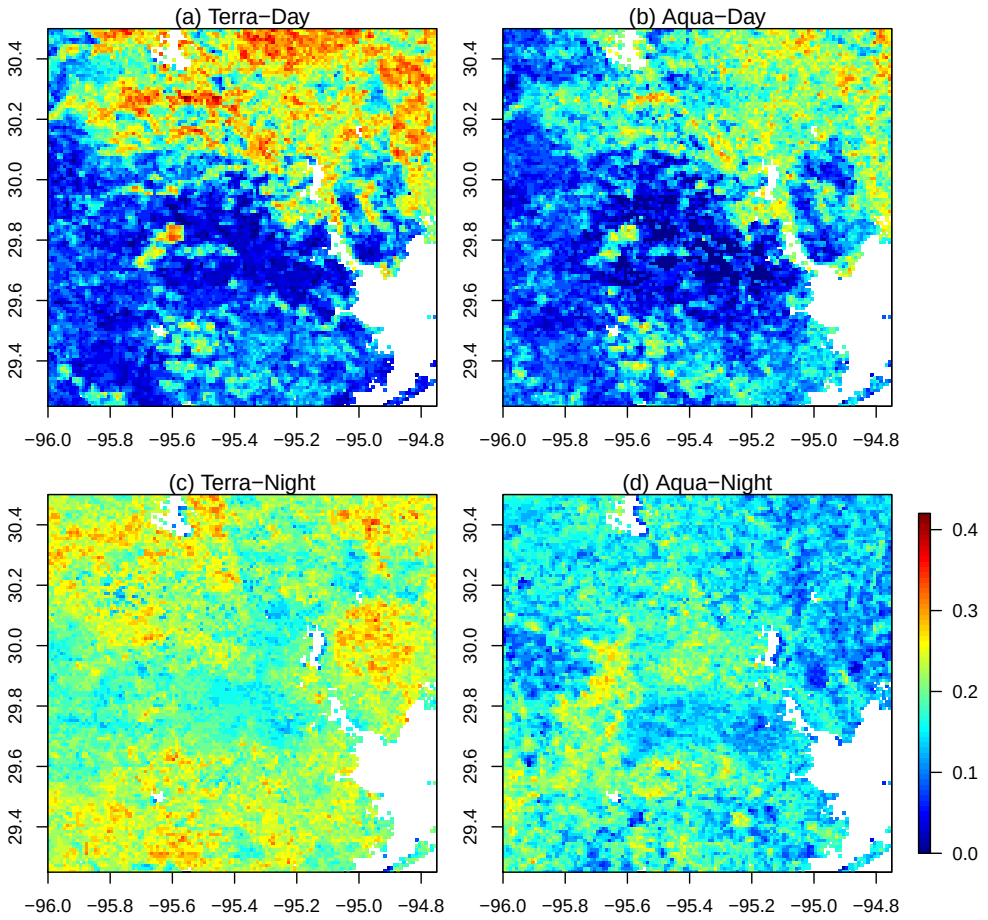

Figure 3.8: The ratio of the temporally consistent days to the total selected 50 days for four times a day.

The MMT method is designed to sample the two ends of the temperature distribution from MODIS and the model. For the observations, potentially it enhances the impact of view angle-induced temperature biases. In order to minimize this effect, prior to employing any of the sampling methods, we masked all of the pixels with view angles larger than 35°. Fig. 3.9 shows the view angle distributions and the corresponding mean MODIS LST of sampled pixels by the MMT method. The nighttime mean LST indicates that warmer pixels slightly coincide with larger view angles, which may be attributed to the warmer radiative temperature of the walls over the roof and

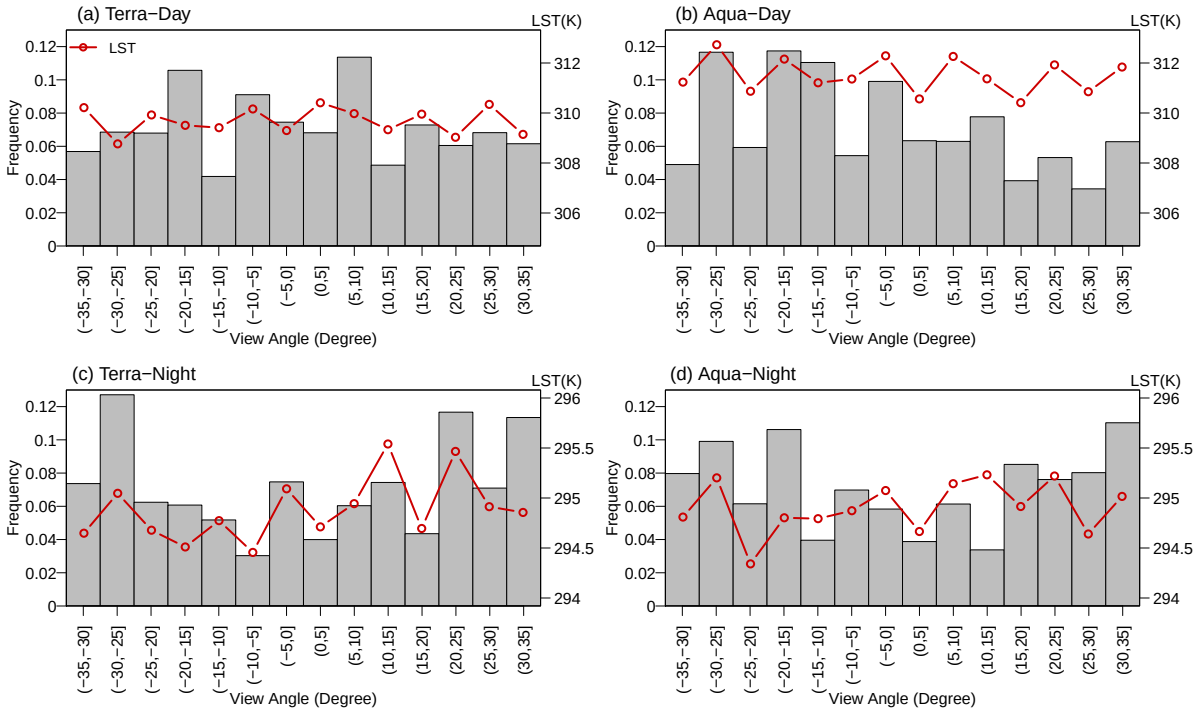

Figure 3.9: The view angle histogram of sampled MODIS LST by the MMT method for four times a day (left y-axis, gray bar) with the mean LST to the corresponding view angle ranges (right y-axis, red line).

roads in the urban area (Kusaka et al., 2001; Voogt and Oke, 2003; Lagouarde et al., 2012). However, the temperature trend here is not statistically significant. The nighttime temperature ranges from 294.5 K to 295.5 K, which is less than the associated daytime temperature variation (about 2K). Further, the similar statistics for each urban land cover type and rural area (not shown) show that LU and rural types share similar LST trends related to view angles with Fig. 3.9, while HU and CU have larger LST variations due to insufficient pixels for some view angles. In summary, the strategy of excluding the larger view angles efficiently decreases the view angle impact on LST.

3.5 Discussion

Before sampling data for model validation, we must be clear about several important facts of using satellite remotely sensed data. First, the overpass time of the satellite is not constant. There is approximately a two hour range for a given MODIS overpass, so we choose a median time for

which to make the comparison of MODIS LST to HRLDAS-simulated T_{rad}. Consequently, biases may be introduced by temporal gaps. The impact will be larger for the daytime than nighttime because the components of the surface energy balance are generally larger and more variable during daytime. Also, the periodicity of sun-synchronous satellites is not frequent enough for determining diurnal variation. As a result, the diurnal temperature range calculated from the MODIS day/night difference is unlikely to match the traditional definition, defined as the difference between daily maximum and minimum temperatures. Less ``diurnal´´ information is available due to cloud distributions varying at the pair of overpass times. Second, the thermal angular anisotropy should be considered because of atmospheric correction, surface geometry, solar zenith and azimuth angles, surface materials, etc. Correcting MODIS LST or simulated T_{rad} view angle over large areas is not practical at this stage. Consequently, we only selected the MODIS data within view angles $\pm$ 35° from nadir, which we demonstrated was an effective approach for view-angle-dependent biases in MODIS LST. These facts will be also valid for MODIS LST product Version 6, because the difference between Version 5 (used in this study) and Version 6 products is very small in all regions except for hot and warm bare soil zones (Wan, 2014). For other narrow-swath satellite remote sensors, view angle may be less influential. Additionally, we had the advantage of having 10 years of data, and therefore retained a large sample of MODIS data for comparison, even after omitting the passes with large view angles. Lastly, clouds can strongly impact the accuracy and applicability of thermal remote sensing data. The sampling methods we proposed are aimed at minimizing cloudy pixels in both the MODIS LST data and simulations.

By selecting only cloud free pixels for comparison, there is the likelihood of biasing the comparison towards warmer daytime conditions (Hu and Brunsell, 2013). However, the validation of a clear-sky case could be the most robust test of how the model surface energy balance performs since it is expected to maximize the differences with variations in surface conditions in the clear-sky cases. Due to the limitation of remote sensing system, the land surface temperature can not be directly measured under the partial-cloudy or cloudy conditions. Bisht and Bras (2010) developed the remote-sensing based estimation of net radiation under all sky conditions. However, the surface

temperature and other parameters under cloudy conditions are the result of global model analyses or regressions based on the in-situ measurements. The model validation for long-term simulations is still challenging under cloudy conditions.

Three sampling methods for validating model simulations versus MODIS LST are proposed and compared. Table 3.2 summarizes the major advantages and disadvantages of each sampling strategy. The length of model simulation and the climate of the study area will affect selection of the optimal method. Generally, if the study area is a cloudy region, such as Houston, we recommend using the SCM method to maximize the sample size of observed data. The HCF method is also an acceptable choice, but may lack representativeness due to small sample size. If the study area is predominantly sunny, such as Phoenix, the difference between the SCM and HCF methods should be modest. The MMT method may be complimentary to the SCM and HCF methods, in that it can be used to evaluate model performance for extreme cases, and it provides an implicit test of the agreement of the simulated-versus-observed cloud distributions. The HCF method is a better choice when simulations are only available for a short period. In summary, each sampling strategy has its own best applicable situations. If the length of simulation or cloud conditions are not limiting factors in the study area, it is also a plausible approach to employ all three approaches for model validation, because each has different strengths.

The thresholds for the processing as well as for the MMT and HCF methods can be adjusted for the specific application. The choice of view angle threshold requires balance between the sample size and LST accuracy. If modelers are interested in extreme events, for the outlier exclusion, it is also reasonable to keep the tail of the temperature distribution on the side that is unaffected by clouds or keep a larger portion of the tails.

For the MMT method, the number of warmest days/coolest nights depends on the minimum number of nearly cloud-free days/nights in the study area, so that we can have relatively large coverage for spatial comparisons. Besides the MMT method, there is another option to select certain high and low quantiles for days and nights in each pixel. This strategy guarantees spatial coverage, but sacrifices the equality of sample size in each grid point. We tested 50% of the

Table 3.2: The advantages and disadvantages of the three proposed sampling methods.

Strategies	Advantages	Disadvantages
SCM method	• The largest possible sample size • Temporally consistent • Diurnal temperature comparison • Long term comparison	• Unequal sample size in each grid box • Possible cloud contamination • Possible cloud mismatch
MMT method	• All samples are cloud-free • Equal sample size from each grid point • Sampling extremes	• Temporal inconsistency • Only apply to long-term data • Unsuitable for year-to-year variability, or time series analysis • Unable to do diurnal temperature comparison
HCF method	• Temporally consistent • Spatially consistent • Likely equal sample size from each grid point • Suitable for case studies	• Small sample size • Unsuitable for year-to-year variability, or time series analysis • Hard to do diurnal temperature comparison

warmest days and coolest nights (not shown), and the LST distributions for each land cover types are similar to the case for the MMT method presented above.

We recommend setting the spatial coverage ratio threshold for the HCF method to be larger than the rural coverage ratio in the domain in this study. For example, we set 90% for the Houston area which is with 25% of urban pixels in the domain, due to the cloud patterns over the metropolitan areas. As shown in Fig. 3.4, clouds occur more frequently over the urban area. The decrease in the spatial coverage threshold may result in enlarging the rural sample size only, which does not benefit the urban temperature comparison.

The SCM method masks all pixels based only on whether clouds exist in the MODIS data. However, it does not mask pixels based on whether clouds exist in the HRLDAS data, because cloud fields are not present in the HRLDAS forcing fields (only fluctuations of longwave and shortwave radiation that may indicate the presence of clouds, though not accurately). Therefore, it is likely that some proportion of HRLDAS pixels which are designated as "clear-sky" by the SCM method may actually be influenced by cloudy or partly cloudy conditions. The effect of this influence is that the HRLDAS simulations that represent "clear-sky" in the SCM method may be cooler during daytime and wormer during nighttime than they otherwise would if they represented clear-sky conditions perfectly. It is therefore recommended that if a user does have access to a cloud mask for their simulations, that they apply it, in addition to the MODIS cloud mask, to both the simulations and the MODIS data to ensure that all pixels represent clear-sky conditions.

The land cover map used for analyses is based on the 30 meter resolution 2001 USGS NLCD. Compared with the MODIS annual land cover product (MCD12Q1) from 2003 to 2011, which are resampled to 1 km resolution, the land cover types and their distributions have some variability. For instance, the total urban pixels in MODIS are about 300 less than the urban pixels defined from NLCD. The major disagreement is with the LU class outside the Houston core urban area, perhaps due in part to having to resample both datasets from their native resolution to the 1 km HRLDAS domain. For rural land cover types, the biggest gap is the wetland in NLCD (25% of total land area in the domain), which is classified as grassland in MODIS (9-year average about 8.2%) in

the north-east corner. Similarly, cropland and natural vegetation mosaics from NLCD are defined as savanna in MODIS. For the land surface temperature, the major impact of this discrepancy in classification is with the emissivity defined according to the land cover type for MODIS, while the related parameters specified for emissivity in the model also differ by land cover type, affecting the radiative temperature. The land cover dynamics and their disagreements are not directly related to the sampling methods, but these differences may be an important contribution to the error for model validation.

Only summer season was discussed in this paper, due to the negative impact of extreme summer heat on human health. Hu and Brunsell (2013) discussed the seasonal cloud distributions during 2000 to 2010 in Greater Houston. The cloud impact is largest during the summer with few cloud-free days and the most heterogeneous clear-sky ratio distribution. Consequently, if we apply these three methods to evaluate the other three seasons, the samples will be more representative for the comparison due to less cloud impact.

We must emphasize that the validation only shows the model performance for radiative temperature. For urban climate modeling applications aimed at characterizing urban extreme heat events and their impacts on human health, air temperature observations must also be considered. Radiative temperature and 2 meter air temperature are highly correlated (Prihodko and Goward, 1997) but determined by different surface processes. Radiative temperature is determined by the radiation budget, which is the part of the energy balance directly affecting the atmospheric temperature from below. Jin et al. (1997) compared the radiative temperature and air temperature at the global scale, finding that the differences are scale dependent and they are more agreeable at larger scales (i.e. monthly scale and hemispheric spatial scales). Voogt and Oke (2003) summarized the relationship between remotely observed radiometric surface temperature and the actual air temperature of the urban-atmosphere interface. The HRLDAS-simulated 2 meter air temperatures are compared to air temperature observations throughout Houston in our companion paper (Monaghan et al., 2014), and the results are similar to those presented here for LST, although the model biases of air temperature are smaller. Therefore, LST-based comparisons may exaggerate the magnitude

of model temperature biases because they are based on skin temperatures as opposed to air temperatures, which typically exhibit smaller diurnal cycles and are less sensitive to changes in the surface energy balance.

3.6 Conclusions

Thermal remotely sensed data are good sources of observations for model validation, with comparable spatial scale, temporal consistency, large coverage, and long-term archives. This study has highlighted several important aspects of satellite LST data that can easily be neglected by modelers for model validation, such as cloud distribution and sensor view angle. From a 10-year case study over Greater Houston during 2003-2012, three sampling strategies were applied to compare MODIS LST with HRLDAS-simulated T_{rad}, temporally and spatially. The assumptions made by each of the strategies were discussed. We assessed the strengths and weakness of the three sampling methods and suggested their best applications. The SCM method gives the best statistical climatological comparison conditioned on the assumed agreement between MODIS clouds and forcing clouds (the longer the time series, the more appropriate this may be). The MMT method gives the best comparison between model simulation and MODIS LST at the extremes in a climatological application. The HCF method gives the best absolute temperature comparison because it is the most consistent, both spatially and between model and observations.

Further research for the view angle correction related to satellite remotely sensed data or model simulations appears warranted, which may further increase the consistency of data properties for validation. Also, the magnitude of impact from temporal gaps between observations and simulations could be tested by modeling exactly at satellite overpass time for each image (beyond the scope of this study). Additional evaluations of the three methods could be performed for other seasons and less cloudy regions. Also, there remains large potential for using other remotely sensed variables to conduct various model validations, such as soil moisture, radiation, precipitation, vegetation indices, evapotranspiration, etc. at multiple scales. Researchers would need to be aware of

the accuracy and limitations of the remotely sensed products before proceeding when comparing different variables.

Chapter 4

A new perspective to assess the urban heat island through remotely sensed atmospheric profiles

4.1 Introduction

The urban heat island (UHI) is a phenomenon where the urban area is warmer than its ambient rural area. The progressive modification of surface covers and structures as well as other human activities cause the UHI. With a growing trend of urban populations, a threat to human health is posed due to the increased temperatures (Kalkstein and Greene, 1997; Patz et al., 2005) and air pollution (Mage et al., 1996; Taha, 1997) in urban environments, which has created wide public concern, especially under the global climate changes. To solve these problems requires intensive investigations of the UHI at multiple scales.

UHI studies are well documented across time and space by using various measuring techniques and temperatures as summarized by Voogt and Oke (2003). Two distinct classes of the UHI are often defined: the atmospheric UHI is assessed through in-situ and vehicle mounted sensors measuring air temperatures in the urban canopy layer (UCL) (Oke, 1976) and through the ground-

based, airborne and tower mounted senors for the urban boundary layer (UBL) (Barlow et al., 2011; Grimmond, 2006; Voogt and Oke, 2003; Roth, 2000); the second class is the surface UHI (SUHI) and is based on the use of thermal remotely sensed data (Voogt and Oke, 2003). Traditionally, the atmospheric UHI magnitude is defined/estimated by comparing air temperature in urban and rural sites (Grimmond, 2006). However, the measurements for atmospheric UHI at urban sites face some substantial challenges. Oke (2007) addressed the detailed siting and exposure requirements for the measurements. Stewart (2011) pointed out that about a half of 190 observational UHI studies have not sufficiently controlled for the essential effects of weather, relief or time to quantify the UHI intensity. Moreover, the limited footprint of the ground-based measurement is difficult to capture a comprehensive distribution of temperature over the highly heterogeneous urban areas. The consistent gridded air temperature data may help to solve the problems for the atmospheric UHI.

SUHI research is thriving after the land surface temperature (LST) data become available (Voogt and Oke, 2003; Gallo et al., 1995). Moreover, the global coverage, temporally consistent LSTs from satellite observations provide a way to estimate air temperature distributions, but the relationship of LST and air temperature remains empirical (Voogt and Oke, 2003). To link the LST and air temperature, many factors must be considered, such as the surface properties, atmospheric conditions and solar angles (Kim and Han, 2013; Vancutsem et al., 2010). Therefore, it becomes difficult to get a simple and consistent estimation for a large area. The air temperature directly retrieved from satellite remote sensing probably has more potential for universal applications of UHI and human health related research, which avoids the scaling issue and the problems associated with the different essential physical factors impacting those two types of temperatures, such as atmospheric conditions and surface properties.

The atmospheric temperature and moisture profiles are important descriptors of the urban environment. Kidd et al. (2009) summarized the progress of satellite-based atmospheric observations and discussed the applications of retrieved atmospheric parameters for improving weather forecasting, extending weather systems monitoring ability, and understanding climate change. Sounding

sensors are typically designed with the horizontal resolutions from tens to hundreds of kilometers. For application over the urban area, the coarse spatial resolutions may fail to capture the surface heterogeneity over the urban area.

The MODIS retrievals of temperature and moisture information at 5 km horizontal resolution can bridge the gaps in an atmospheric UHI study that requires relatively high spatial and temporal observations. These global-coverage data are not only used for atmospheric effect corrections of other MODIS products, such as sea/land surface temperature (SST/LST), but also for capturing the atmospheric features of column water vapor and ozone (Seemann et al., 2006; Borbas et al., 2011). However, the applications of MODIS atmospheric profiles are only discussed in a few studies outside the MODIS product groups, such as the MODIS-based estimation of net radiation (Bisht et al., 2005; Wang and Liang, 2009; Bisht and Bras, 2010) and potential evapotranspiration (Kim and Hogue, 2008). These studies directly estimated the surface temperature and moisture from MODIS product without quantifying the accuracy. The error propagation from the MODIS product may explain part of the errors in their estimations.

Moreover, the spatial distribution of temperature does not solve UHI quantification problems as a result of unclear urban-rural division at the current stage (Stewart, 2011). Schwarz et al. (2011) concluded that different SUHI indicators have weak correlations, and emphasized the critical role of choosing indicators to quantify SUHI effects. It becomes very difficult to conduct the intercomparison among the UHI studies in the literature due to the unstandardized indicators. Consequently, a better way to quantify UHI magnitude is required with considering the surface heterogeneity and ambiguous urban/rural divisions.

The purpose of this study is to provide an innovative analysis for using MODIS retrieved near-surface air temperature to investigate the UHI. This study first assesses the accuracy of the near-surface air and dew-point temperatures estimated from the MODIS 07 atmosphere profiles over the urban area and its ambient rural area by using long-term ground observations. Both Terra and Aqua overpasses are investigated due to the potential applications to address UHI effects for both day and night. Moreover, according to the strengths of the MODIS air temperature, we

developed a city-dependent UHI curve as a function of urban fraction, which is able to integrate the spatially heterogeneous physical properties and long-term variation of temperature to quantify UHI intensity.

4.2 Study Area and Data

4.2.1 Study Area

Four mega cities in North America are selected for this research: Phoenix, Houston, Chicago and Toronto. Fig. 4.1 shows the domains and 2012 land cover distributions of the four cities. According to NOAA's national coastal population report, about 39% of the U.S. population live in coastal areas in 2010 (NOAA National Ocean Service, 2013), so three cities located near/on the shoreline were chosen. Chicago and Toronto, with similar geographic location and prevailing weather conditions, are featured as the humid continental climate with warm/hot and humid summers. Although, the higher latitude and location near the Great Lakes may help decrease the energy consumption for air conditioning, the population growth and climate change may put these cities under the exposure of a higher heat vulnerability. Houston is located in the humid subtropical climate zone, known for hot and very humid summers. Phoenix is under a subtropical desert climate with extremely hot and clear summers. It is important to include cities with very clear and very cloudy summers to extend the understanding of the performance of the MODIS data.

4.2.2 Satellite Data

The MODIS atmospheric profile product (MOD07_L2 for Terra and MYD07_L2 for Aqua, hereafter MOD07_L2 for MODIS 07 product) for 5-minute Level-2 Collection-6 was processed from 2003 to 2013 in June-July-August (JJA) for both daytime and nighttime overpasses. The median local stand time of each satellite overpass for four cities ranges from 10:30 - 11:05 (Terra-Day), 21:15 - 22:15 (Terra-Night), 12:25 - 13:20 (Aqua-Day), 1:35 - 2:10 (Aqua-Night). MOD07_L2

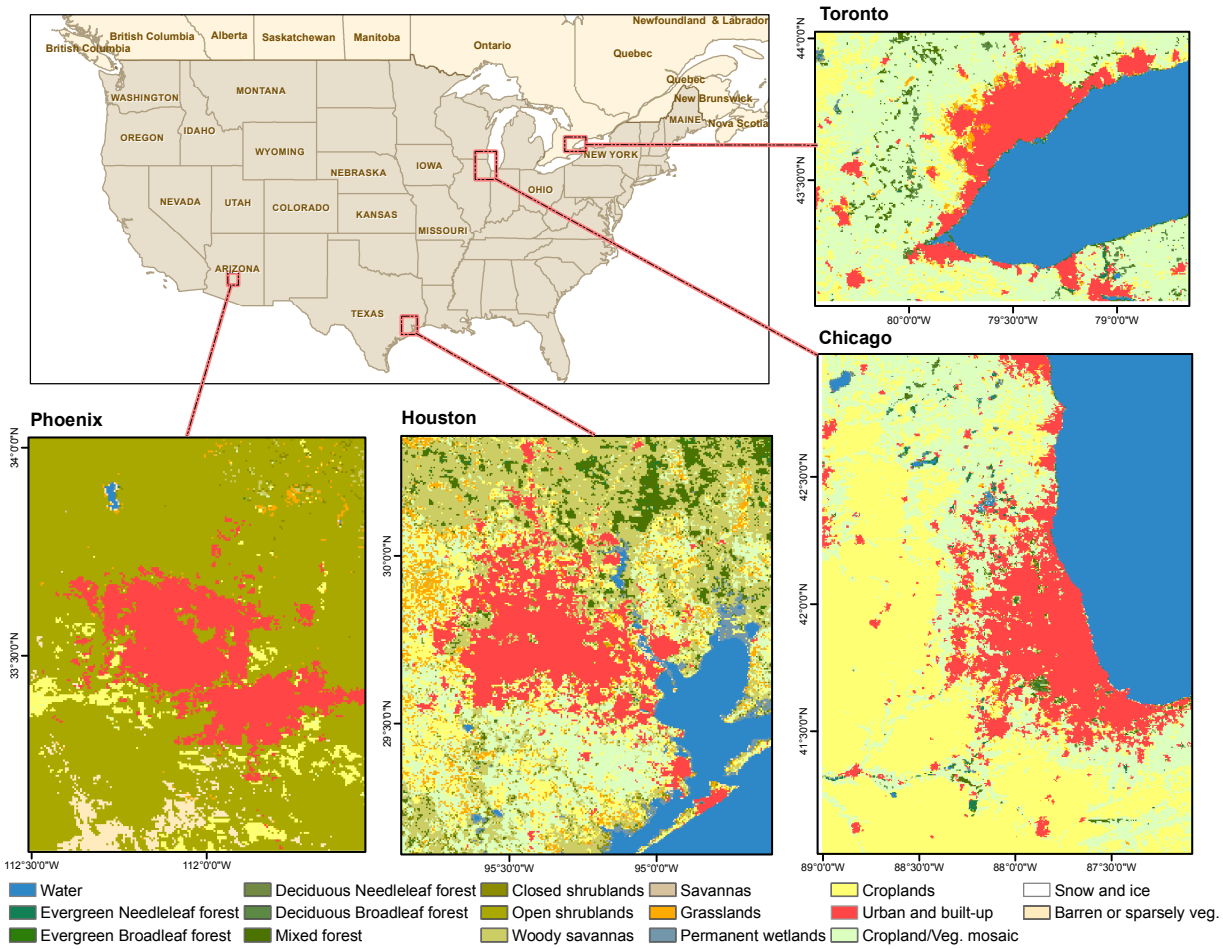

Figure 4.1: The city domains and the land cover distributions in 2012 of four cities: Phoenix, Houston, Chicago, and Toronto. The land cover maps are IGBP land cover classification from MODIS MCD12Q1 product at 500 m.

product consists of temperature and moisture profiles (20 pressure levels: 05, 10, 20, 30, 50, 70, 100, 150, 200, 250, 300, 400, 500, 620, 700, 780, 850, 920, 950, and 1000 hPa), total-ozone burden, atmospheric water vapor and other atmospheric information in clear skies at 5 km horizontal resolution.

The MOD07_L2 temperature and moisture sounding data are retrieved from MODIS multispectral thermal radiation measurements. The MODIS retrieval algorithms (Seemann et al., 2006) are adjusted from the TIROS (Television Infrared Observation Satellite) Operational Vertical Sounder (TOVS) algorithms (Reale, 2002) and Geostationary Operational Environmental Satellite (GOES) Atmospheric Sounder algorithms (Menzel and Purdom, 1996), which are based on a statistical regression retrieval (Seemann et al., 2003). Further details regarding the retrieval algorithm and MOD07_L2 Collection 6 quality can be found in the product algorithm theoretical basis document (Borbas et al., 2011). In general, MODIS has a limited ability to capture the fine-scale vertical structure compared to the high spectral resolution sounding sensors (e.g. Atmospheric Infrared Sounder (AIRS) (Aumann et al., 2003)), but it provides higher horizontal resolution of temperature and moisture distributions. This is useful to help understand the urban climate by capturing the urban surface heterogeneity globally for a long-term perspective.

To estimate the near-surface air temperature, the digital elevation model (DEM) from U.S. Geological Survey (USGS)'s National Elevation Dataset (NED) was used instead of the surface elevation (SE) layer from the MOD07_L2 product. The SE varies temporally, which is estimated from the surface pressure. To match the spatial resolution of the MOD07_L2 product, the DEM is upscaled from the original 30 m to 5 km by averaging. The mean differences between DEM and SE over the area with less terrain variations (where most of the cities are located) are small, while the mountainous areas result in larger gaps up to 100-200 m.

The yearly MODIS land cover product (MCD12Q1) at 500 m resolution from 2003 to 2012 was used for discrimination of urban and rural pixels in UHI analysis. The 2012 land cover information was used for 2013 due to the unavailability of 2013 land cover data.

4.2.3 Ground Observations

The Integrated Surface Global Hourly observations from the National Climatic Data Center (NCDC) (`http://www.ncdc.noaa.gov/cdo-web/datasets`) were used for validation. Observations were filtered based on the following criteria: 1) observational data passed all the quality control checks, 2) the observation time was within satellite overpass $\pm$ 1 hr, and 3) the observation sites were within the study domains. After preliminary statistics, the site in Elora RCS, Toronto (USAF ID: 713520) was removed due to the presence of many below-freezing records in summer. Fig. 4.2 illustrates the ground observation locations with a the black empty circle (the sites in the 5 km pixel not classified as a water pixel), and a black cross (the sites in the 5km pixel with water pixels). A summary of the ground sites is given in Table S1 in the supplemental document.

4.3 Methodology

The MOD07_L2 is formated in orbital swath. The primary reprocessing requires mosaicing, reprojection and subseting, which were done by using HDF-EOS to GeoTIFF Conversion Tool (HEG) (`http://newsroom.gsfc.nasa.gov/sdptoolkit/HEG/HEGHome.html`). The layers from MOD07_L2 air temperature, dew-point temperature, and geopotential height profiles (converted to geometric height), and the DEM from USGS were converted into a consistent extent and resolution for each city.

4.3.1 Instantaneous Near-surface Air and Dew-point Temperatures

The methodology to estimate the near-surface air and dew-point temperature (T_a^S and T_d^S) was to extrapolate the lowest pressure level temperature/moisture information (T_a^L and T_d^L) from MOD07_L2 profiles to the surface elevation from the DEM under the hydrostatic atmosphere assumption. Because the estimation is primarily determined by the mean surface elevation at the 5 km resolution, it does not explicitly distinguish between urban and rural surface structure. Although we called the "near-surface" temperature, it is more likely to be at the top of the UCL.

First, the geopotential height is converted to geometric height based on the gravity of the city locations. Bisht and Bras (2010) use a constant lapse rate (6.5 K/km) over the Southern Great Plains. However, considering the urban surface heterogeneity, environment lapse rate (Γ_e) was assumed to vary spatially and was calculated for each pixel by using temperature and height information at the two lowest layers of the profiles:

$$\Gamma_e = -\frac{\partial T}{\partial z} \simeq -\frac{T_a^{L1} - T_a^{L2}}{z^{L1} - z^{L2}} \tag{4.1}$$

where T_a^{L1} and T_a^{L2} are the air temperature at the lowest and the second lowest levels of MODIS sounding near the surface; and z^{L1} and z^{L2} are the geometric heights corresponding to T_a^{L1} and T_a^{L2}.

Assuming that the lapse rate is constant near the surface for each pixel, Γ_e at the lowest profile level was applied to the surface level. The near-surface air temperature (T_a^S) can be calculated by:

$$T_a^S = T_a^{L1} - \Gamma_e(z^S - z^{L1}) \tag{4.2}$$

where z^S is surface elevation from the DEM.

Similarly, Eq. (4.1) and Eq. (4.2) can be applied to estimate the near-surface dew-point temperature (T_d^S) by using dew-point lapse rate (Γ_w) and the dew-point temperatures at the two lowest levels (T_d^{L1} and T_d^{L2}) of MODIS profiles.

The MOD07_L2 product quality is sensitive to the presence of clouds and cloud contamination detection. The MODIS cloud mask product (MOD35_L2) was used for cloud screening. Moreover, the profile retrieval requires at least 5 out of 25 pixels (1 km resolution at nadir) in a 5 $\times$ 5 field-of-view area (around 5 km) with a 95% or greater confidence of clear sky (Borbas et al., 2011). In addition to clouds, other factors may cause unrealistic profiles, e.g. a sharp change in atmospheric structure. Quality controls were applied to the near-surface air and dew-point temperatures to exclude the "bad" atmospheric profiles and near-surface temperatures. We removed a few outliers that the MODIS air temperatures are higher or lower than the historic records $\pm$ 5 K. For example, the high threshold for Phoenix is 328 K (323+5 K), while the low threshold is 277 K (282-5 K).

The 5 K buffer was set for the possible bias for MOD07_L2 product. Also, the pixels with a dew-point temperature higher than the air temperature were considered invalid pixels under clear sky conditions.

4.3.2 Urban Heat Island Curve

Current studies have investigated the relationship between UHI intensity with surface physical properties and social and economic factors, such as population and city size (Oke, 1973), vegetation index (Weng et al., 2004, 2011), wind (Morris et al., 2001; Offerle et al., 2007), building configuration (Coseo and Larsen, 2014; Monaghan et al., 2014; Alchapar et al., 2014), and impervious surface area (Zhang et al., 2010; Imhoff et al., 2010). Fundamentally, the UHI is a direct consequence of human-induced land surface modifications (Oke, 1995). Directly linking surface urban/vegetation area provides the most robust estimation and captures the fundamental features of UHI, because the thermal/physical properties of human-made and natural surfaces directly alter the energy budget and flux partitioning.

We come up with a new concept to quantify the UHI, "urban heat island curve (UHIC)", which is designed to explore the spatial relationship between the air temperature and the urban fraction. Urban fraction is an integrated indicator to show the intensiveness of human activities in a sub-grid scale, usually closely associated with the building density and is a function of factors, such as urban core, suburban, and industrial urban.

Air temperatures were grouped into different urban fraction categories. The urban fraction within a 5 km pixel is simply calculated from the ratio of the urban land cover pixels (MCD12Q1) to the total pixels at 500 m. Land cover in 2012 was used for statistics in 2013 due to unavailable data. We exclude pixels with water bodies because of the strong thermal properties of water, which may skew the trend, especially for the coastal areas. The UHIC is the curve connecting either the median or mean temperature in each urban fraction category.

In this study, we use the median temperature of each urban fraction category as the curve, and also adopt the 25% and 75% quantiles to illustrate the temperature variation. Compared to the

mean and standard deviation as the statistic indicator, the quantiles can effectively limit the impact of extreme heat events to the curve for presenting a long-term trend.

4.4 Results

4.4.1 Spatial Patterns of MODIS Near-surface Air and Dew-point Temperature

In order to investigate the ability of MODIS near-surface temperature over the urban area, spatial averages of the 11-years of air and dew-point temperatures are illustrated in Fig. 4.2 and Fig. 4.3, respectively. The figures portray the averaged day and night satellite overpasses in the UHI diurnal cycle over the four metropolitan areas. In general, the MODIS air and dew-point temperatures suggest a remarkable, fine-scale thermal heterogeneity of near-surface features during both daytime and nighttime.

The UHI intensities vary spatially and temporally. For Phoenix, the dry environmental background around the urban area decreases the contrast of UHI boundary and temperature variations within the city. However, the major urban area did have relatively higher temperatures than the surroundings and lower than the desert in the southwest corner. Houston shows a strong urban/rural temperature contrast during the daytime while it becomes less distinct during the nighttime. Chicago and Toronto demonstrate a very similar diurnal UHI pattern: distinct UHI for both day and night. The quantification of the UHI through time and space are discussed in Section 4.4.3.1.

The urban effect has less influence on the dew-point temperature before noon (Terra-Day in Fig. 4.3). It is commonly true that the urban surface becomes drier in the afternoon due to the urban surface properties (e.g. imperviousness, structure, and thermal properties), limiting the ability to maintain surface moisture and the accumulation of additional energy and anthropogenic heat emissions in the urban canyons. Moreover, the deeper convection developing in the afternoon accelerates moisture dissipation. Consequently, cities usually become moisture deficit (see Fig.S1), evident by high air temperature and low dew-point temperature over the urban area by the time of

the Aqua-Day overpass. The nighttime dew-point temperatures are much higher than the rural surroundings in Toronto and Chicago. This results in a lower moisture in the urban area during Terra and Aqua nighttime passes. There are smaller dew-point temperature gradients between urban and rural area for Phoenix and Houston due to the prevailing dry/wet climate features. The relative humidity over these two urban areas are slightly higher than the ambient rural area (Fig.S1).

In order to assess the overall accuracy of MODIS-retrieved near-surface temperature, the ground observations selected within $\pm$ 1 hr of each satellite overpass time were directly compared with the corresponding MODIS air temperatures under clear-sky conditions during the 11 summers. Fig. 4.4 shows the distribution of air temperatures from satellite and surface observations for the four cities. The results of dew-point temperature are similar and can be found in Fig.S2. The sites shown in the scatter plots include the locations over the urban and rural area without water in the 5 km pixel (empty circles in Fig. 4.2). The statistics of the MODIS and ground observation comparisons over three categories of site locations are presented in Fig. 4.5, including sites in a 5 km pixel with urban area but no water surfaces, sites in a 5 km pixel over the land but no water surfaces, and all the sites in each study domain (including urban, rural and water surfaces) (all sites shown in Fig. 4.2). The urban, rural and water surfaces are determined by the MCD12Q1 yearly land cover data.

Fig. 4.5 indicates that MODIS air and dew-point temperatures are generally underestimated. For air temperature, Aqua data show a better agreement with the ground observations than Terra, which is about 1-6 K smaller than Terra for the mean of differences (MD). Nighttime air temperatures agree better than the daytime in most cases. Although the RMSE ranges from 3-7 K, most cases are due to the total bias which can be easily corrected. In contrast to the air temperature, the daytime dew-point temperature generally indicates a better agreement, showing that daytime RMSEs is about 0.3 - 2.2 K smaller than nighttime RMSEs.

In general, the results of the cities under very dry or humid climate conditions suggest a poorer detectability of MODIS retrievals or larger errors, which may result in more challenges to correct for these effects. For example, the slope of the linear regression between the MODIS and ground

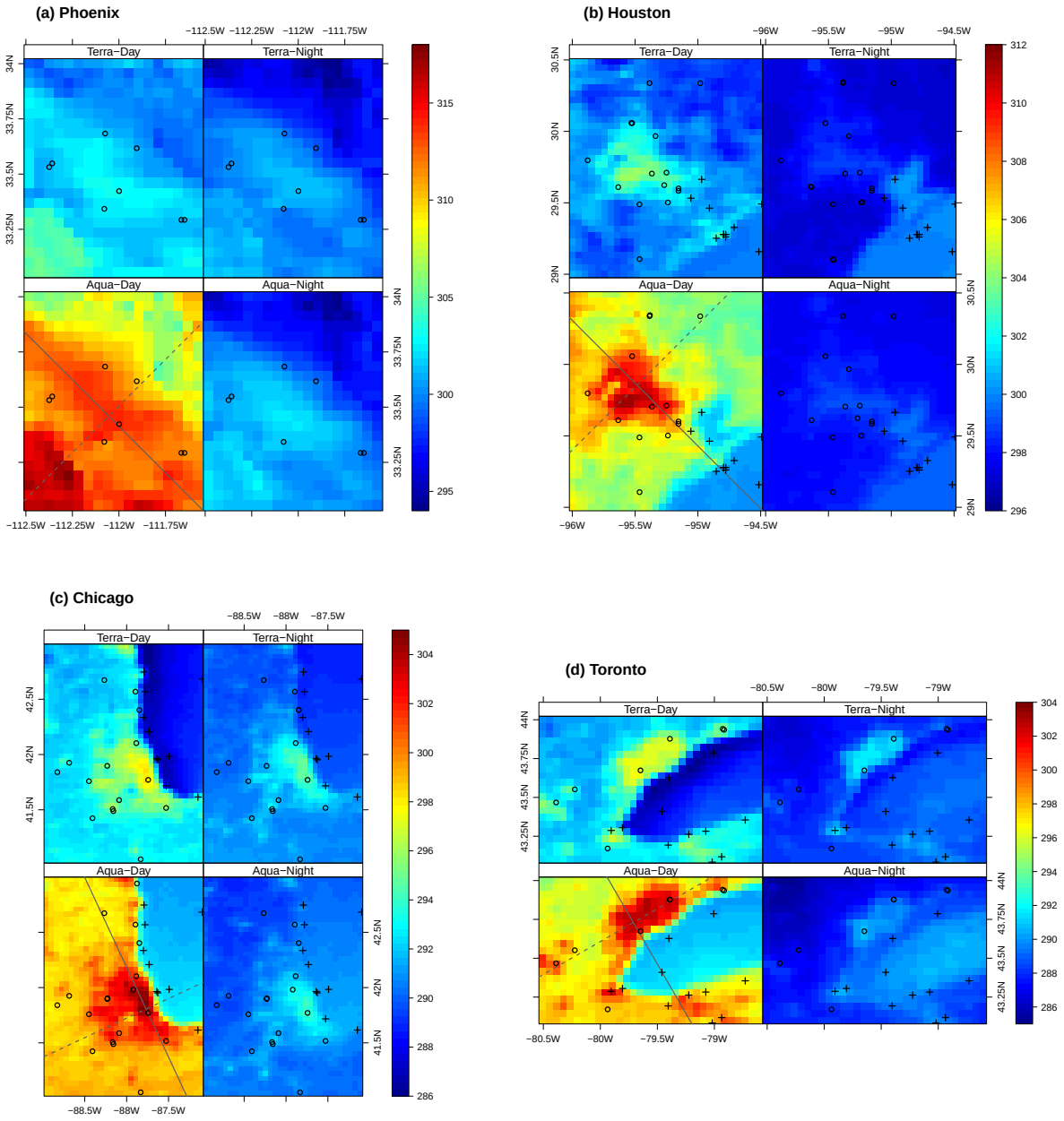

Figure 4.2: The 11-year JJA mean near-surface air temperature (T_a^S) of four cities with the hourly ground observation locations. The empty circle indicates the sites in 5 km pixel without water fraction. The black cross indicates the sites with water fraction in the pixel. The two gray lines in the Aqua-Day image depict the transect lines for **Fig. 4.6**, where a solid line is Transect 1 and a dashed line is Transect 2.

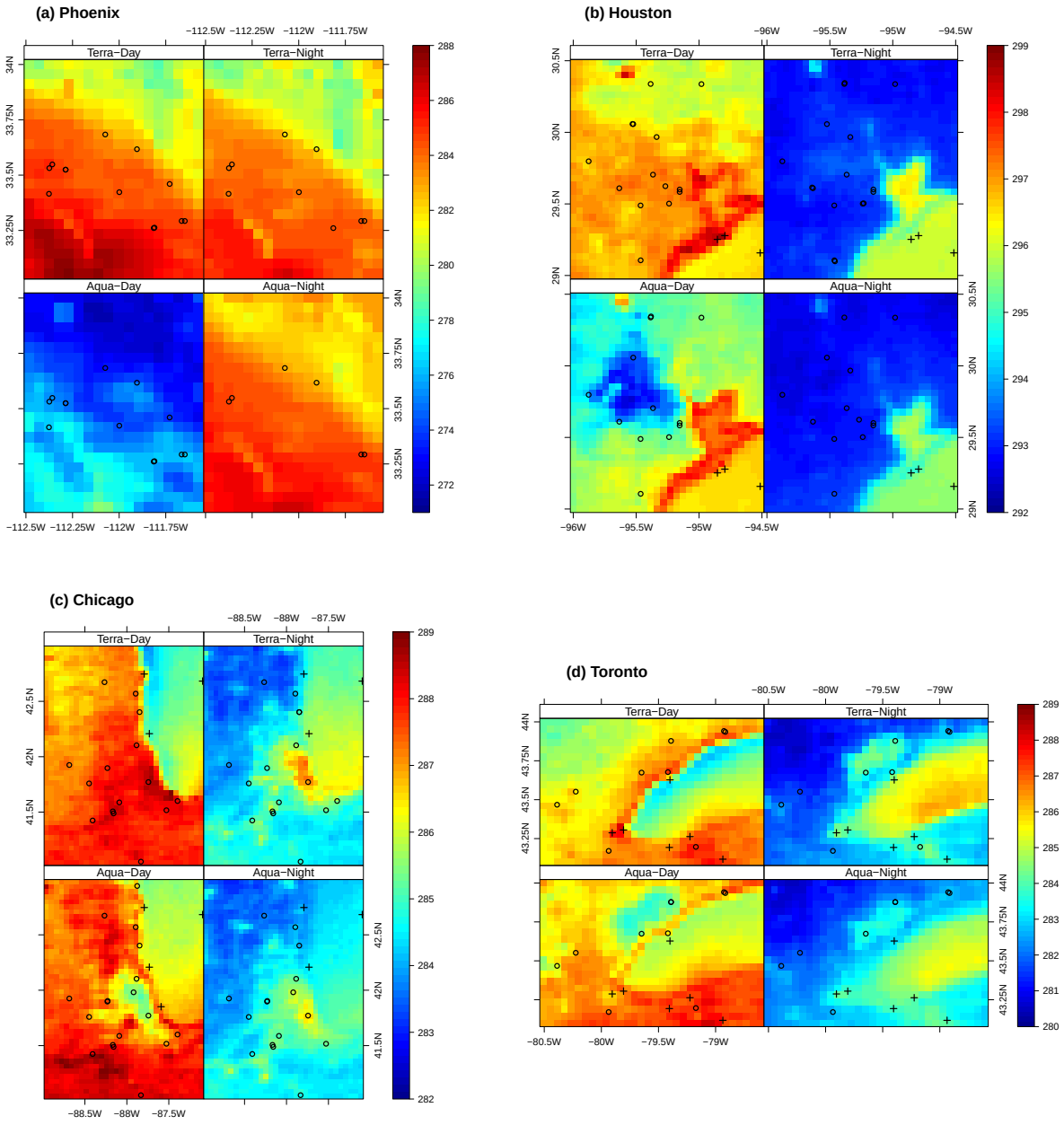

Figure 4.3: The 11-year JJA mean near-surface dew-point temperature (T_d^S) of the four cities with hourly ground observation locations.

observations are significantly different from 1 for the nighttime dew-point temperature in Phoenix. The detectability of MODIS for moisture is reduced when the dew-point temperature is low (see Fig.S2), approximately ranging from 260-280 K. In Houston, the temperature variation is small for each satellite overpass period with a less clustered distribution in relation to the reference line in the scatter plot. This possibly explains the large variation of linear regression slopes in Fig. 4.5. Although the RMSE and MD are sometimes even smaller than other cities, the degree of inaccuracy is difficult to reduce after the corrections. Relatively large air temperature differences exist for Terra, and the dew-point temperature biases occur during the nighttime, so some necessary corrections regarding the observations may need to be applied.

However, the factors related to the mismatch of spatial scale, surface heterogeneity, as well as the possible 1 hr observational temporal gap need to be taken into account for the error. Also, the uncertainty in the measurement height will impact the results of the comparison.

This research is attempting to illustrate the applicability of MODIS atmospheric profile product for UHI studies, and the temperature gradients are more emphasized than the absolute temperature magnitude. Consequently, no data correction is provided in this study. The following analysis of the vertical temperature structures and UHIC will focus on Aqua air temperature, which has relatively high accuracy.

4.4.2 Vertical Structure of UHI

The 3-dimensional temperature field may help advance our understanding of the impact of urban surfaces on the lower layers of the atmosphere. Fig. 4.6 illustrates the 11-year JJA mean vertical air temperature distributions along two orthogonal transects (shown in Fig 4.2 Aqua-Day) for each city. The daily atmospheric profiles and near-surface air temperatures were interpolated into 50 m vertical resolution by cubic spine interpolation, and then averaged for the 11 summers. Only Aqua data are plotted here due to the higher quality of near-surface air temperature, and the Aqua daytime period is also closest to the maximum temperature during the day.

The vertical temperature structure reflects the dramatic impact of surface heating extending

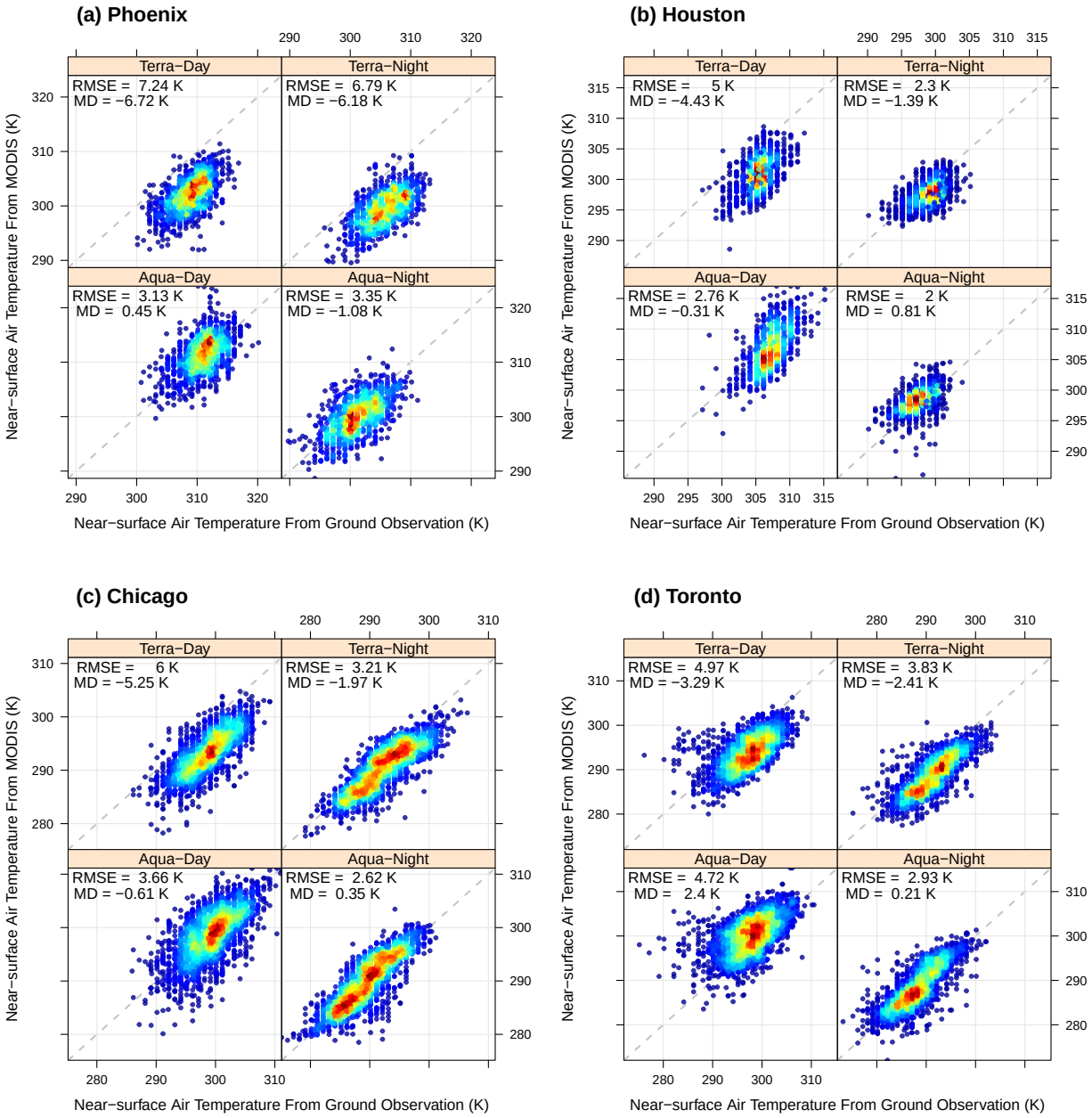

Figure 4.4: The density scatter plot of near-surface air temperature from ground observations (the sites denoted as empty circles in Fig. 4.2) and the MODIS product. The point density from low to high is expressed as the color ramp from blue to red. RMSE is the Root-Mean-Square Error, and MD is the Mean of the Differences between MODIS estimations and ground observations in K.

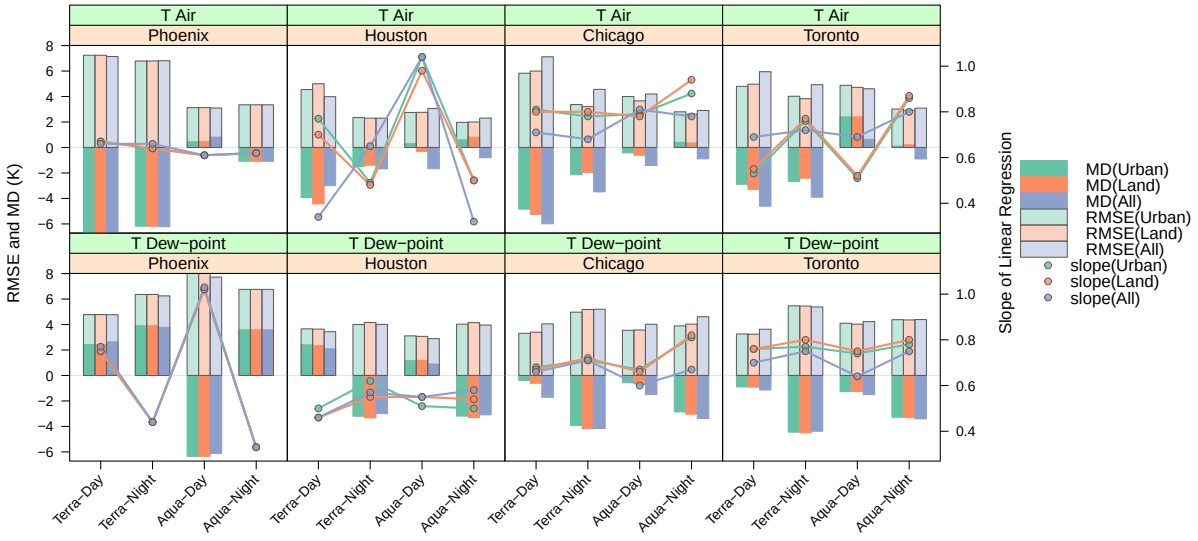

Figure 4.5: The Root-Mean-Square Error (RMSE), Mean of the Differences (MD), and the slope of the linear regression between the ground observations and MODIS estimations for three site categories: sites in a 5 km pixel with urban fraction (no water fraction), sites in a 5 km pixel of land surface (no water fraction), and sites in the domain. The near-surface air temperature is shown in the upper-panel plot, and the near-surface dew-point temperature is in the lower row.

into the lower-level atmosphere (Fig. 4.6). The horizontal temperature gradient is interrupted by the change of hot or cool locations with different land cover composition. One transect of each city is coincident with the dominant wind directions. According to the land cover distribution along the transects, the heat distribution in the downwind (sea/lake breezes) directions is evidence of advection during the daytime.

Phoenix is the only inland city in this study with a relatively flat terrain in the urban area and mountains around the city in the domain. Transect 1 and Transect 2 (gray dashed line in Fig. 4.2) are coincident with the dominant wind direction at Aqua-Night and Aqua-Day, respectively. Multiple factors, such as elevation and land cover distributions, including vegetation, urban and desert, play essential roles impacting UHI features. Although the desert at the southwest corner of the domain (western proportion of the Transect 2) has a higher temperature, the heat from the urban area could still be detected due to the relatively lower temperature in the area transitioning from vegetation and higher elevation (Fig. 4.6 (a) Transect 2). For the other three cities near water

bodies, the shapes of the heat dome have a relatively clear boundary associated with the surface land cover types.

4.4.3 Application of MODIS Air Temperature for UHI Assessment

4.4.3.1 Urban Heat Island Curve

With the spatial distribution of summer air temperature for 11 years, the urban heat island curves (UHIC) are shown in Fig. 4.7 for the four cities and four satellite-overpass periods. The 25%, 50% and 75% quantiles of air temperature for each group of urban fraction reveal a city-dependent temperature trend. The median of air temperatures of fully vegetated pixels is added as a reference line (gray dashed line in Fig. 4.7). The data from the Terra overpass showed a low bias (about 3.3-6.7 K for daytime and 1.4-6.2 K for nighttime) compared to the ground observations (in Section 4.4.1). With an assumption that the bias is spatially consistent, the shape of the UHIC and the difference between the UHIC and the fully vegetated temperature line are less impacted by the total bias of MODIS air temperature.

Compared with pairs of urban-rural temperature differences, the UHIC incorporates the spatial heterogeneity of the whole city domain in the curve, resulting in a unique pattern for each city. The air temperature showed a positive slope as a function of urban fraction. The magnitude of slope varied temporally and spatially. For example, the air temperature differences among the pixels with 60% and higher urban fraction in Phoenix were small, which is related to the local climate and vegetation types in the non-urban fraction. However, a positive slope was observed among the lower urban fraction groups (1% - 45%). In the Greater Houston, the UHIC slope became very steep during the daytime (about 3.0 for Terra-Day, and 4.6 for Aqua-Day), suggesting a large impact of the urban surface that contributes to the higher air temperature. Comparably, the nighttime UHIC of Houston increased steadily and slowly, with the slopes of 0.8 and 0.7 for Terra and Aqua night, respectively. The UHICs of Chicago have relatively similar steep positive slopes for both day and night, ranging from 2.1 to 3.2. There is a large variation of Toronto Aqua-Day UHIC; however, the trend was still positive with a slope of 1.85. Other times of day for Toronto

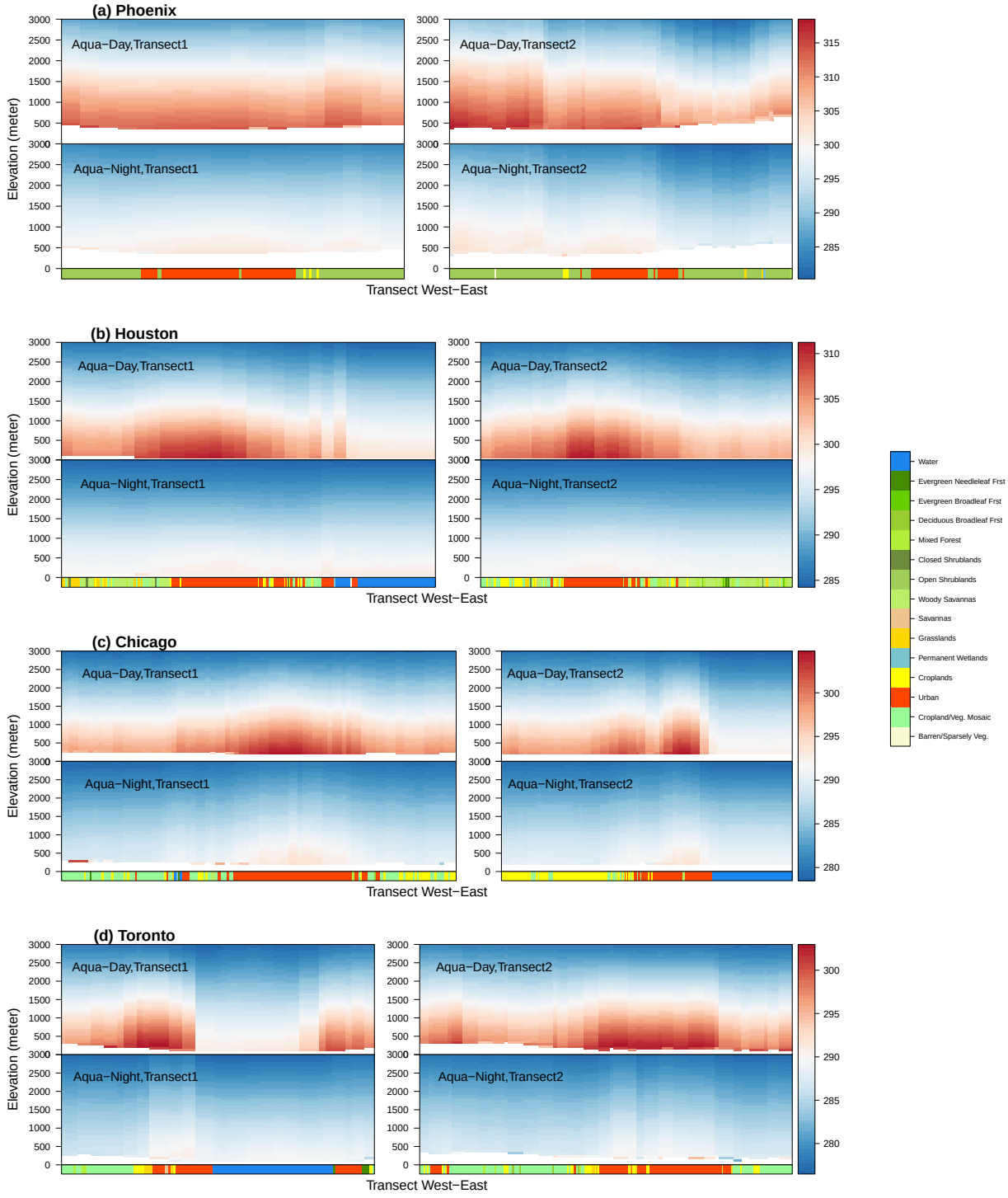

Figure 4.6: The mean vertical temperature distributions from Aqua distribution along two orthogonal horizontal transects for both day and night conditions for the four cities. The bottom color bar indicates corresponding land cover types along the transects. The white area at the bottom represents the ground below the surface elevation.

revealed a steady increase (with a slope of 3.5) in temperature with increasing urban fraction. The large variation may be impacted by some scattered urban areas around the lake in the domain, especially during the times with strong fluxes. These results support the widely accepted fact that UHI is primarily caused by the urban modification to the surface energy balance (Stewart and Oke, 2012). Moreover, the UHIC reveals more spatial complexity impacting temperature variations in space and time than other UHI indicators.

The gray dashed line in Fig. 4.7 presents the median temperature of fully-vegetated pixels in each domain. The dominant vegetation types around the cities are shrublands (Phoenix), croplands and savannas (Houston), croplands (Chicago), croplands and natural vegetation mosaic (Toronto). The maximum median temperature differences between urban and pure vegetation are also shown in Fig. 4.7. A comparison between the air temperature with low urban fractions and the pure-vegetation temperature showed a slightly different magnitude in most cases, which can be explained by the influence of the urban fraction as well as the ambient pixels when considering the clustered pattern of urban surfaces. The majority of urban pixels at the 5 km resolution are a composite of urban and vegetation. Pixels with water fraction are not considered in the UHIC. However, pixels with urban fraction in Phoenix may also consist of the barren soil, which increases the temperature difference from the fully-vegetated pixels.

In general, each city had very similar UHIC shapes for different time periods, which is largely determined by the land use pattern and dominant vegetation types. For example, the concave part of the curve, showing a higher urban fraction but lower air temperature, may be a result of one or multiple inexplicit reasons, such as elevation, building types and heights, surrounding land cover types (parks versus industrial), the vegetation types or the irrigation management in the non-urban fraction. Moreover, the variation of UHIC reveals the air temperature partially determined by the surface properties. The Aqua-Day (early afternoon) reveals the largest variation while nighttime UHIs have smoother UHIC.

The light-green bars (right y-axis) in Fig. 4.7 indicate the number of pixels in each urban fraction category. This value accounts for two main factors: the number of pixels with a certain

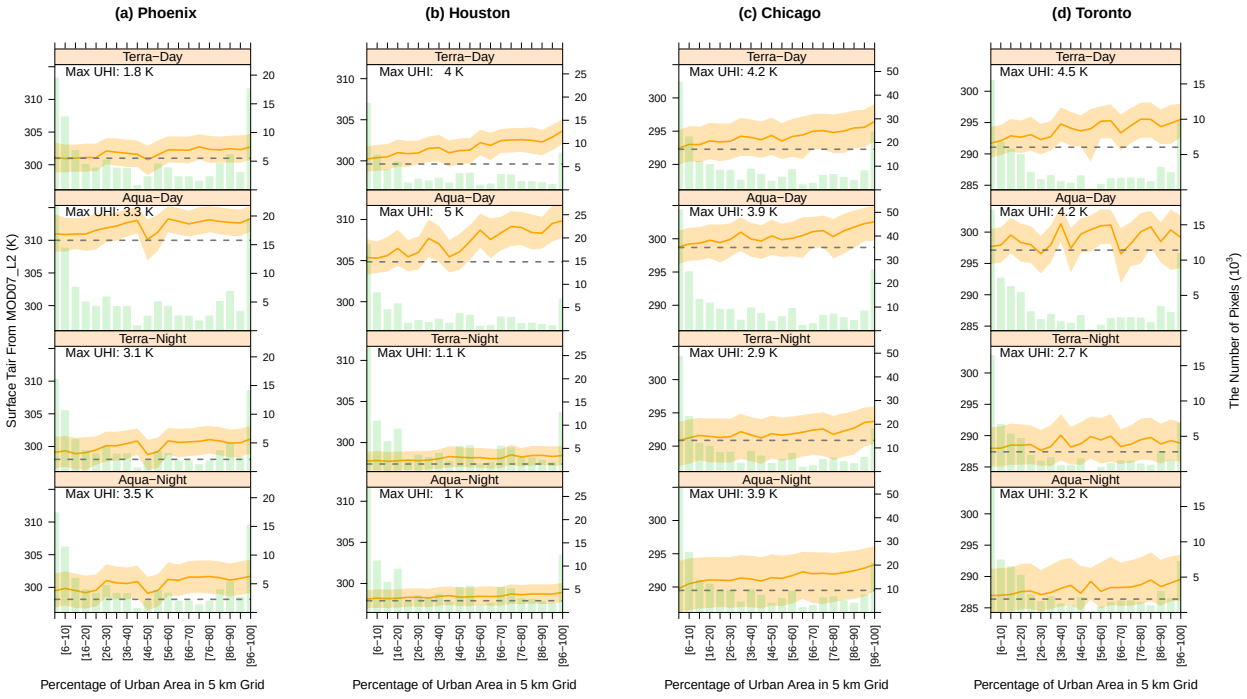

Figure 4.7: The UHIC of four cities as a function of urban fraction (at 5% interval) in 5 km pixel using 2003-2013 JJA data. The solid orange line is the median air temperature of the pixels with corresponding urban fractions (left y-axis). The shaded orange area indicates the 25% and 75% quantiles of the air temperature distributions (left y-axis). The light green bar plot (right y-axis) shows the number of pixels in each group for the statistics for 11 year summers. Max UHI is the difference between the highest median air temperature on the UHIC and mean vegetation temperature.

urban fraction in each city and the number of clear days for 11-year JJA. The "U-shape" distribution of pixel numbers along with the urban fraction increasing may depict the urban density decreasing from the urban core. However, the higher urban density is more likely to be cloudy due to the strong convection during the late afternoon (Hu and Brunsell, 2013). The UHIC is based on robust statistic for the 11-year summers under clear-sky conditions. Some attention needs to be paid to the categories with relatively small sample sizes, e.g. 75 for Terra-Night and 93 for Aqua-Night with urban fractions of 51%-55% in Toronto. This may decrease the confidence level of the variation in the UHIC.

4.4.3.2 Yearly Trends of Urban Heat Island

Taking advantage of consistent long-term observations, we calculated the annual trend of urban/rural temperature for UHI dynamics (Fig. 4.8). In this section, we chose one indicator to exploit the monthly 11-year UHI by using the temperature difference between urban (more than 60% urban fraction) and fully vegetated pixels. Daily records require that more than 30% of the urban pixels are available in clear sky. The monthly statistics required more than 3 days of records (e.g. 2004 August in Houston are removed). From this indicator perspective, the UHI intensity is more characterized by the locations and prevailing climate conditions in general, which agrees well with the UHIC analysis (Fig. 4.7).

The urban and vegetation temperatures are significantly correlated, being determined by the larger scale climate. However, the magnitudes of urban/vegetation temperature differences vary slightly and are inconsistent, which may be the result from the vegetation conditions controlled by precipitation, agriculture management, etc. This paper focuses on the MODIS air temperature ability to capture the UHI, and more research is needed.

The near-noon/midnight ground observations were used for the temporal dynamics analysis instead of the Aqua overpass times, so more records were available for the sites in each domain, which can give a better depiction of temporal temperature variations. Although the times vary within a two hour timespan, we chose to compare the trends rather than the absolute differences,

which would decrease the influence of time. The annual trends from the ground observations located far from the water bodies (the light solid line with a star sign in Fig. 4.8) are fairly comparable with MODIS air temperature in most cases. However, some trends are opposite during certain periods, e.g. 2008-2010 JJ for Toronto, 2009 June for Phoenix. It is important to point out that there are several reasons for a discrepancy between the ground and satellite observations, including: the ground sites are unevenly distributed in space, mostly located in the low density urban and rural areas of the domain; the measuring length for each site differs within the 11-year period; and the sky-conditions are not taken into account for the comparison. Possibly, those factors contribute errors to a certain extent. The factors related to time, space, scale, and sky conditions between the ground observations and MODIS estimations hamper the direct comparison for the long-term trends validations. The MODIS product has a more consistent quality in time and space, which at least, is still able to provide valuable information for research on gradients, such as the UHI.

4.5 Discussion

As is widely known, MODIS is not designed for sounding purposes. However, the information provided at high spatial resolution can "improve upon a priori definitions of atmospheric state by providing better delineation of horizontal gradients (King et al., 2003)". MODIS-derived air and dew-point temperatures in this study show an ability to capture the heat distributions in three dimensions. The availability of the near-surface air temperature solves the problems of limited numbers and footprints of ground-based observations in the urban area for atmospheric UHI research. The accuracy from comparing with ground observations shows a fairly good result in most cases.

The near-surface air temperatures derived from the profiles are more likely to be the top of the UCL temperature. Oke (1976) discussed two different concepts regarding UCL and UBL UHIs. UCL describes the climate features impacted by the urban roughness elements at a microscale, while the urban boundary layer is dominated by urban area and its lower boundary at a local or

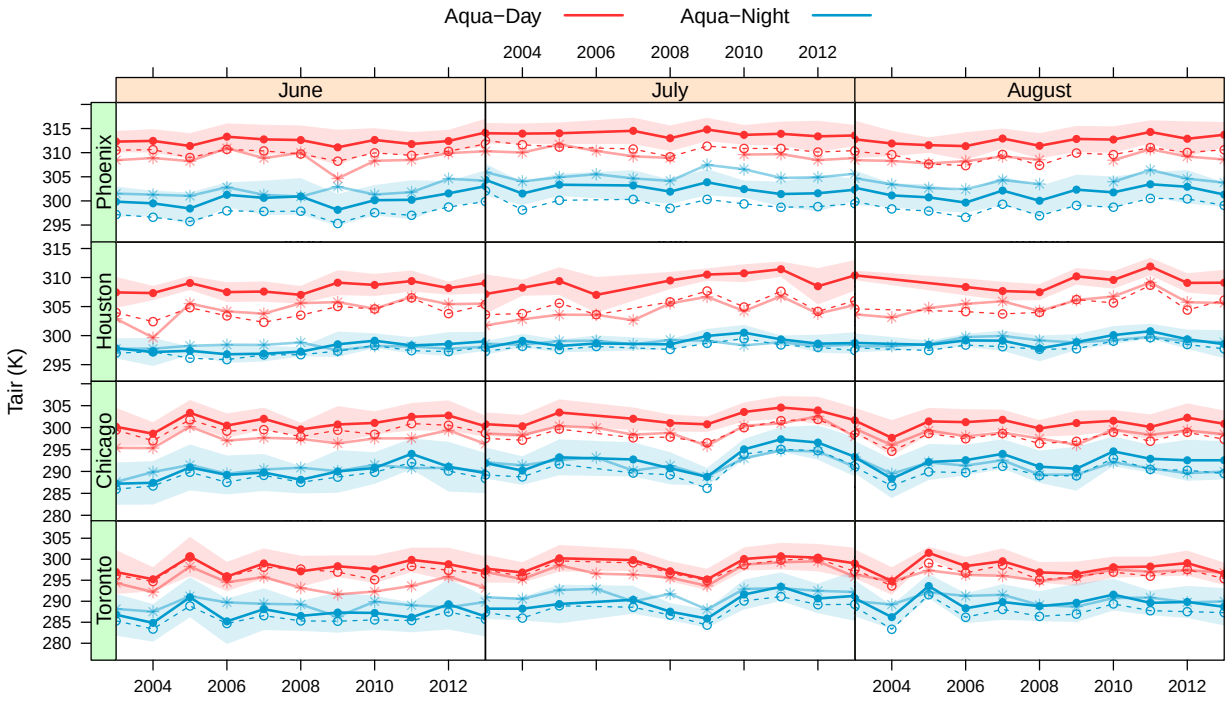

Figure 4.8: The monthly 11-year UHI dynamics for four cities during Aqua overpass periods. The red lines are daytime temperatures while the blue lines indicate the nighttime temperatures. The dark solid line with filled circles and the shaded area represent the mean $\pm$ one standard deviation of MODIS air temperatures for the pixels with more than 60% urban fraction and no water fraction. The dark dashed line with empty circles is the mean pure-vegetation temperature. The light solid line with stars represents averaged temperature from the ground observations around noon/midnight.

mesoscale. The signal sensed from the urban surface includes roof, wall, and ground depending on the view angles. Further, the retrieval of the near-surface temperature is determined by the mean elevation within a 5 km pixel. The height representing the MODIS air temperature at 5 km resolution may diminish the influence of building/canopy height variations and enhance the terrain impact at this scale. Fortunately, most cities are located in flat terrain, so the estimated height is more likely to be in the top or above of UCL in general. In more mountainous regions, in addition to the land-cover forcing, the terrain impacts may introduce more complicating factors that influence the temperature.

The MOD07_L2 is derived from the integrated information of cloud-free instantaneous field-of-views (IFOVs) at 1 km within 5×5 km area. Therefore, sunny areas may lead to more reliable estimations. Urban areas tend to be more cloudy in general (Rabin and Martin, 1996). Fig.S3 shows the number of clear sky pixels for satellite overpass during the study period, suggesting more cloudy summers in the Houston area compared to the other three cities. One reason for more clouds over the urban areas is that the deep convection happens in the afternoon enhancing the chance of clouds (Angevine et al., 2003). Also, anthropogenic emissions provide additional sources of cloud condensation nuclei. The frequent presence of clouds over the Greater Houston area, potentially decreases the number of cloud-free IFOVs at the 5 km scale. This may explain the relatively low correlation coefficients and large variations of slopes of linear regressions between the MODIS estimations and ground observations. Similarly, the sky conditions of the ground observations may not represent the clear-sky pixels of MODIS. More precise experiments may be needed to further evaluate the MOD07_L2-based air temperature accuracy over very cloudy cities.

The diurnal UHI patterns illustrated in Fig. 4.2 and Fig. 4.7 for some cities are slightly different from the features of atmospheric UHI and surface UHI. The atmospheric UHI effects are usually found under calm and clear nighttimes (Voogt and Oke, 2003), which is related to the different heating/cooling rates over urban and rural surfaces (Oke, 1982). The SUHIs usually exhibit stronger and larger spatial variability during the daytime (Roth et al., 1989; Hung et al., 2006; Hu and Brunsell, 2013). Fig. 4.9 gives a broad idea of the diurnal cycle of atmospheric UHI for each

city based on the ground observations over the land area. However, we should realize that the ground measurements at the "urban" and "rural" sites only illustrate one possible UHI intensity, which may be representative for one point on the UHIC. Houston shows an underestimated atmospheric UHI from nighttime MODIS, which may be explained by some limited ability of MODIS for detecting in humid environments as well as by increasing uncertainty with the presence of large amounts of clouds. For most cases, daytime UHI are slightly enhanced compared to nighttime for the atmospheric UHI. One of the reasons is the regression statistics algorithm is based on the signals detected from a narrow solid angle of view from the sensor at different zenith view angles ranging from - 65° to + 65°. The observed surface components impact the representativeness of the near-surface temperatures. Also, the near-surface temperature from MODIS represents a higher height rather than screen level.

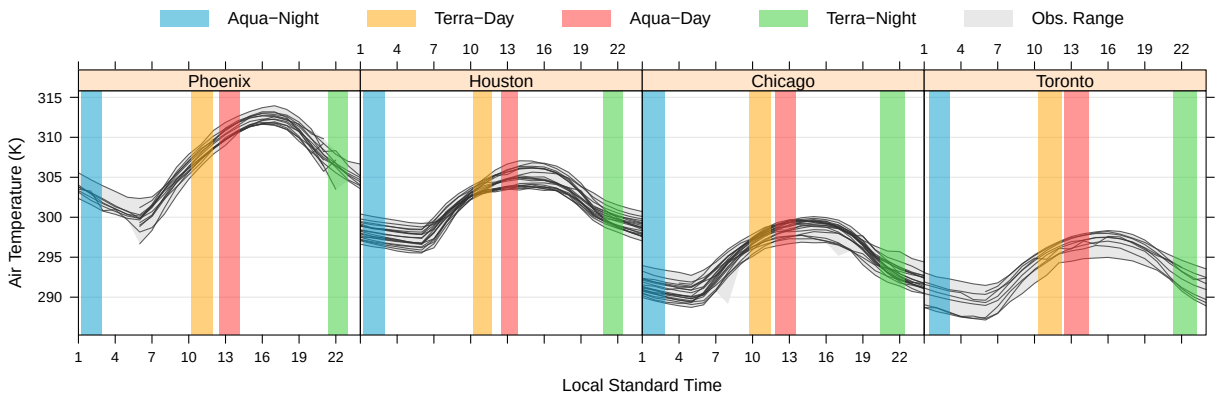

Figure 4.9: The mean diurnal cycles of each site (black lines) over the urban/rural areas shown as empty circles in Fig. 4.2. The gray shaded area indicates the temperature differences among these sites. Four satellite overpass periods are shaded in four colors.

The MODIS atmosphere product could not avoid some issues which are limited by the nature of remote sensing techniques. For example, the sensor view angle impacts the land surface temperature in the MODIS products (Hu et al., 2014) even when the retrieval algorithm considers the view angle influences. Moreover, thermal anisotropy widely exists in the urban surface. These issues have not been addressed in this study, but need to be considered for studies where higher accuracy is required.

When concerning human health and living environments in the urban area, the air tempera-

tures are potentially better sources compared with the LST. The research for SUHI spatiotemporal dynamics and the techniques for spatial/temporal scaling can also apply to air temperature. Furthermore, the overpass time of Aqua-Day is closest to the time of the maximum air temperature. With the availability of both air and dew-point temperatures, MODIS can be an invaluable source to conduct heat stress studies. However, time-based corrections of MODIS estimated near-surface temperatures may need to be applied using the diurnal temperature patten from other high temporal-frequency data, such as in-situ observations. Moreover, the time variation should be considered based on the day to day corrections.

Compared to the common UHI indicators in the literature (Schwarz et al., 2011), the UHIC has many advantages. 1) UHIC integrates the urban surface heterogeneity, which also avoids the biases caused by urban/rural divisions. 2) UHIC can capture the urban surface features; consequently, each city has a unique UHIC. 3) UHIC can be constructed for different temporal scales, such as annual, seasonal, and diurnal scales. 4) UHIC is universal and easy to use for comparisons across time and space. 5) UHIC is less influenced by the bias of the data source, due to the reliance on the gradients rather than absolute values of temperatures.

There are some caveats for the applications of UHIC. The urban fractions integrate many inexplicit factors. For example, the urban fraction is highly correlated to the major urban land use types. The different local climate zones (Stewart and Oke, 2012) with similar urban fraction but a quite large variety of building configuration and terrain roughness may diverge from the temperature distributions. For such situations, UHIC only shows the integrated results. A particular region is likely to contain only a few local climate zones, because the urban features usually are highly correlated due to the close geolocations, similar climate, shared cultural and economic settings. The UHIC should be interpreted city by city among different regions. The non-urban fraction, such as a water bodies, dense vegetation and barren soil, also plays a critical role in the air temperature over the urban area. Other possible solutions include using impervious surface area or other parameters that could distinguish urban features heavily impacting the temperature instead of the urban fraction.

The urban fraction is a relative concept according to the source resolution to distinguish the urban surfaces and target scale to calculate the fraction. In this study, we employed the urban pixels at 500 m for UHIC, which is defined by the dominant built areas larger than 50% in the 500 m pixel and the contiguous patches of urban environment larger than 1 km^2 (Schneider et al., 2009). The urban build-up area within each pixel varies widely around the world and is influenced by many social and climatic factors (Friedl et al., 2010). The higher resolution of land cover data will naturally decrease the non-urban fraction mixed in the upscaled pixel level. The proper ratio of resolutions for the upscaling and statistics should be determined by the quantifying interval of the urban fraction, such as 5% in this study, and the accuracy requirement.

UHIC under clear-sky conditions can be applied to different temporal scales but is sensitive to the time of day (Fig. 4.7). In order to guarantee sufficient sample size, monthly or seasonal UHICs are preferred for relatively longer observations for the cloudy areas. Finally, the UHIC is not a single-value UHI indicator, but it helps easily estimate different indicators if necessary.

4.6 Conclusions

By estimating the near-surface air and dew-point temperatures from the MODIS atmospheric profiles product (MOD07_L2), this is the first study that exploits the ability of MODIS to capture the temporal dynamics, and spatial structures (horizontal and vertical) of atmospheric UHI for four mega cities in North America during 2003-2013 summers. In addition, this study develops an UHI curve to represent UHI intensity by integrating the urban surface heterogeneity in a curve, showing the relationship between the air temperature and the urban fractions.

MODIS atmospheric profile data are a invaluable source to capture the urban thermal distributions in horizontal (5 km), vertical (20 pressure levels) and temporal (4 times a day) dimensions. The MODIS near-surface temperature represents an integrated result in a 5 km grid, including urban morphology, surface material heterogeneity, terrain, solar angle, and sensor view angle. The comparison between the MODIS near-surface temperature and the ground observations suggests

an accuracy of 3-7 K RMSE for different cities and times of day. In general, very dry and moist climate conditions increase the variability of the MODIS temperature accuracy. Although the magnitude seems relatively high, it can be reduced by correcting for the total biases.

The MODIS air temperature provides a less expensive way to conduct UHI research, which is able to capture the fine-scale gradients over the complex urban areas due to the high spatial resolution. UHIC provides a new way to quantify the UHI city by city, which emphasize the temperature gradients for different urban fractions, consequently decreasing the impact of the data biases.

This study evaluates the performance of MODIS air and dew-point temperatures during summer months. Further evaluations will be worthwhile for other seasons, as well as for other cities in different regions under various climatic conditions. Moreover, this study presents the original MODIS temperature and its application for UHIC under basic quality controls and does not discuss any correction method in detail or use corrected results. Simple linear regression between the MODIS data and observations, possibly, is the easiest way to correct the primary bias. Systematic research may be required to limit the bias and to control the uncertainty for other applications that depend on the absolute magnitude of air and dew-point temperatures.

Chapter 5

Conclusions

5.1 Summary of Findings

Remote sensing techniques have become popular to assess the urban heat island. However, the remotely sensed temperature for UHI faces several unique problems and challenges, which need to distinguish from the traditional in-situ/traverse measurements and urban climate model simulations.

This dissertation research has addressed several important issues about using remote sensing to conduct urban heat islands studies. The nature of thermal remote sensing techniques prevents detecting the signals under clouds. Using the temporally composited data is a common solution to avoid the missing data. Chapter 2 of this dissertation addresses the question about the impact of temporal aggregation of remote sensing data on UHI studies and the main causes of the bias. Chapter 2 investigates a long-term urban heat island dynamics using daily, 2-, 4-, 8-, 16- and 32-day composite LST over the Houston area. Several conclusions are drawn from the statistical comparison:

1. The temporal aggregation impact has seasonality and is also a function of composite scale. The seasonal pattern shows that the summer daytime SUHI has the largest magnitude and variation, while the nighttime SUHI magnitudes are much smaller and less variable. The

composite scale is particularly important during the summer daytime. The higher the aggregation scale is, the higher SUHI biases are generated. However, the impact from the aggregation scales and seasonality for nighttime is comparably small.

2. The temporal aggregation errors vary spatially, which is related to the land cover types.

3. The primary reason for the errors from temporal aggregation is heterogeneously distributed clouds, showing a higher frequency of clouds over the urban areas and leading to a bias of LST towards warmer daytime conditions.

The second part of this research was based on the fact that several important aspects of satellite LST data can easily be neglected by modelers for model validation, such as cloud distribution and sensor view angle. The motivating question for Chapter 3 was "How can we use MODIS land surface temperature to validate long-term urban model simulations?" This research consisted of a 10-year case study over Houston during 2003-2012 and three sampling strategies to minimize the confounding factors of clouds are proposed and applied to compare MODIS LST with HRLDAS-simulated T_{rad}, temporally and spatially. The assumptions made by each of the strategies were discussed. We assessed the strengths and weakness of the three sampling methods and suggested their best applications:

1. The satellite cloud mask (SCM) method: prior to comparison, the cloud mask for each MODIS scene is applied to its concurrent HRLDAS simulation. The SCM method gives the best statistical climatological comparison conditioned on the assumed agreement between MODIS clouds and forcing clouds.

2. The max/min temperature (MMT) method: the 50 warmest days and coolest nights for each dataset are selected and compared to avoid cloud impacts, which is best for comparison at the extremes.

3. The high clear-sky fraction (HCF) method: only those MODIS scenes that have a high percentage of clear-sky pixels are sampled and compared, which gives the best absolute tem-

perature comparison due to the spatial and temporal consistency between simulations and observations

The third part of the research (Chapter 4) extended the applications of MODIS products to capture the atmospheric UHI instead of the SUHI. To understand the ability and accuracy of the MODIS atmospheric profile-based near-surface temperature and to solve the current problem of describing UHI from spatial coverages, four mega cities in North America during 2003-2013 summers were evaluated using ground observations. In addition, this study developed an UHI curve to represent UHI intensity by integrating the urban surface heterogeneity in a curve, showing the relationship between the air temperature and the urban fractions. The conclusions drawn from this part were:

1. The comparison between the MODIS near-surface temperature and the ground observations suggests an accuracy of 3-7 K RMSE for different cities and times of day. In general, very dry and moist climate conditions increase the variability of the MODIS temperature accuracy.

2. The MODIS air temperature provides a less expensive way to conduct UHI research, which is able to capture the fine-scale gradients over the complex urban areas due to the high spatial resolution.

3. UHIC is a new way to quantify the UHI city by city, which emphasize the temperature gradients for different urban fractions, consequently decreasing the impact of the data biases. Different kinds of UHI indicators can be easily obtained from UHIC if necessary, such as the inter-urban, and urban-vegetation UHI intensity.

5.2 Summary of Contributions

UHI and extreme heat events in cities are regarded as one of the leading causes of weather-related human mortality in the United States and in many countries worldwide. Understanding and further prediction of UHI intensity and its related weather phenomena are direct needs for policy and

decision-making. By addressing the questions, this study extended the understanding of the spatial and temporal distributions of UHI in a long-term period under different weather conditions through remote sensing data. The research not only showed the temporal dynamics and spatial patterns of UHI in the last ten years, but it also explored the potential for remote sensing data to detect UHI effects. By comparing the performances of high-resolution models for long-term or short term periods through remote sensing data, it is possible to evaluate the accuracy of simulations and to put up suggestions to improve predictions for future heat events.

This dissertation contributes the literatures of urban heat island and urban climatology studies in several aspects:

- A comprehensive evaluation for the impact of clouds on composite LST data. This study provides an overall bias of UHI for using composite data over cloudy area.
- Three practical sampling methods to validate long-term urban climate simulations by using satellite data. These sampling methods considered the different features of modeling and bird's-eye view satellite observations, which will be best application for various validation purposes.
- A new way to quantify UHI from remotely sensed temperature data. UHIC integrates the impact of urban fraction on the air temperature in the curve, showing the unique features of urban surface heterogeneity.
- An introduction of new satellite data source for atmospheric UHI studies. MODIS temperature and moisture profiles provide invaluable long-term information for the UHI and heat stress estimations with a high spatial resolution.

To sum up, the dissertation research addressed different aspects of remotely sensed UHI research, including the problems required to be aware of, the approaches that are practical to be used, and potential datasets needed more attentions. This study expects to help widen and broaden applications of remote sensing to understand the UHI climatology, and to improve the accuracy of UHI quantification from a new perspective.

5.3 Recommendations for Future Work

The view angle problems

Voogt and Oke (1997) came up with a concept of complete urban surface temperature and discussed the anisotropy of urban surface. Then, there were several research groups discussing the directional anisotropic thermal properties over the urban area. For example, Lagouarde et al. (2010, 2012) addressed the urban thermal anisotropy features for daytime and nighttime through the airborne cameras. Voogt (2008) tested the sensor view model over the light-industrial and downtown area in Vancouver, concluding that the total anisotropy is significantly impacted by the surface structure and microscale temperature variability. However, the research was based on higher resolution data, which decreases the urban heterogeneity at the pixel level. For coarser resolution data from satellite to detect the temperature over large cities, the situations became more complex. Chapter 3 of this dissertation found the major view angle impacts from MODIS LST product come from the inadequate atmosphere corrections instead of urban surfaces. To better quantify the UHI magnitude, the view angle effects from the atmosphere and urban surfaces should be separated first. Further corrections for the atmosphere effects due to different view path lengths are required, and then the anisotropic surface properties should be considered.

Temperatures estimated from MODIS atmospheric profile product

In general, the root-mean-square-error (RMSE) of MODIS profiles is about 1 K higher than AIRS profiles through the Atmospheric Radiation Measurement (ARM) Program Cloud and Radiation Test Bed (CART) (Seemann et al., 2006). The evaluations in Brazil (de Souza et al., 2007) and the Korean Peninsula (Kim et al., 2004) showed better results. Seemann et al. (2003) concluded that MODIS profiles agree well with the radiosonde under fairly monotonic smooth temperature and moisture distributions. Other assessments of MODIS data were conducted for the total precipitable water or total column ozone that is yielded from the temperature/moisture profiles (Seemann et al., 2003; King et al., 2003; Borbas et al., 2011). Although the absolute error or bias exists in the dataset, the accuracy under different regions and climate states should be addressed considering the great potential for applications. In addition to the bias from the product retrieval algorithm,

other atmospheric conditions also contribute to the accuracy of the atmospheric profiles. The results shows a relatively unstable estimations under very dry and moist conditions, which require more comprehensive evaluations. If the corrections is based on ground observations, the site condition (height, environment setting, etc.), observation time, and atmospheric conditions should be considered.

Applications of MODIS air and dew-point temperatures

The relatively high resolution temperature data derived from satellite observations will be useful after the necessary error corrections. First, urban heat stress needs both temperature and moisture information. The MODIS profiles provide the information to estimate heat stress index with a relative high spatial/temporal dynamics over global urban areas. This valuable information benefits the heat-related health studies, and the research of impacts from the urbanization, global changes and extreme events. Second, to understand urban climatology, temperature and moisture information is the key to estimate the energy budget. Third, for the urban climate modeling, the data may provide valuable information for model validations, due to the comparable scale, global coverage, and independence from modeling, consistency with other surface parameters derived from satellite observations.

UHIC and its applications

The UHICs of cities in different climate zones during each season can extend our understanding of the UHI pattens at a global scale. The impact of urbanization on the UHI dynamics are also interesting to be compared through UHIC. Besides the urban fractions, other parameters that could distinguish urban features that significantly influence urban temperatures can be useful for UHIC, such as impervious surface area and population density. How different are UHICs and what is the most important information revealed from these UHICs should be address with and an extension of this research.

References

Alchapar, N. L., Correa, E. N., Cantón, M. A., 2014. Classification of building materials used in the urban envelopes according to their capacity for mitigation of the urban heat island in semiarid zones. Energy and Buildings 69 (0), 22–32.

Angevine, W. M., White, A. B., Senff, C. J., Trainer, M., Banta, R. M., Ayoub, M. A., 2003. Urban-rural contrasts in mixing height and cloudiness over nashville in 1999. Journal of Geophysical Research-Atmospheres 108 (D3).

Aumann, H. H., Chahine, M. T., Gautier, C., Goldberg, M. D., Kalnay, E., McMillin, L. M., Revercomb, H., Rosenkranz, P. W., Smith, W. L., Staelin, D. H., Strow, L. L., Susskind, J., 2003. Airs/amsu/hsb on the aqua mission: design, science objectives, data products, and processing systems. Geoscience and Remote Sensing, IEEE Transactions on 41 (2), 253–264.

Barlow, J. F., Dunbar, T. M., Nemitz, E. G., Wood, C. R., Gallagher, M. W., Davies, F., O'Connor, E., Harrison, R. M., 2011. Boundary layer dynamics over london, uk, as observed using doppler lidar during repartee-ii. Atmos. Chem. Phys. 11 (5), 2111–2125.

BenDor, E., Saaroni, H., 1997. Airborne video thermal radiometry as a tool for monitoring microscale structures of the urban heat island. International Journal of Remote Sensing 18 (14), 3039–3053.

Betts, A. K., Desjardins, R. L., Worth, D., 2007. Impact of agriculture, forest and cloud feedback on the surface energy budget in boreas. Agricultural and Forest Meteorology 142 (2-4), 156–169.

Bisht, G., Bras, R. L., 2010. Estimation of net radiation from the modis data under all sky conditions: Southern great plains case study. Remote Sensing of Environment 114 (7), 1522–1534.

Bisht, G., Venturini, V., Islam, S., Jiang, L., 2005. Estimation of the net radiation using modis (moderate resolution imaging spectroradiometer) data for clear sky days. Remote Sensing of Environment 97 (1), 52–67.

Bodas-Salcedo, A., Ringer, M. A., Jones, A., 2008. Evaluation of the surface radiation budget in the atmospheric component of the hadley centre global environmental model (hadgem1). Journal of Climate 21 (18), 4723–4748.

Borbas, E., Seemann, S. W., Kern, A., Moy, L., Li, J., Gumley, L., Menzel, W. P., 2011. Modis atmospheric profile retrieval algorithm theoretical basis document, collection 6. Tech. rep., University of Wisconsin-Madison.

Burian, S. J., Ching, J. K., 2009. Development of gridded fields of urban canopy parameters for advanced urban meteorological and air quality models. Tech. rep.

Burian, S. J., Shepherd, J. M., 2005. Effect of urbanization on the diurnal rainfall pattern in houston. Hydrological Processes 19 (5), 1089–1103.

Chen, F., Dudhia, J., 2001. Coupling an advanced land surface-hydrology model with the penn state-ncar mm5 modeling system. part i: Model implementation and sensitivity. Monthly Weather Review 129 (4), 569–585.

Chen, F., Kusaka, H., Bornstein, R., Ching, J., Grimmond, C. S. B., Grossman-Clarke, S., Loridan, T., Manning, K. W., Martilli, A., Miao, S. G., Sailor, D., Salamanca, F. P., Taha, H., Tewari, M., Wang, X. M., Wyszogrodzki, A. A., Zhang, C. L., 2011. The integrated wrf/urban modelling system: development, evaluation, and applications to urban environmental problems. International Journal of Climatology 31 (2), 273–288.

Chen, F., Manning, K. W., LeMone, M. A., Trier, S. B., Alfieri, J. G., Roberts, R., Tewari, M., Niyogi, D., Horst, T. W., Oncley, S. P., Basara, J. B., Blanken, P. D., 2007. Description and evaluation of the characteristics of the ncar high-resolution land data assimilation system. Journal of Applied Meteorology and Climatology 46 (6), 694–713.

Chen, X. L., Zhao, H. M., Li, P. X., Yin, Z. Y., 2006. Remote sensing image-based analysis of the relationship between urban heat island and land use/cover changes. Remote Sensing of Environment 104 (2), 133–146.

Ching, J., Brown, M., Burian, S., Chen, F., Cionco, R., Hanna, A., Hultgren, T., McPherson, T., Sailor, D., Taha, H., Williams, D., 2009. National urban database and access portal tool. Bulletin of the American Meteorological Society 90 (8), 1157–1168.

Chow, W. T. L., Brennan, D., Brazel, A. J., 2011. Urban heat island research in phoenix, arizona: Theoretical contributions and policy applications. Bulletin of the American Meteorological Society 93 (4), 517–530.

Coseo, P., Larsen, L., 2014. How factors of land use/land cover, building configuration, and adjacent heat sources and sinks explain urban heat islands in chicago. Landscape and Urban Planning 125 (0), 117–129.

Cosgrove, B. A., Lohmann, D., Mitchell, K. E., Houser, P. R., Wood, E. F., Schaake, J. C., Robock, A., Marshall, C., Sheffield, J., Duan, Q. Y., Luo, L. F., Higgins, R. W., Pinker, R. T., Tarpley, J. D., Meng, J., 2003. Real-time and retrospective forcing in the north american land data assimilation system (nldas) project. Journal of Geophysical Research-Atmospheres 108 (D22).

Dai, A., Trenberth, K. E., Karl, T. R., 1999. Effects of clouds, soil moisture, precipitation, and water vapor on diurnal temperature range. Journal of Climate 12 (8), 2451–2473.

de Souza, R. A. F., Rodrigues, J. V., Ceballos, J. C., 2007. Performance of the airs/amsu and modis soundings over natal/brazil using collocated sondes: Shadoz campaign 2004-2005. pp. 644–647.

Diem, J. E., Brown, D. P., 2003. Anthropogenic impacts on summer precipitation in central arizona, usa. Professional Geographer 55 (3), 343–355.

Dousset, B., Gourmelon, F., 2003. Satellite multi-sensor data analysis of urban surface temperatures and landcover. Isprs Journal of Photogrammetry and Remote Sensing 58 (1-2), 43–54.

Friedl, M. A., Sulla-Menashe, D., Tan, B., Schneider, A., Ramankutty, N., Sibley, A., Huang, X. M., 2010. Modis collection 5 global land cover: Algorithm refinements and characterization of new datasets. Remote Sensing of Environment 114 (1), 168–182.

Fry, J., Xian, G., Jin, S., Dewitz, J., Homer, C., Yang, L., Barnes, C., Herold, N., Wickham, J., 2011. Completion of the 2006 national land cover database for the conterminous united states. Photogrammetric Engineering and Remote Sensing 77 (9), 858–864.

Gaffin, S. R., Rosenzweig, C., Khanbilvardi, R., Parshall, L., Mahani, S., Glickman, H., Goldberg, R., Blake, R., Slosberg, R. B., Hillel, D., 2008. Variations in new york city's urban heat island strength over time and space. Theoretical and Applied Climatology 94 (1-2), 1–11.

Gallo, K., McNab, A., Karl, T., Brown, J., Hood, J., Tarpley, J., 1993. The use of noaa avhrr data for assessment of the urban heat island effect. Center for Advanced Land Management Information Technologies–Publications, 1.

Gallo, K. P., Owen, T. W., 1999. Satellite-based adjustments for the urban heat island temperature bias. Journal of Applied Meteorology 38 (6), 806–813.

Gallo, K. P., Tarpley, J. D., Mcnab, A. L., Karl, T. R., 1995. Assessment of urban heat islands - a satellite perspective. Atmospheric Research 37 (1-3), 37–43.

Ghent, D., Kaduk, J., Remedios, J., Ardo, J., Balzter, H., 2010. Assimilation of land surface temperature into the land surface model jules with an ensemble kalman filter. Journal of Geophysical Research-Atmospheres 115.

Grimmond, C. S. B., 2006. Progress in measuring and observing the urban atmosphere. Theoretical and Applied Climatology 84 (1-3), 3–22.

Grimmond, C. S. B., Blackett, M., Best, M. J., Barlow, J., Baik, J. J., Belcher, S. E., Bohnenstengel, S. I., Calmet, I., Chen, F., Dandou, A., Fortuniak, K., Gouvea, M. L., Hamdi, R., Hendry, M., Kawai, T., Kawamoto, Y., Kondo, H., Krayenhoff, E. S., Lee, S. H., Loridan, T., Martilli, A., Masson, V., Miao, S., Oleson, K., Pigeon, G., Porson, A., Ryu, Y. H., Salamanca, F., Shashua-Bar, L., Steeneveld, G. J., Tombrou, M., Voogt, J., Young, D., Zhang, N., 2010. The international urban energy balance models comparison project: First results from phase 1. Journal of Applied Meteorology and Climatology 49 (6), 1268–1292.

Grimmond, C. S. B., Oke, T. R., 2002. Turbulent heat fluxes in urban areas: Observations and a local-scale urban meteorological parameterization scheme (lumps). Journal of Applied Meteorology 41 (7), 792–810.

Henry, J. A., Dicks, S. E., Wetterqvist, O. F., Roguski, S. J., 1989. Comparison of satellite, ground-based, and modeling techniques for analyzing the urban heat-island. Photogrammetric Engineering and Remote Sensing 55 (1), 69–76.

Holben, B. N., 1986. Characteristics of maximum-value composite images from temporal avhrr data. International Journal of Remote Sensing 7 (11), 1417–1434.

Homer, C., Huang, C. Q., Yang, L. M., Wylie, B., Coan, M., 2004. Development of a 2001 national land-cover database for the united states. Photogrammetric Engineering and Remote Sensing 70 (7), 829–840.

Hu, L., Brunsell, N. A., 2013. The impact of temporal aggregation of land surface temperature data for surface urban heat island (suhi) monitoring. Remote Sensing of Environment 134, 162–174.

Hu, L., Brunsell, N. A., Monaghan, A. J., Barlage, M., Wilhelmi, O. V., 2014. How can we use modis land surface temperature to validate long-term urban model simulations? Journal of Geophysical Research: Atmospheres 119 (6), 3185–3201.

Hung, T., Uchihama, D., Ochi, S., Yasuoka, Y., 2006. Assessment with satellite data of the urban heat island effects in asian mega cities. International Journal of Applied Earth Observation and Geoinformation 8 (1), 34–48.

Imhoff, M. L., Zhang, P., Wolfe, R. E., Bounoua, L., 2010. Remote sensing of the urban heat island effect across biomes in the continental usa. Remote Sensing of Environment 114 (3), 504–513.

Jin, M., Shepherd, J. M., 2005. Inclusion of urban landscape in a climate model - how can satellite data help? Bulletin of the American Meteorological Society 86 (5), 681–689.

Jin, M. L., Dickinson, R. E., 2010. Land surface skin temperature climatology: benefitting from the strengths of satellite observations. Environmental Research Letters 5 (4).

Jin, M. L., Dickinson, R. E., Vogelmann, A. M., 1997. A comparison of ccm2-bats skin temperature and surface-air temperature with satellite and surface observations. Journal of Climate 10 (7), 1505–1524.

Jin, M. L., Shepherd, J. M., King, M. D., 2005. Urban aerosols and their variations with clouds and rainfall: A case study for new york and houston. Journal of Geophysical Research-Atmospheres 110 (D10).

Kalkstein, L. S., Greene, J. S., 1997. An evaluation of climate/mortality relationships in large us cities and the possible impacts of a climate change. Environmental Health Perspectives 105 (1), 84–93.

Kato, S., Yamaguchi, Y., 2005. Analysis of urban heat-island effect using aster and etm+ data: Separation of anthropogenic heat discharge and natural heat radiation from sensible heat flux. Remote Sensing of Environment 99 (1-2), 44–54.

Kidd, C., Levizzani, V., Bauer, P., 2009. A review of satellite meteorology and climatology at the start of the twenty-first century. Progress in Physical Geography 33 (4), 474–489.

Kim, D. Y., Han, K. S., 2013. Remotely sensed retrieval of midday air temperature considering atmospheric and surface moisture conditions. International Journal of Remote Sensing 34 (1), 247–263.

Kim, J. Y., Hogue, T. S., 2008. Evaluation of a modis-based potential evapotranspiration product at the point scale. Journal of Hydrometeorology 9 (3), 444–460.

Kim, Y., Kwon, B., Hong, K., 2004. Vertical temperature and moisture structure in lower atmosphere retrived from terra/modis. Gayana (Concepción) 68 (2), 319–323.

King, M. D., Menzel, W. P., Kaufman, Y. J., Tanre, D., Bo-Cai, G., Platnick, S., Ackerman, S. A., Remer, L. A., Pincus, R., Hubanks, P. A., 2003. Cloud and aerosol properties, precipitable water, and profiles of temperature and water vapor from modis. Geoscience and Remote Sensing, IEEE Transactions on 41 (2), 442–458.

Kusaka, H., Kimura, F., 2004. Coupling a single-layer urban canopy model with a simple atmospheric model: Impact on urban heat island simulation for an idealized case. Journal of the Meteorological Society of Japan 82 (1), 67–80.

Kusaka, H., Kondo, H., Kikegawa, Y., Kimura, F., 2001. A simple single-layer urban canopy model for atmospheric models: Comparison with multi-layer and slab models. Boundary-Layer Meteorology 101 (3), 329–358.

Lagouarde, J. P., Henon, A., Irvine, M., Voogt, J., Pigeon, G., Moreau, P., Masson, V., Mestayer, P., 2012. Experimental characterization and modelling of the nighttime directional anisotropy of thermal infrared measurements over an urban area: Case study of toulouse (france). Remote Sensing of Environment 117, 19–33.

Lagouarde, J. P., Henon, A., Kurz, B., Moreau, P., Irvine, M., Voogt, J., Mestayer, P., 2010. Modelling daytime thermal infrared directional anisotropy over toulouse city centre. Remote Sensing of Environment 114 (1), 87–105.

Lagouarde, J. P., Moreau, P., Irvine, M., Bonnefond, J. M., Voogt, J. A., Solliec, F., 2004. Airborne experimental measurements of the angular variations in surface temperature over urban areas: case study of marseille (france). Remote Sensing of Environment 93 (4), 443–462.

Leroyer, S., Belair, S., Mailhot, J., 2011. Microscale numerical prediction over montreal with the canadian external urban modeling system. Journal of Applied Meteorology and Climatology 50 (12), 2410–2428.

Lo, C. P., Quattrochi, D. A., Luvall, J. C., 1997. Application of high-resolution thermal infrared remote sensing and gis to assess the urban heat island effect. International Journal of Remote Sensing 18 (2), 287–304.

Los, S. O., Justice, C. O., Tucker, C. J., 1994. A global 1-degrees-by-1-degrees ndvi data set for climate studies derived from the gimms continental ndvi data. International Journal of Remote Sensing 15 (17), 3493–3518.

Mage, D., Ozolins, G., Peterson, P., Webster, A., Orthofer, R., Vandeweerd, V., Gwynne, M., 1996. Urban air pollution in megacities of the world. Atmospheric Environment 30 (5), 681–686.

Masson, V., 2006. Urban surface modeling and the meso-scale impact of cities. Theoretical and Applied Climatology 84 (1-3), 35–45.

Matson, M., Mcclain, E. P., Mcginnis, D. F., Pritchard, J. A., 1978. Satellite detection of urban heat islands. Monthly Weather Review 106 (12), 1725–1734.

Menzel, W. P., Purdom, J. F. W., 1996. Introducing goes-1: The first of a new generation of geo-stationary operational environmental satellites .1. the satellite sensor systems, quality control procedures for converting data into products. Earth Observation and Remote Sensing 14 (1), 81–99.

Mestayer, P. G., Durand, P., Augustin, P., Bastin, S., Bonnefond, J. M., Benech, B., Campistron, B., Coppalle, A., Delbarre, H., Dousset, B., Drobinski, P., Druilhet, A., Frejafon, E., Grimmond,

C. S. B., Groleau, D., Irvine, M., Kergomard, C., Kermadi, S., Lagouarde, J. P., Lemonsu, A., Lohou, F., Long, N., Masson, V., Moppert, C., Noilhan, J., Offerle, B., Oke, T. R., Pigeon, G., Puygrenier, V., Roberts, S., Rosant, J. M., Said, F., Salmond, J., Talbaut, M., Voogt, J., 2005. The urban boundary-layer field campaign in marseille (ubl/clu-escompte): Set-up and first results. Boundary-Layer Meteorology 114 (2), 315–365.

Miao, S. G., Chen, F., Lemone, M. A., Tewari, M., Li, Q. C., Wang, Y. C., 2009. An observational and modeling study of characteristics of urban heat island and boundary layer structures in beijing. Journal of Applied Meteorology and Climatology 48 (3), 484–501.

Mildrexler, D. J., Zhao, M. S., Running, S. W., 2011. A global comparison between station air temperatures and modis land surface temperatures reveals the cooling role of forests. Journal of Geophysical Research-Biogeosciences 116.

Monaghan, A. J., Hu, L., Brunsell, N. A., Barlage, M., Wilhelmi, O. V., 2014. Evaluating the impact of urban morphology configurations on the accuracy of urban canopy model temperature simulations with modis. Journal of Geophysical Research: Atmospheres 119.

Moody, A., Strahler, A. H., 1994. Characteristics of composited avhrr data and problems in their classification. International Journal of Remote Sensing 15 (17), 3473–3491.

Morris, C., Simmonds, I., Plummer, N., 2001. Quantification of the influences of wind and cloud on the nocturnal urban heat island of a large city. Journal of Applied Meteorology 40 (2), 169–182.

Mu, Q., Heinsch, F. A., Zhao, M., Running, S. W., 2007. Development of a global evapotranspiration algorithm based on modis and global meteorology data. Remote Sensing of Environment 111 (4), 519–536.

National Research Council, ., 2012. Urban Meteorology: Forecasting, Monitoring, and Meeting Users' Needs. The National Academies Press, Washington, DC.

NOAA National Ocean Service, ., 2013. National coastal population report, population trends from 1970 to 2020. Tech. rep., National Oceanic and Atmospheric Administration, Department of Commerce.

Norman, J. M., Divakarla, M., Goel, N. S., 1995. Algorithms for extracting information from remote thermal-ir observations of the earths surface. Remote Sensing of Environment 51 (1), 157–168.

Offerle, B., Eliasson, I., Grimmond, C. S. B., Holmer, B., 2007. Surface heating in relation to air temperature, wind and turbulence in an urban street canyon. Boundary-Layer Meteorology 122 (2), 273–292.

Oke, T., 2007. Siting and exposure of meteorological instruments at urban sites. In: Borrego, C., Norman, A.-L. (Eds.), Air Pollution Modeling and Its Application XVII. Springer US, pp. 615–631.

Oke, T. R., 1973. City size and the urban heat island. Atmospheric Environment (1967) 7 (8), 769–779.

Oke, T. R., 1976. The distinction between canopy and boundary-layer urban heat islands. Atmosphere 14 (4), 268–277.

Oke, T. R., 1982. The energetic basis of the urban heat-island. Quarterly Journal of the Royal Meteorological Society 108 (455), 1–24.

Oke, T. R., 1995. The heat island of the urban boundary layer: Characteristics, causes and effects. In: Cermak, J., Davenport, A., Plate, E., Viegas, D. (Eds.), Wind Climate in Cities. Vol. 277 of NATO ASI Series. Springer Netherlands, pp. 81–107.

Oleson, K. W., Bonan, G. B., Feddema, J., Vertenstein, M., Grimmond, C. S. B., 2008. An urban parameterization for a global climate model. part i: Formulation and evaluation for two cities. Journal of Applied Meteorology and Climatology 47 (4), 1038–1060.

Patz, J. A., Campbell-Lendrum, D., Holloway, T., Foley, J. A., 2005. Impact of regional climate change on human health. Nature 438 (7066), 310–317.

Pinheiro, A. C. T., Privette, J. L., Guillevic, P., 2006. Modeling the observed angular anisotropy of land surface temperature in a savanna. Ieee Transactions on Geoscience and Remote Sensing 44 (4), 1036–1047.

Pinty, B., Gobron, N., Melin, F., Verstraete, M. M., 2002. A time composite algorithm for fapar products: Theoretical basis document. Tech. rep., Institute for Environment and Sustainability, Joint Research Centre.

Platnick, S., King, M. D., Ackerman, S. A., Menzel, W. P., Baum, B. A., Riedi, J. C., Frey, R. A., 2003. The modis cloud products: Algorithms and examples from terra. Ieee Transactions on Geoscience and Remote Sensing 41 (2), 459–473.

Prata, A. J., 1994. Land-surface temperatures derived from the advanced very high-resolution radiometer and the along-track scanning radiometer .2. experimental results and validation of avhrr algorithms. Journal of Geophysical Research-Atmospheres 99 (D6), 13025–13058.

Prihodko, L., Goward, S. N., 1997. Estimation of air temperature from remotely sensed surface observations. Remote Sensing of Environment 60 (3), 335–346.

Quattrochi, D. A., Luvall, J. C., Rickman, D. L., Estes, M. G., Laymon, C. A., Howell, B. F., 2000. A decision support information system for urban landscape management using thermal infrared data. Photogrammetric Engineering and Remote Sensing 66 (10), 1195–1207.

Rabin, R. M., Martin, D. W., 1996. Satellite observations of shallow cumulus coverage over the central united states: An exploration of land use impact on cloud cover. Journal of Geophysical Research-Atmospheres 101 (D3), 7149–7155.

Rasmussen, M. O., Pinheiro, A. C., Proud, S. R., Sandholt, I., 2010. Modeling angular dependences in land surface temperatures from the seviri instrument onboard the geostationary me-

teosat second generation satellites. Ieee Transactions on Geoscience and Remote Sensing 48 (8), 3123–3133.

Reale, A. L., 2002. Noaa operational sounding products for advanced-tovs. In: NOAA Tech. Rep. NESDIS. Vol. 107. Washington D.C., p. 29.

Romanov, P., 1999. Urban influence on cloud cover estimated from satellite data. Atmospheric Environment 33 (24-25), 4163–4172.

Roth, M., 2000. Review of atmospheric turbulence over cities. Quarterly Journal of the Royal Meteorological Society 126 (564), 941–990.

Roth, M., Oke, T. R., Emery, W. J., 1989. Satellite-derived urban heat islands from 3 coastal cities and the utilization of such data in urban climatology. International Journal of Remote Sensing 10 (11), 1699–1720.

Roy, D. P., 1997. Investigation of the maximum normalized difference vegetation index (ndvi) and the maximum surface temperature (t-s) avhrr compositing procedures for the extraction of ndvi and t-s over forest. International Journal of Remote Sensing 18 (11), 2383–2401.

Schneider, A., Friedl, M. A., Potere, D., 2009. A new map of global urban extent from modis satellite data. Environmental Research Letters 4 (4).

Schwarz, N., Lautenbach, S., Seppelt, R., 2011. Exploring indicators for quantifying surface urban heat islands of european cities with modis land surface temperatures. Remote Sensing of Environment 115 (12), 3175–3186.

Seemann, S., Borbas, E. E., Li, J., Menzel, W. P., Gumley, L. E., 2006. Modis atmospheric profile retrieval algorithm theoretical basis document. Tech. rep.

Seemann, S. W., Li, J., Menzel, W. P., Gumley, L. E., 2003. Operational retrieval of atmospheric temperature, moisture, and ozone from modis infrared radiances. Journal of Applied Meteorology 42 (8), 1072–1091.

Sen Roy, S., Yuan, F., 2009. Trends in extreme temperatures in relation to urbanization in the twin cities metropolitan area, minnesota. Journal of Applied Meteorology and Climatology 48 (3), 669–679.

Shao, Q. Q., Sun, C. Y., Liu, J. Y., He, J. F., Kuang, W. H., Tao, F. L., 2011. Impact of urban expansion on meteorological observation data and overestimation to regional air temperature in china. Journal of Geographical Sciences 21 (6), 994–1006.

Skamarock, W. C., Klemp, J. B., 2008. A time-split nonhydrostatic atmospheric model for weather research and forecasting applications. Journal of Computational Physics 227 (7), 3465–3485.

Smith, J. A., Ballard, J. R., Pedelty, J. A., 1997. Effect of three-dimensional canopy architecture on thermal infrared exitance. Optical Engineering 36 (11), 3093–3100.

Sohrabinia, M., Rack, W., Zawar-Reza, P., 2012. Analysis of modis lst compared with wrf model and in situ data over the waimakariri river basin, canterbury, new zealand. Remote Sensing 4 (11), 3501–3527.

Soux, A., Voogt, J. A., Oke, T. R., 2004. A model to calculate what a remote sensor 'sees' of an urban surface. Boundary-Layer Meteorology 112 (2), 401–424.

Stewart, I. D., 2011. A systematic review and scientific critique of methodology in modern urban heat island literature. International Journal of Climatology 31 (2), 200–217.

Stewart, I. D., Oke, T. R., 2012. Local climate zones for urban temperature studies. Bulletin of the American Meteorological Society 93 (12), 1879–1900.

Streutker, D. R., 2003. Satellite-measured growth of the urban heat island of houston, texas. Remote Sensing of Environment 85 (3), 282–289.

Sun, J. L., Mahrt, L., 1995. Determination of surface fluxes from the surface radiative temperature. Journal of the Atmospheric Sciences 52 (8), 1096–1106.

Taha, H., 1997. Urban climates and heat islands: Albedo, evapotranspiration, and anthropogenic heat. Energy and Buildings 25 (2), 99–103.

Tan, B., Woodcock, C. E., Hu, J., Zhang, P., Ozdogan, M., Huang, D., Yang, W., Knyazikhin, Y., Myneni, R. B., 2006. The impact of gridding artifacts on the local spatial properties of modis data: Implications for validation, compositing, and band-to-band registration across resolutions. Remote Sensing of Environment 105 (2), 98–114.

Tiangco, M., Lagmay, A. M. F., Argete, J., 2008. Aster-based study of the night-time urban heat island effect in metro manila. International Journal of Remote Sensing 29 (10), 2799–2818.

Tomlinson, C. J., Chapman, L., Thornes, J. E., Baker, C. J., 2012. Derivation of birmingham's summer surface urban heat island from modis satellite images. International Journal of Climatology 32 (2), 214–224.

United State Census Bureau, ., 2010. State & county quickfacts, houston (city), texas.

Vancutsem, C., Ceccato, P., Dinku, T., Connor, S. J., 2010. Evaluation of modis land surface temperature data to estimate air temperature in different ecosystems over africa. Remote Sensing of Environment 114 (2), 449–465.

Vinnikov, K. Y., Yu, Y., Goldberg, M. D., Tarpley, D., Romanov, P., Laszlo, I., Chen, M., 2012. Angular anisotropy of satellite observations of land surface temperature. Geophysical Research Letters 39 (23), L23802.

Voogt, J. A., 2008. Assessment of an urban sensor view model for thermal anisotropy. Remote Sensing of Environment 112 (2), 482–495.

Voogt, J. A., Oke, T. R., 1997. Complete urban surface temperatures. Journal of Applied Meteorology 36 (9), 1117–1132.

Voogt, J. A., Oke, T. R., 1998. Effects of urban surface geometry on remotely-sensed surface temperature. International Journal of Remote Sensing 19 (5), 895–920.

Voogt, J. A., Oke, T. R., 2003. Thermal remote sensing of urban climates. Remote Sensing of Environment 86 (3), 370–384.

Wan, Z., 2007. Collection-5 modis land surface temperature products users' guide. ICESS, University of California, Santa Barbara.

Wan, Z., 2014. New refinements and validation of the collection-6 modis land-surface temperature/emissivity product. Remote Sensing of Environment 140 (0), 36–45.

Wan, Z. M., 2008. New refinements and validation of the modis land-surface temperature/emissivity products. Remote Sensing of Environment 112 (1), 59–74.

Wan, Z. M., Dozier, J., 1996. A generalized split-window algorithm for retrieving land-surface temperature from space. Ieee Transactions on Geoscience and Remote Sensing 34 (4), 892–905.

Wang, W. H., Liang, S. L., 2009. Estimation of high-spatial resolution clear-sky longwave downward and net radiation over land surfaces from modis data. Remote Sensing of Environment 113 (4), 745–754.

Weng, Q. H., Lu, D. S., Schubring, J., 2004. Estimation of land surface temperature-vegetation abundance relationship for urban heat island studies. Remote Sensing of Environment 89 (4), 467–483.

Weng, Q. H., Rajasekar, U., Hu, X. F., 2011. Modeling urban heat islands and their relationship with impervious surface and vegetation abundance by using aster images. Ieee Transactions on Geoscience and Remote Sensing 49 (10), 4080–4089.

Williamson, S. N., Hik, D. S., Gamon, J. A., Kavanaugh, J. L., Koh, S., 2013. Evaluating cloud contamination in clear-sky modis terra daytime land surface temperatures using ground-based meteorology station observations. Journal of Climate 26 (5), 1551–1560.

World Health Organization Centre for Health Development, ., 2010. Hidden cities: unmasking and overcoming health inequities in urban settings. World Health Organization.

Xia, Y. L., Mitchell, K., Ek, M., Sheffield, J., Cosgrove, B., Wood, E., Luo, L. F., Alonge, C., Wei, H. L., Meng, J., Livneh, B., Lettenmaier, D., Koren, V., Duan, Q. Y., Mo, K., Fan, Y., Mocko, D., 2012. Continental-scale water and energy flux analysis and validation for the north american land data assimilation system project phase 2 (nldas-2): 1. intercomparison and application of model products. Journal of Geophysical Research-Atmospheres 117.

Zhan, W. F., Chen, Y. H., Voogt, J. A., Zhou, J., Wang, J. F., Ma, W., Liu, W. Y., 2012. Assessment of thermal anisotropy on remote estimation of urban thermal inertia. Remote Sensing of Environment 123, 12–24.

Zhang, P., Imhoff, M. L., Wolfe, R. E., Bounoua, L., 2010. Characterizing urban heat islands of global settlements using modis and nighttime lights products. Canadian Journal of Remote Sensing 36 (3), 185–196.

Zhou, J., Chen, Y. H., Wang, J. F., Zhan, W. F., 2011. Maximum nighttime urban heat island (uhi) intensity simulation by integrating remotely sensed data and meteorological observations. Ieee Journal of Selected Topics in Applied Earth Observations and Remote Sensing 4 (1), 138–146.

Appendix A

Supplemental Document for Chapter 4

Table S1 shows a list of sites that are used for the comparisons with MODIS near-surface temperature. The details of site information can be found on the NOAA national climatic data center (NCDC) website (`http://www.ncdc.noaa.gov/data-access/land-based-station-data/station-metadata/surface-station-listings`).

Fig. S1 illustrates the 11-year mean relative humidity for four cities. The daytime relative humidity over the urban areas is significantly lower than rural areas. The urban/rural differences decease during nighttime, however, the value in urban area still show a slight lower than that in rural areas.

Fig. S2 illustrates the comparison of MODIS dew-point temperatures and the ground observations for the sites over the land surface. As mentioned Section 4.4.1, the ability of MODIS to estimated Phoenix at the low range of dew-point temperature is limited. Under very humid climate area, e.g. Houston, the comparison suggests a relative scattered distribution around the reference line. The accuracy level and patterns in Chicago and Toronto are relatively consistent.

The clear sky days during 2003-2013 summers are shown in Fig. S3. Urban areas are tend to be more cloudy. Houston is in most cloudy area among four cities, especially during the daytime.

Table S1: A list of the site ID for each city. USAF is the identification fixed-weather-station USAF master station catalog identifier, which is assigned by a 6-digit number. NCDC is the identification fixed-weather-station NCDC WBAN identifier, which is identified by using a 5-digit number.

City	Total Sites	Site ID (USAF-NCDC) (Sites in land surface without water surface in the 5 km pixel)	Site ID (USAF-NCDC) (Sites with water surface in 5 km pixel)
Phoenix	14	722749-53128,722749-99999,722780-23183,722783-99999,722784-99999, 722785-23111,722785-99999,722786-23104,722786-99999,722787-53126, 722787-99999,722788-99999,722789-99999,999999-53156	NA
Houston	30	720594-99999,720617-99999,720637-99999,722427-99999,722429-53910, 722429-99999,722430-12960,722435-12918,722436-12906,722436-99999, 722444-99999,722527-99999,722543-99999,725021-99999,998481-99999, 722444-53902,722427-12975,722527-12976,722543-12977	720917-99999,722420-12923,722420-99999,994730-99999,997361-99999, 997363-99999,997364-99999,997370-99999,997729-99999,998181-99999, 998182-99999
Chicago	31	720137-99999,722059-99999,722075-99999,722126-99999,722127-99999, 725305-99999,725337-99999,725340-14819,725345-14834,725345-99999, 725347-99999,725348-99999,726505-99999,744655-99999,744665-99999, 999999-54811,725300-94846,725305-94892,726400-14839,725347-14880	725374-99999,726424-99999,992140-99999,997255-99999,997338-99999, 997340-99999,997735-99999,997787-99999,998497-99999,998498-99999, 725346-94866
Toronto	21	712625-99999,712630-99999,712643-99999,713680-99999,715080-99999, 716240-99999,716970-99999,718330-99999,719666-99999,716390-99999	711710-99999,712650-99999,712970-99999,714320-99999,714370-99999, 725287-99999,996550-99999 997989-99999,998168-99999,998235-99999, 998338-99999

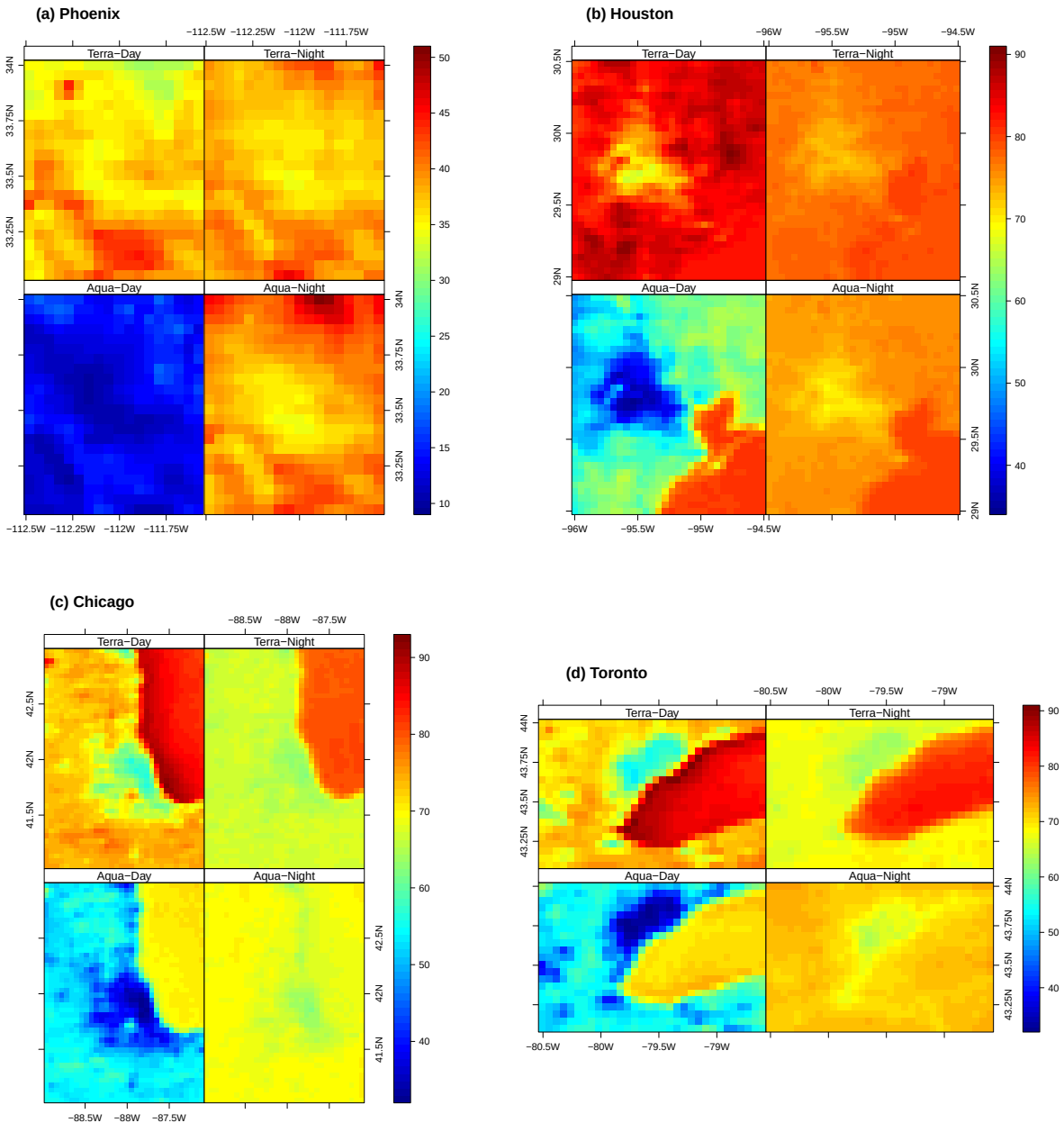

Figure S1: The 11-year JJA mean near-surface relative humidity (%) of four cities

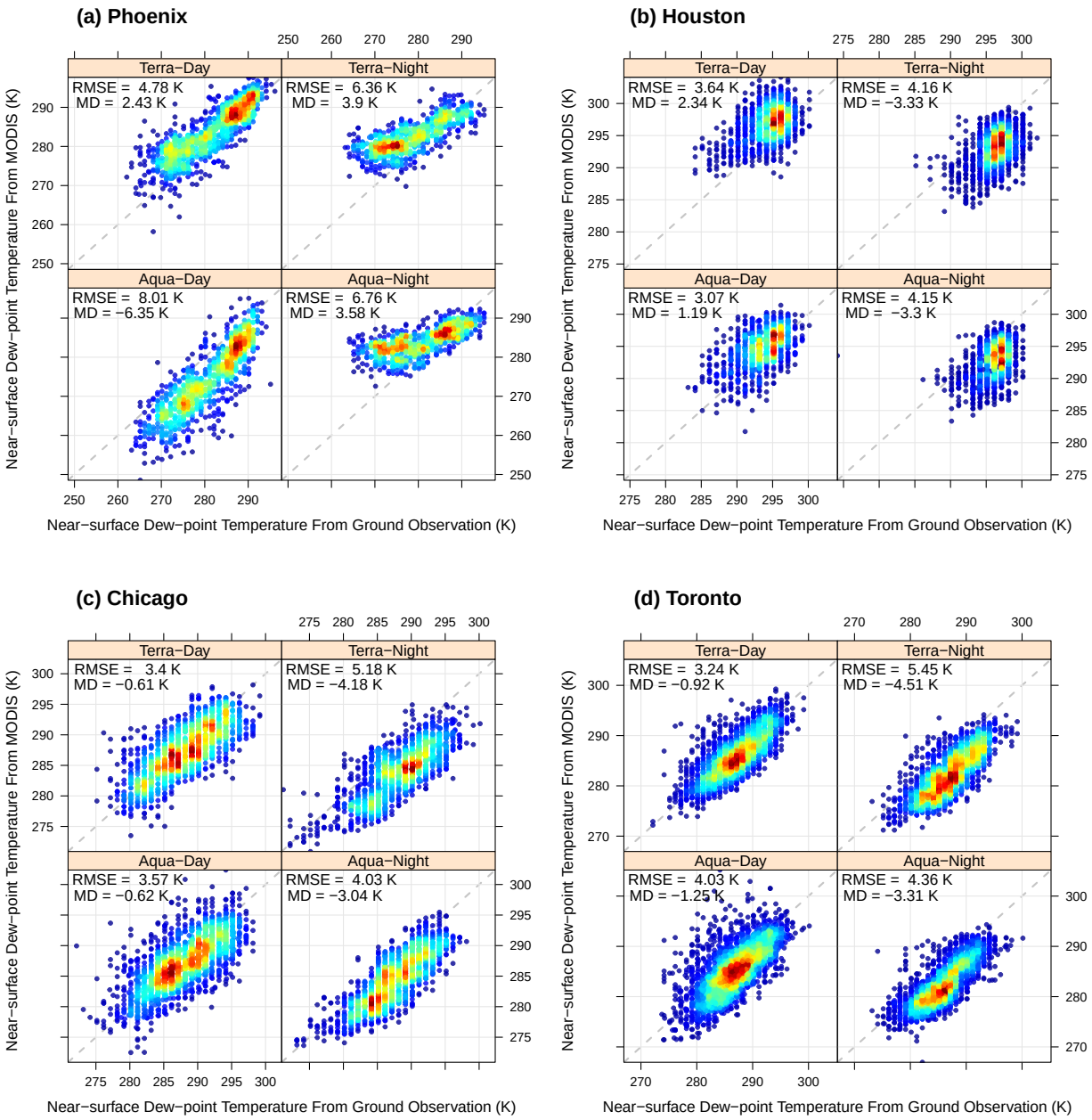

Figure S2: The density scatter plot of near-surface dew temperature from the ground observation (the sites denoted as empty circles shown in Fig. 4.3) and the MODIS product. Higher density shows in red and lower density is in Blue. RMSE is the Root-Mean-Square Error, and MD is the Mean of the Differences between MODIS estimations and ground observations in K.

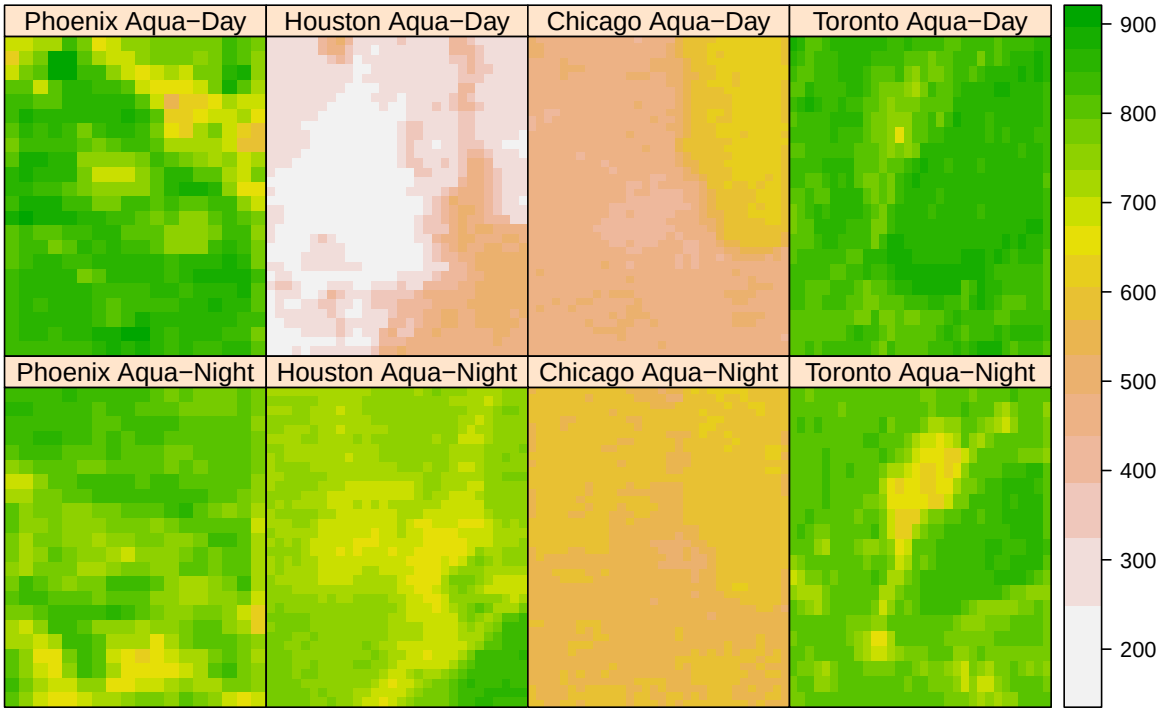

Figure S3: The number of pixels available during 2003-2013 JJA (total 1012 days) for four cities at Aqua overpasses.